

The ATLAS^{3D} project – XVIII. CARMA CO imaging survey of early-type galaxies

Katherine Alatalo,^{1,2*} Timothy A. Davis,³ Martin Bureau,⁴ Lisa M. Young,⁵
 Leo Blitz,¹ Alison F. Crocker,^{6,7} Estelle Bayet,⁴ Maxime Bois,⁸ Frédéric Bournaud,⁹
 Michele Cappellari,⁴ Roger L. Davies,⁴ P. T. de Zeeuw,^{3,10} Pierre-Alain Duc,⁹
 Eric Emsellem,^{3,11} Sadegh Khochfar,¹² Davor Krajnović,³ Harald Kuntschner,³
 Pierre-Yves Lablanche,^{3,11} Raffaella Morganti,^{13,14} Richard M. McDermid,¹⁵
 Thorsten Naab,¹² Tom Oosterloo,^{13,14} Marc Sarzi,¹⁶ Nicholas Scott,¹⁷
 Paolo Serra,¹³ and Anne-Marie Weijmans^{18†}

¹Department of Astronomy, Hearst Field Annex, University of California, Berkeley, CA 94720-3411, USA

²NASA Herschel Science Center, California Institute of Technology, 770 S. Wilson Ave., Pasadena, CA 91125, USA

³European Southern Observatory, Karl-Schwarzschild-Str. 2, 85748 Garching, Germany

⁴Sub-department of Astrophysics, Department of Physics, University of Oxford, Denys Wilkinson Building, Keble Road, Oxford OX1 3RH, UK

⁵Physics Department, New Mexico Institute of Mining and Technology, Socorro, NM 87801, USA

⁶Department of Astronomy, Lederle Graduate Research Tower B 619E, University of Massachusetts, Amherst, MA 01003, USA

⁷Physics Department, University of Toledo, 2801 W. Bancroft, Toledo, OH, USA

⁸Observatoire de Paris, LERMA and CNRS, 61 Av. de l'Observatoire, F-75014 Paris, France

⁹Laboratoire AIM Paris-Saclay, CEA/IRFU/SAp – CNRS – Université Paris Diderot, 91191 Gif-sur-Yvette Cedex, France

¹⁰Sterrewacht Leiden, Leiden University, Postbus 9513, 2300 RA Leiden, The Netherlands

¹¹Université Lyon 1, Observatoire de Lyon, Centre de Recherche Astrophysique de Lyon and Ecole Normale Supérieure de Lyon,
 9 avenue Charles André, F-69230 Saint-Genis Laval, France

¹²Max Planck Institut für Extraterrestrische Physik, PO Box 1312, D-85478 Garching, Germany

¹³Netherlands Institute for Radio Astronomy (ASTRON), Postbus 2, 7990 AA Dwingeloo, The Netherlands

¹⁴Kapteyn Astronomical Institute, University of Groningen, Postbus 800, 9700 AV Groningen, The Netherlands

¹⁵Gemini Observatory, Northern Operations Centre, 670 N. A'ohoku Place, Hilo, HI 96720, USA

¹⁶Centre for Astrophysics Research, University of Hertfordshire, Hatfield, Herts AL1 9AB, UK

¹⁷Centre for Astrophysics and Supercomputing, Swinburne University of Technology, Hawthorn, Victoria 3122, Australia

¹⁸Dunlap Institute for Astronomy & Astrophysics, University of Toronto, 50 St. George Street, Toronto, ON M5S 3H4, Canada

ABSTRACT

We present the Combined Array for Research in Millimeter Astronomy (CARMA) ATLAS^{3D} molecular gas imaging survey, a systematic study of the distribution and kinematics of molecular gas in CO-rich early-type galaxies. Our full sample of 40 galaxies (30 newly mapped and 10 taken from the literature) is complete to a $^{12}\text{CO}(1-0)$ integrated flux of $18.5 \text{ Jy km s}^{-1}$, and it represents the largest, best-studied sample of its type to date. A comparison of the CO distribution of each galaxy to the $g-r$ color image (representing dust) shows that the molecular gas and dust distributions are in good agreement and trace the same underlying interstellar medium. The galaxies exhibit a variety of CO morphologies, including discs (50%), rings (15%), bars+rings (10%), spiral arms (5%), and mildly (12.5%) and strongly (7.5%) disrupted morphologies. There appear to be weak trends between galaxy mass and CO morphology, whereby the most massive galaxies in the sample tend to have molecular gas in a disc morphology. We derive a lower limit to the total accreted molecular gas mass across the sample of $2.48 \times 10^{10} M_{\odot}$, or approximately $8.3 \times 10^8 M_{\odot}$ per minor merger within the sample, consistent with minor merger stellar mass ratios.

Key words: galaxies : elliptical and lenticular, cD – galaxies : kinematics and dynamics – galaxies : evolution – galaxies : ISM – radio lines : galaxies – galaxies : star formation – ISM : molecules – surveys

1 INTRODUCTION

The bimodality in the morphological classification of galaxies has long been known (Hubble 1926). Late-type galaxies (LTGs) typically have exponential discs, spiral structure and blue colours. Early-type galaxies (ETGs) are more ellipsoidal, with smoother isophotes and red colours. One scenario for producing this galaxy bimodality is via mergers. Simulations have shown that a merger between two LTGs often creates an ETG (Toomre & Toomre 1972; Springel et al. 2005). ETGs are also much more likely to be found on the “red sequence” portion of the color-magnitude diagram (CMD; Baldry et al. 2004; Faber et al. 2007), presumably due to the loss of most of their star-forming material.

ETGs have been shown to be deficient in star formation relative to LTGs at a given mass (Visvanathan & Sandage 1977; Bower et al. 1992), and therefore should be molecular and atomic gas-poor (Lees et al. 1991). Recently, it has however become clear that they are not devoid of cold gas, containing reservoirs of dust (e.g. Hawarden et al. 1981; Jura 1986; Knapp et al. 1989), neutral atomic gas (e.g. Knapp et al. 1985; Sage & Welch 2006; Oosterloo et al. 2010) and molecular gas (e.g. Sage & Wrobel 1989; Welch & Sage 2003; Combes et al. 2007).

The ATLAS^{3D} sample is a complete, volume-limited sample of 260 local ETGs brighter than $M_K = -21.5$, covering distances to 42 Mpc with some restrictions on declination and Galactic latitude (Cappellari et al. 2011a, hereafter Paper I). The survey was designed to help us understand ETG formation and evolution. Optical integral-field spectroscopy with SAURON on the William Herschel Telescope (WHT) has been obtained over the central $41'' \times 33''$ region of all ATLAS^{3D} galaxies, revealing their internal stellar kinematics, stellar population properties and ionized gas distributions and kinematics. The ATLAS^{3D} sample has also been completely observed in CO J=1–0 and J=2–1 with the Institut de Radioastronomie Millimétrique (IRAM) 30m telescope (Young et al. 2011,

hereafter Paper IV), and 65% of the sample has been observed in H I with the Westerbork Synthesis Radio Telescope (WSRT; Morganti et al. 2006; Oosterloo et al. 2010; Serra et al. 2012, hereafter Paper XIII). For studies of the cold and warm interstellar medium (ISM), the ATLAS^{3D} sample is thus one of the largest and best-observed samples of local ETGs available.

Of the 260 ETGs in the ATLAS^{3D} sample, 56 were detected in CO (22% detection rate; Paper IV). However, despite emerging evidence that a non-negligible fraction of ETGs contain molecular gas, little is known about its origin and evolution, although various scenarios have been put forth (see e.g. Davis et al. 2011b, hereafter Paper X¹). The three most prominent scenarios are outlined here. First, it is possible that the gas survived the galaxy’s transformation into an ETG and was not completely consumed subsequently through secular evolution. Second, the molecular gas may have accumulated internally through stellar mass loss (Faber & Gallagher 1976). In the ATLAS^{3D} sample, it is expected that each galaxy produces on average $0.1 M_{\odot} \text{ yr}^{-1}$ of ISM through mass loss from the old stellar population alone (Ciotti et al. 1991). Third, it is possible that the molecular gas was accreted from an external source, through tidal stripping events, cold accretion and/or minor mergers with gas-rich companions. The minor merger (1:4 – 1:10 mass ratios) rate calculated by Lotz et al. (2008, 2011) suggests that there are approximately 0.12 minor mergers per galaxy per Gyr, so the ETGs of the ATLAS^{3D} sample as a whole should have undergone a total of ≈ 30 minor mergers in the last Gyr. It is also possible that this molecular gas is leftover from major mergers that have taken place, but minor mergers dominate in number. Determining the origin of the molecular gas therefore requires a detailed analysis of its distribution and kinematics (e.g. angular momentum), only available from interferometric maps, and a comparison to the stellar kinematics (as done in Paper X).

How the properties of the molecular gas depend on the environment of the host galaxy is an open question. For instance, galaxies in clusters may well be unable to acquire cold external gas, specifically atomic hydrogen (H I), due to the presence of the hot

* email: kalatalo@ipac.caltech.edu

† Dunlap Fellow

‡ $18.5 \text{ Jy km s}^{-1}$ is drawn from the IRAM 30m survey, and as the interferometric data indicate that the 30m molecular gas masses are generally underestimates, the true limit is likely slightly higher.

¹ The current paper presents in detail the observations used in Paper X to discuss the origin of the CO.

intracluster medium (ICM) and associated ram pressure stripping (Cayatte et al. 1990; Böhringer et al. 1994; Paper X). A first effort towards studying the molecular gas properties of ETGs with multiple molecular transitions (including ¹³CO, HCN and HCO⁺ in addition to ¹²CO; Crocker et al. 2012, hereafter Paper XI) shows that the molecular gas properties widely vary among ETGs, probably due to ¹²CO optical thickness variations linked to the dynamical state of the gas.

It is also not well determined whether the properties of individual galaxies are the determining factors in the behavior of the molecular gas, or whether the molecular gas in ETGs follows the same star-formation relations as in spirals (e.g. Kennicutt 1998; Bigiel et al. 2008; Shapiro et al. 2010; Wei et al. 2010a; Crocker et al. 2011). To completely understand star formation in ETGs, it is vital to study in a spatially-resolved way the molecular gas in an unbiased sample of molecular-gas rich ETGs. Therefore, as part of the ATLAS^{3D} project, we performed the present imaging survey with the Combined Array for Research in Millimeter Astronomy (CARMA), the first of its kind capable of providing significant conclusions about the state of molecular gas in ordinary ETGs from interferometric imaging.

In §2, we describe the selection criteria used to define the CARMA sample. In §3, we describe the observational strategy, the data calibration and reduction, and the analysis techniques. In §4, we investigate the properties of the molecular gas in the sample, including the range of morphologies present and their relationships to other host galaxy properties. We conclude briefly in §5. Appendix A describes the CO data of individual galaxies in the CARMA ATLAS^{3D} sample. Appendix B presents CO literature data of CO-imaged ATLAS^{3D} galaxies, that will be included in the official data release in a uniform manner.

2 THE CARMA SAMPLE

The sample of ETGs chosen for the CARMA survey was extracted from the ATLAS^{3D} survey. All ATLAS^{3D} galaxies were observed with the IRAM 30m telescope in CO(1–0) and CO(2–1), mostly by Combes et al. (2007) and Paper IV, though a few were observed by Welch & Sage (2003). The CARMA sample consists of 30 of the CO-detected ATLAS^{3D} galaxies (see Table 1). NGC 2697 and NGC 4292, removed from the ATLAS^{3D} sample because of evidence of spiral structure in optical images and of a lack of SAURON data, respectively, were also imaged with CARMA. We present their maps in Appendix C, but will not use them in any statistical work discussed in §4. We will refer to the 30 CO-rich ATLAS^{3D} galaxies with CARMA data as the CARMA ATLAS^{3D} sample.

Including 10 CO-detected sample galaxies that have already been interferometrically-mapped (see §3.5). The total number of ATLAS^{3D} galaxies with interferometric observations discussed in this paper is 40. This sample of CO-imaged ATLAS^{3D} galaxies is complete for the 33 brightest objects, down to an integrated CO(1–0) flux limit of 18.5 Jy km s^{−1} (corresponding to the flux of NGC 3182). Two galaxies with fluxes below this threshold also have CARMA CO images, UGC 05408 and NGC 5173. Five other CO-faint galaxies have CO maps in the literature (NGC 4550 by Crocker et al. 2009; NGC 2768, NGC 4477 and NGC 3489 by Crocker et al. 2011; NGC 2685 by Schinnerer & Scoville 2002). The faintest detections from Paper IV were not observed due to observing time restrictions.

Objects in the CARMA ATLAS^{3D} sample have total absolute *K*-band magnitudes ranging from $M_K = -21.57$ to -25.09 , and

distances from 13.4 Mpc to 45.8 Mpc². Six of the 30 galaxies belong to the Virgo cluster. All galaxies but three (IC 719, NGC 1222 and NGC 7465) are regular rotators according to their stellar kinematics (Krajnović et al. 2011, hereafter Paper II). NGC 1222, classified as a non-regular rotator, is known to be undergoing a strong interaction with a neighbour. NGC 7465 is undergoing an interaction with NGC 7464 and NGC 7463, and has a kinematically-decoupled core. IC 719 does show ordered rotation in its stellar component, but is recognized as a 2 σ (double-peaked) galaxy when the velocity dispersion map is considered, indicating two counter-rotating stellar discs. Further properties of the sample galaxies are listed in Table 1.

3 OBSERVATIONS, CALIBRATION AND DATA REDUCTION

3.1 CARMA observations

Observations for this survey were taken in the ¹²CO(1–0) line at CARMA over the course of five semesters, beginning in Autumn 2008 and finishing in November 2010. Galaxies were always first observed with the CARMA D array, with 11 – 150m baselines, corresponding to observable angular scales of 3.5 – 48'' at CO(1–0). NGC 2697 and NGC 7465, that appeared to have significant flux resolved out, were followed up with the more compact E array (8 – 66m baselines). NGC 1266 was spatially unresolved in D array, and was followed up with the CARMA B and A arrays (a detailed discussion of NGC 1266 can be found in Alatalo et al. 2011). The CARMA ATLAS^{3D} survey had a surface brightness sensitivity (1σ in 100 km s^{−1} linewidth) ranging from 12 to 369 M_\odot pc^{−2}, with median a sensitivity of 84 M_\odot pc^{−2}. On average, ≈ 100 hours of observations were obtained each semester. Observational parameters are listed in Table 2.

Upgrades to the CARMA correlator and receivers were taking place while the ATLAS^{3D} survey was ongoing, so data taken later in the programme have larger bandwidths and simultaneous observations of ¹²CO(1–0) and ¹³CO(1–0). A handful of ATLAS^{3D} galaxies thus also have ¹³CO maps that will be presented in an upcoming paper. The galaxies with large line widths ($\Delta v \gtrsim 420$ km s^{−1}) were observed only after the CARMA correlator was upgraded, providing sufficient bandwidth and channel resolution to properly cover and sample the line. We were able to reliably image 3mm continuum in three sources (NGC 1266, NGC 3665 and NGC 5866), and Table 3 lists those fluxes as well as upper limits for the other galaxies.

3.2 Calibration and imaging

Raw CARMA visibility data were reduced in the usual way, using the Multichannel Image Reconstruction Image Analysis and Display (MIRIAD) package (Sault et al. 1995). For each source and track, the raw data were first Hanning-smoothed in velocity. Then the phase vs. time behaviour of the calibrator was checked to search for decorrelations over baselines, which were flagged out. Next, the data were corrected for differences in the lengths of the fiber optic lines between the antennas and the correlator. The bandpass

² UGC 05408 was kept in the ATLAS^{3D} survey because its estimated distance is within 42 Mpc when errors in the distance estimate are taken into account (Paper I)

Table 1. CARMA ATLAS^{3D} galaxy sample.

Name	α (J2000)	δ (J2000)	v_{sys} (km s ⁻¹)	i (deg)	ϕ_{mol} (deg)	d (Mpc)	Virgo membership
IC 676	11 12 39.84	+09 03 20.7	1429	69	16.5	24.6	0
IC 719	11 40 18.52	+09 00 35.6	1833	74	229.0	29.4	0
IC 1024	14 31 27.07	+03 00 30.0	1479	72	24.5	24.2	0
NGC 1222	03 08 56.76	-02 57 19.3	2422	41	33.0 ^c	33.3	0
NGC 1266	03 16 00.79	-02 25 38.6	2170	26	270	29.9	0
NGC 2764	09 08 17.44	+21 26 35.8	2706	65	202.5	39.6	0
NGC 2824	09 19 02.22	+26 16 12.3	2758	61	161.5	40.7	0
NGC 3182	10 19 33.02	+58 12 21.0	2118	35	331.5	34.0	0
NGC 3607	11 16 54.54	+18 03 07.1	942	34	302.5	22.2	0
NGC 3619	11 19 21.60	+57 45 28.3	1560	48	74.5	26.8	0
NGC 3626	11 20 03.78	+18 21 25.6	1486	67	169.5	19.5	0
NGC 3665	11 24 43.64	+38 45 46.2	2069	64	219.5	33.1	0
NGC 4119	12 08 09.60	+10 22 44.7	1656	69	296.0	16.5	1
NGC 4150	12 10 33.65	+30 24 05.5	208	54	146.0	13.4	0
NGC 4324	12 23 06.17	+05 15 02.8	1665	62	232.0	16.5	1
NGC 4429	12 27 26.56	+11 06 27.3	1104	68	82.0	16.5	1
NGC 4435	12 27 40.49	+13 04 44.3	791	52	201.0	16.7	1
NGC 4694	12 48 15.10	+10 59 01.3	1171	69	155.5	16.5	1
NGC 4710	12 49 39.36	+15 10 11.7	1102	86	207.0	16.5	1
NGC 4753	12 52 22.07	-01 11 57.9	1163	75	93.0	22.9	0
NGC 5173	13 28 25.29	+46 35 29.9	2424	24	100 ^c	38.4	0
NGC 5379	13 55 34.35	+59 44 34.3	1774	64	66	30.0	0
NGC 5866	15 06 29.60	+55 45 48.0	755	89	127	14.9	0
NGC 6014	15 55 57.39	+05 55 54.7	2381	22	139.5	35.8	0
NGC 7465	23 02 00.96	+15 57 53.3	1960	70	106.0	29.3	0
PGC 029321	10 05 51.18	+12 57 40.7	2816	38	76	40.9	0
PGC 058114	16 26 04.29	+02 54 23.6	1507	71	94.5	23.8	0
UGC 05408	10 03 51.86	+59 26 10.2	2998	31	315 ^c	45.8	0
UGC 06176	11 07 24.68	+21 39 25.6	2677	68	201.0	40.1	0
UGC 09519	14 46 21.12	+34 22 14.2	1631	41	177.5	27.6	0
NGC 2697 ^a	08 54 59.40	-02 59 15.2	1814 ^b	30	301.5	22.0	0
NGC 4292 ^a	12 21 16.49	+04 35 44.3	2258 ^b	50	230	29.8	0

^a Removed from the ATLAS^{3D} sample, but the CO data are presented in Appendix C.^b From the HYPERLEDA catalog, due to the absence of SAURON data.^c Not originally in Paper V.**Notes:**

Column (1): Principle designation from LEDA, used as the standard designation.

Column (2): Right ascension (J2000), from LEDA.

Column (3): Declination (J2000), from LEDA.

Column (4): Optical stellar heliocentric velocity, from Paper I.

Column (5): Best-determined CO inclination angle, from Paper V.

Column (6): Kinematic position angle of the molecular gas, from Paper X.

Column (7): Average distance to each galaxy, from Paper I, originally from Tonry et al. (2001) and Mei et al. (2007).

Column (8): Virgo membership of each galaxy, from Paper I.

Table 2. Observational parameters of CARMA galaxies

Name	Semester	Gain calibrator	Total hours	$\theta_{\text{maj}} \times \theta_{\text{min}}$ (arcsec)	ΔV (km s ⁻¹)	Bandwidth (km s ⁻¹)
IC 676	2009B	1058+015	3.75	3.8×3.3	10	410
IC 719	2010A	3C273	13.17	3.9×2.8	20	580
IC 1024	2008B	3C279	4.68	3.9×3.0	10	420
NGC 1222	2008B	0339-017	5.20	3.6×3.2	5	420
NGC 1266	2008B	0339-017	5.43	4.2×3.3	10	410
NGC 2764	2009B	0854+201	4.43	3.5×2.9	10	410
NGC 2824	2008B	0956+252	8.79	4.3×4.0	25	400
NGC 3182	2009A	0927+390	7.42	5.2×4.1	30	390
NGC 3607	2010B	1058+015	9.30	5.6×5.0	20	900
NGC 3619	2010B	0958+655	24.44	4.4×3.9	40	880
NGC 3626	2009B	1159+292	7.50	3.9×3.7	25	400
NGC 3665	2010B	1159+292	16.59	4.3×4.2	10	910
NGC 4119	2008B	3C273	3.67	5.0×4.0	10	410
NGC 4150	2010A	1159+292	6.74	5.3×4.1	10	560
NGC 4324	2009A	3C273	20.18	4.7×3.9	20	400
NGC 4429	2010B	3C273	8.83	4.7×3.7	10	840
NGC 4435	2010B	3C273	8.48	3.9×3.4	10	920
NGC 4694	2010A	3C273	5.38	3.9×3.1	10	390
NGC 4710	2009A	3C273	5.10	3.9×3.2	10	410
NGC 4753	2010B	3C273	10.38	5.6×4.1	15	735
NGC 5173	2009B ^a	1310+323	7.06	3.9×3.5	20	240
NGC 5379	2010A	1642+689	5.33	5.2×3.6	10	410
NGC 5866	2010B	1419+543	3.52	3.6×3.1	10	920
NGC 6014	2008B	1751+096	3.85	4.2×3.9	10	350
NGC 7465	2008B 2009A ^b	3C454.3	15.02	6.6×5.6	10	410
PGC 029321	2009B	1058+015	4.52	3.8×3.7	10	410
PGC 058114	2009A	1549+026	3.62	4.4×3.8	10	410
UGC 05408	2009A	0927+390	2.00	4.6×3.5	25	196
UGC 06176	2009A	1159+292	4.08	3.5×2.8	15	735
UGC 09519	2008B	1310+323	3.75	3.4×2.9	10	410
NGC 2697	2008B 2009A ^b	0927+390	14.33	6.8×5.1	20	380
NGC 4292	2008B	3C273	19.86	4.1×3.3	10	410

^a Observed both in C- and D-arrays^b Observed in D-array in 2008B and E-array in 2009A.**Notes:**

Column (1): Principle designation from LEDA, used as the standard designation.

Column (2): Semester in which the observations were taken at CARMA.

Column (3): Gain calibrator used.

Column (4): Total on-source observing time in hours.

Column (5): FWHM of the major and minor axes of the synthesized beam.

Column (6): Final velocity channel width.

Column (7): Velocity bandwidth covering the line.

was then determined using a high signal-to-noise ratio (S/N) observation of a bright calibrator, and used to correct for instrumental spectral fluctuations. The atmospheric phase offsets present in the data were determined using a phase calibrator, usually a quasar within 20° of the source, observed at regular (≈ 15 minutes) intervals. Amplitude calibration was performed using the phase calibrator. A catalog of the most up-to-date fluxes of each calibrator is maintained at CARMA, both through monitoring of calibrator fluxes during science tracks and through dedicated flux calibration tracks taken on a weekly basis, and is updated weekly using all tracks that include a primary calibrator (e.g. a planet), used to infer the secondary calibrator fluxes (Bauermeister et al. 2012). Flux calibration uncertainties are assumed to be 20%, which is standard for millimeter observations using planetary models (Petric et al., in prep). After the data were satisfactorily processed, the gain solutions derived from the nearby calibrator were applied to the source. The calibrated source data of all observations of each source were then combined into one visibility file for imaging.

We then used MIRIAD to convert all visibility files to three-dimensional (3D) data cubes. When possible, a zeroth order continuum fit to the uv -data was made using channels free of line emission, and was subtracted from all channels. Only galaxies observed after the correlator was upgraded (bandwidth > 420 km s⁻¹) had sufficient bandwidth for a reliable continuum fit. Galaxies with narrower bandwidths were not continuum-subtracted (continuum emission generally adds $< 10\%$ extra flux to each galaxy, much less than the total flux calibration uncertainties, and this is usually confined to the central beam in each galaxy). The continuum-subtracted uv -datasets were then transformed into RA-Dec-velocity space (with velocities determined from the line being imaged, mainly ¹²CO but also occasionally ¹³CO). Channel widths were chosen to achieve at least a 3σ detection in each channel where flux was present, and were always larger (by at least a factor of 2) than the original spectral resolution of the uv -data. Pixels of $1'' \times 1''$ were chosen as a compromise between spatial sampling and resolution, typically giving approximately 4 pixels across the beam major axis. A constant pixel size was chosen to maintain uniform spatial sampling across the sample. One arcsecond corresponds to a physical scale between 72 and 222 pc, depending on the distance of the source. The areas imaged were generally chosen to be within the primary beam of the 10m antennas ($\approx 54''$), but in the cases of sources that extend beyond this (NGC 4324, NGC 4710 and NGC 5866), the area imaged was taken to be closer to the primary beam of the 6m antennas ($\approx 90''$). In these cases, the MIRIAD imaging task INVERT was run with the mosaicking option, to properly scale the data and account for the different primary beam widths.

Robust=0 weighting was used by default, but was changed if the size and make-up of the source dictated it. Natural weighting (robust = 1) was used for sources where large scale features presented in the initial (robust = 0) channel maps, and we suspected that some flux might be resolved out (NGC 3619, NGC 3626 and NGC 4324). The dirty cubes were cleaned in regions of source emission to a threshold equal to the rms of the dirty channels. The clean components were then added back and re-convolved using a Gaussian beam of full-width at half maximum (FWHM) equal to that of the dirty beam. This produced the final, reduced and fully calibrated data cube for each galaxy.

The 3D data cubes were then used to create moment maps of each galaxy: a zeroth moment (moment0) or integrated intensity map, and a first moment (moment1) or mean velocity map. The data cubes were first Hanning-smoothed in velocity and Gaussian-

smoothed spatially (with a FWHM equal to that of the beam), and masks were created by selecting all pixels above fixed flux thresholds, adjusted to recover as much flux as possible in the moment maps while minimising the noise (generally about 2–3 times the rms noise in the smoothed channels). The moment maps were then created using the unsmoothed cubes within the masked regions only.

All data products were converted into Flexible Image Transport System (FITS) files using MIRIAD. Tables 2 and 3 list some datacube properties for each of the ATLAS^{3D} CARMA galaxies. Figure 1 shows the CO moment0 contours of each CARMA ATLAS^{3D} sample galaxy overlaid on an r -band image, either from the Sloan Digital Sky Survey (SDSS) or the Isaac Newton Telescope (INT) when SDSS imaging is unavailable (Scott et al. 2012, submitted, hereafter Paper XXI). Figure 2 displays the moment1 maps of the 30 sample galaxies. Figure 3 shows the CO moment0 contours overlaid on unsharp-masked optical images, to enhance dust features (see §4.1). Figure 4 displays position-velocity diagrams (PVDs) of galaxies whose kinematics are not well represented with moment1 maps, due to multiple velocity components along the line-of-sight (NGC 2764, NGC 4710 and NGC 5866). Appendix A contains multiple figures for each CARMA ATLAS^{3D} galaxy, including a r -band-moment0 overlay, moment0 map, moment1 map, a comparison of the CARMA and IRAM 30m spectra, a PVD along the kinematic position angle determined in Paper X, and individual channel maps. A more detailed analysis of the PVD, as well as a comparison to the stellar and ionized gas kinematics is available in Davis et al. (2012, hereafter Paper XIV).

The continuum measurement or upper limit for each galaxy depended on the correlator configuration. For narrow-band (bandwidth ≈ 420 km s⁻¹) galaxies that did not include ¹³CO in the lower sideband, the full lower sideband was used to calculate the continuum (bandwidth ≈ 186 MHz). For narrow-band galaxies that included ¹³CO observations, the edges of the band in the lower sideband were used (bandwidth ≈ 124 MHz). Galaxies that were observed with the upgraded correlator were treated individually, the continuum being modeled in line-free channels only, which varied from galaxy to galaxy. The continuum upper limit was taken to be three times the rms noise of the dirty map produced by inverting the combined line-free channels. Galaxies where a continuum source was detected (NGC 1266, NGC 3665 and NGC 5866), the flux was measured from the detected point source, and the rms noise was measured in the flux-free regions of the cleaned maps.

3.3 Measurements from the data

To calculate the noise level, σ_{rms} of each data cube, we selected all the pixels within each cube outside the region known to contain flux, and calculated the standard deviation. The total flux per channel was then calculated by using the region of the moment0 map that contained flux, then summing over all pixels in each channel located within that region. The statistical noise per channel is calculated as $\sigma_{\text{rms}} * \sqrt{N_b}$, where N_b is the number of beam areas in the region with identified emission. The CARMA integrated spectra presented in Appendix A have been constructed using this method. The integrated fluxes in the channel maps were converted from the native Jansky beam⁻¹ units into Jansky by dividing out the total beam area in pixels, and are given in Table 3.

PVDs were created by taking thin (5 pixel) slices through the data cubes, positioned to intersect the centre of the CO emission, and using the kinematic position angle determined in Paper X. Table 1 also lists the kinematic position angles of galaxies not orig-

Table 3. Data parameters of CARMA ATLAS^{3D} galaxies

Name	σ_{rms} (mJy bm ⁻¹)	Continuum (mJy bm ⁻¹)	F_{CARMA} (Jy km s ⁻¹)	$\log \frac{M_{\text{H}_2}}{M_{\odot}}$	$\frac{F_{\text{CARMA}}}{F_{30\text{m}}}$	Morph. class.
IC 676	30.6	< 3.09	66.3 ± 2.5	8.71 ± 0.04	1.2 ± 0.05	D
IC 719	6.63	< 0.351	20.4 ± 1.0	8.34 ± 0.05	1.2 ± 0.12	D
IC 1024	19.4	< 3.06	94.6 ± 1.7	8.87 ± 0.02	1.8 ± 0.04	D
NGC 1222	23.1	< 1.97	147.6 ± 1.6	9.33 ± 0.01	1.8 ± 0.04	X
NGC 1266	22.8	7.49 ± 1.96	162.9 ± 0.7	9.28 ± 0.01	1.0 ± 0.03	D
NGC 2764	12.9	< 1.85	85.4 ± 1.5	9.23 ± 0.02	1.1 ± 0.04	B+R
NGC 2824	10.2	< 2.21	37.8 ± 0.8	8.91 ± 0.02	1.8 ± 0.08	D
NGC 3182	8.16	< 1.68	16.4 ± 0.7	8.41 ± 0.04	1.2 ± 0.12	R
NGC 3607	7.50	< 0.830	58.0 ± 0.8	8.50 ± 0.01	1.2 ± 0.04	D
NGC 3619	3.23	< 0.327	15.2 ± 0.4	8.28 ± 0.03	0.7 ± 0.12	M
NGC 3626	5.34	< 1.48	43.2 ± 0.9	8.32 ± 0.02	1.3 ± 0.10	D
NGC 3665	10.2	8.98 ± 0.42	94.3 ± 1.2	9.11 ± 0.01	1.6 ± 0.06	D
NGC 4119	20.2	< 2.64	39.3 ± 0.9	8.14 ± 0.02	1.8 ± 0.07	R
NGC 4150	9.41	< 1.87	20.5 ± 0.4	7.82 ± 0.02	0.7 ± 0.08	M
NGC 4324	4.30	< 0.974	27.2 ± 0.6	7.97 ± 0.02	1.9 ± 0.12	R
NGC 4429	9.53	< 0.375	70.8 ± 0.9	8.39 ± 0.01	2.2 ± 0.08	D
NGC 4435	11.5	< 0.375	31.6 ± 1.0	8.05 ± 0.03	1.5 ± 0.10	R
NGC 4694	9.30	< 0.512	21.7 ± 0.6	8.01 ± 0.03	0.7 ± 0.07	X
NGC 4710	14.0	< 5.20	351.2 ± 1.7	9.08 ± 0.01	2.3 ± 0.03	B+R
NGC 4753	11.1	< 0.521	74.7 ± 1.1	8.70 ± 0.01	1.4 ± 0.06	M
NGC 5173	8.16	< 1.46	12.5 ± 0.2	8.36 ± 0.02	1.2 ± 0.14	X
NGC 5379	10.8	< 0.450	18.5 ± 0.8	8.53 ± 0.04	1.6 ± 0.15	B+R
NGC 5866	17.6	4.02 ± 0.54	258.2 ± 3.4	8.75 ± 0.01	1.9 ± 0.02	B+R
NGC 6014	22.4	< 3.61	34.5 ± 1.0	8.77 ± 0.03	1.0 ± 0.07	S
NGC 7465	9.71	< 1.39	93.6 ± 0.4	9.02 ± 0.01	1.7 ± 0.04	M
PGC 029321	13.1	< 2.09	18.3 ± 0.7	8.61 ± 0.04	1.2 ± 0.09	D
PGC 058114	15.7	< 2.21	73.7 ± 0.9	8.75 ± 0.01	1.4 ± 0.04	D
UGC 05408	13.6	< 2.83	6.1 ± 0.5	8.32 ± 0.08	0.8 ± 0.18	D
UGC 06176	10.8	< 0.524	28.5 ± 0.8	8.76 ± 0.03	1.5 ± 0.10	D
UGC 09519	19.5	< 2.27	51.4 ± 1.4	8.77 ± 0.03	0.9 ± 0.04	M
NGC 2697	9.89	< 1.36	48.2 ± 0.7	8.61 ± 0.01	2.3 ± 0.11	R
NGC 4292	9.58	< 1.05	13.8 ± 0.5	7.74 ± 0.04	1.2 ± 0.14	R

Notes:

Column (1): Principle designation from LEDA, used as the standard designation.

Column (2): Root mean square noise level per channel, measured in regions devoid of line emission.

Column (3): Continuum emission or upper limit (see text).

Column (4): Total CO flux from CARMA.

Column (5): Total molecular gas mass from the CARMA observations using $X_{\text{CO}} = 3 \times 10^{20} \text{ (K km s}^{-1}\text{)}^{-1} \text{ cm}^{-2}$ (as in Paper IV)

Column (6): Fraction of CO flux recovered by CARMA (with respect to the IRAM 30m telescope).

Column (7): CO morphological classification, based on the moment0 and moment1 maps:

D = disc, X = strongly disrupted, R = ring, M = mildly disrupted, B = bar/ring, S = spiral.

inally listed in Paper X, but subsequently had kinematic position angles fitted using the same methods.

3.4 Comparison to the 30m data

The integrated spectra from CARMA and the IRAM 30m telescope are overlaid in Figs. A1–A30. Millimeter measurements are assumed to have 20% absolute flux uncertainties (errors reported on the measured parameters listed in Table 3 only include the random errors on the measurement itself, not the systematic flux calibration error), so flux ratios between 0.78 and 1.28 indicate fluxes in agreement within the uncertainties. The spectra from the IRAM 30m agree with the CARMA ones for 15/30 galaxies. In all cases where there is disagreement, CARMA actually recovers more flux than the 30m. Most discrepant galaxies either extend beyond, or fill the majority of the single-dish beam, with two large ratios (NGC 4435 and UGC 06176) likely due to a slight off-center pointing of the single dish. In fact, only 7 of the galaxies within the CARMA ATLAS^{3D} sample are well contained within the 21.6'' IRAM beam.

As discussed above, all galaxies detected with the IRAM 30m were also detected at CARMA. However, the IRAM 30m selection for the current CARMA survey does imply that galaxies with molecular gas exclusively beyond the 30m beam (e.g. rings, arms and tidal features beyond a radius of $\approx 12''$) would have been missed. It is impossible to estimate the incidence of these objects based on the CO data alone, but the Galaxy Evolution Explorer (GALEX) ultraviolet imaging survey of the SAURON sample (tracing the associated star formation) suggests that they are very rare (of 34 ETGs, only one has such features, NGC 2974; Jeong et al. 2009). Lower density neutral hydrogen is however fairly common at large radii (Paper XIII).

Because the molecular gas in many ($> 75\%$) galaxies extends beyond the single-dish beam, it is likely that the CARMA flux more accurately reflects the total molecular gas mass in each galaxy, and therefore we adopt the CARMA derived molecular gas masses for the remainder of this paper.

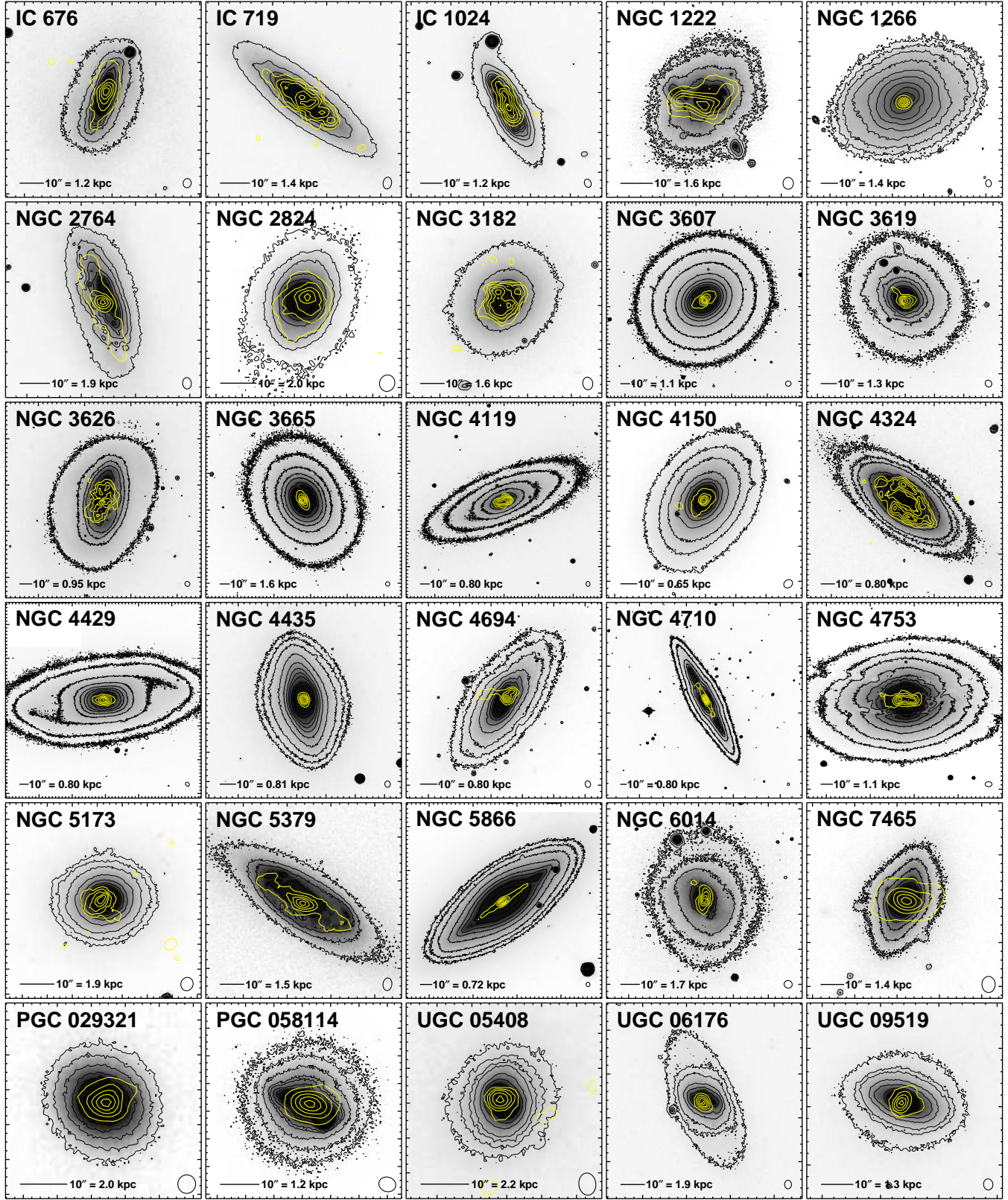


Figure 1. r -band images (grayscale and black contours) overlaid with integrated CO(1–0) contours (yellow) at [10%, 30%, 50%, 70%, 90%] of the peak intensity for the 30 galaxies in the ATLAS^{3D} CARMA sample. The r -band images were either taken from the SDSS or a dedicated program with the INT (Paper XXI). The CO synthesized beam is shown in the bottom-right corner of each panel. A bar in the bottom left corner of each panel indicates the scale of $10''$, as well as the equivalent physical scale at the distance of the galaxy.

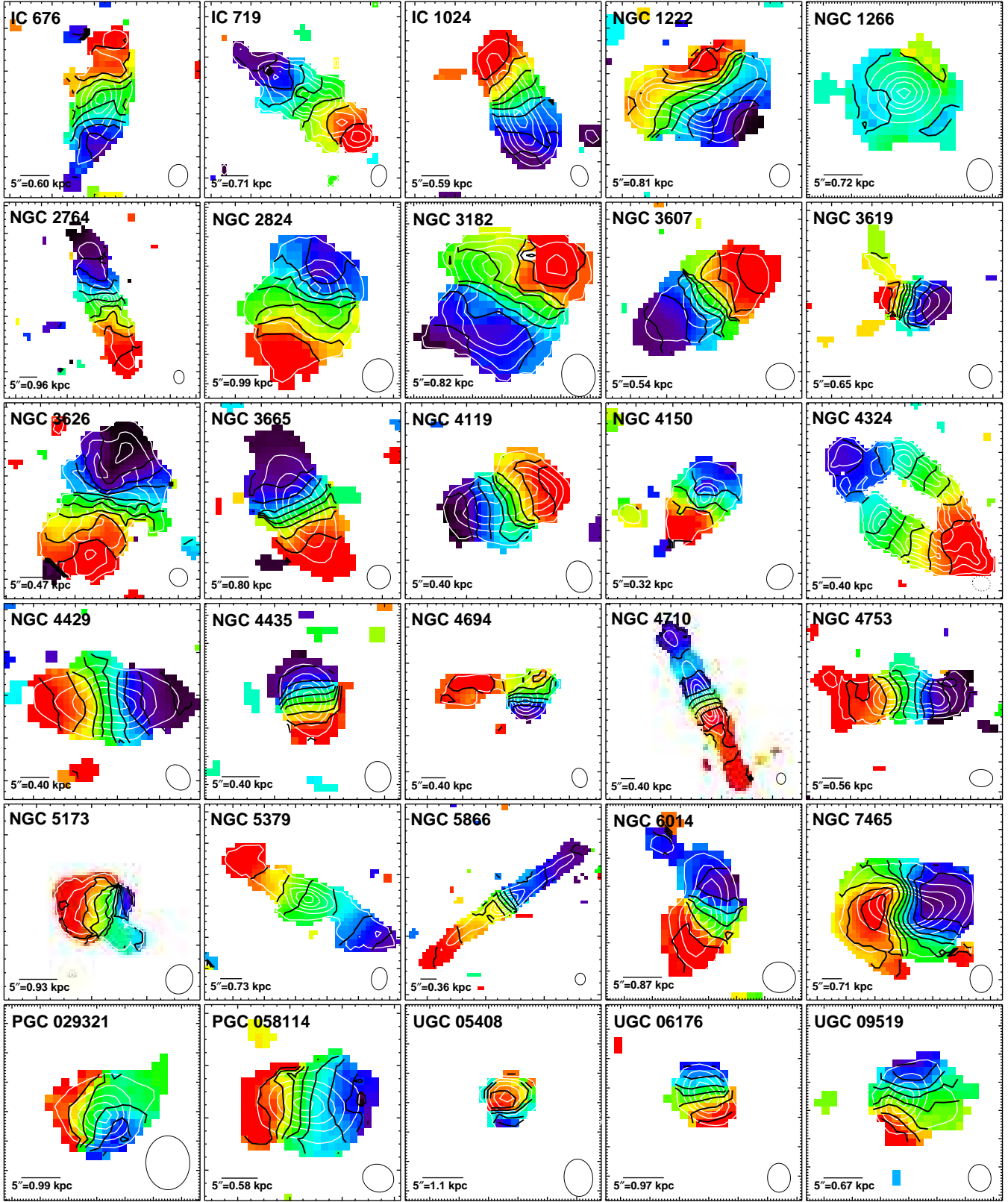


Figure 2. Mean CO(1–0) velocity maps of the 30 galaxies of the ATLAS^{3D} CARMA sample. Iso-velocity contours (black) are overlaid at 20 km s^{−1} intervals, as are contours from the moment0 map (white). The CO synthesized beam is shown at the bottom-right corner of each panel. A bar in the bottom left corner of each panel indicates the scale of 5'', as well as the equivalent physical scale at the distance of the galaxy.

3.5 Literature data

Twelve galaxies of the ATLAS^{3D} sample already have interferometric CO data available in the literature. Those galaxies are: NGC 4710 (Wrobel et al. 1992), NGC 2685 (Schinnerer & Scoville 2002), and the ten galaxies that will be part of the ATLAS^{3D} data release: NGC 4476 (Young 2002); NGC 3032, NGC 4150, NGC 4459 and NGC 4526 (Young, Bureau & Cappellari 2008); NGC 2768 (Crocker et al. 2008); NGC 4550 (Crocker et al. 2009); NGC 524, NGC 3489 and NGC 4477 (Crocker et al. 2011). Names, distances, Virgo membership, CO morphological classes and references of these galaxies are listed in Table 4. When required, data for each of the galaxies were provided by the original authors for use in this work. Moment maps and dust comparisons appear in Figure B1 for the galaxies whose data will be included in the data release. Both NGC 4710 and NGC 4150 were re-observed as part of the CARMA ATLAS^{3D} survey, and we only present these updated data in this paper.

3.6 Catalog of ATLAS^{3D} interferometric CO data

The CARMA data archive³ will include CARMA data for all 30 galaxies, as well as data for the 10 previously published galaxies and the two non-ATLAS^{3D} sources. The data products provided will include data cubes and moment0 and moment1 maps in FITS format. The data will also be reachable from the ATLAS^{3D} project website⁴.

4 DISCUSSION

Figures 1 and 2 show the 30 ETGs imaged as part of the CARMA ATLAS^{3D} survey. Before the survey was complete (which includes the 10 literature galaxies mentioned in §3.5), 16 ETGs had spatially-resolved CO maps (Wrobel et al. 1992; Schinnerer & Scoville 2002; Young 2002, 2005; Wei et al. 2010a; Young, Bureau & Cappellari 2008; Crocker et al. 2011), most obtained as part of individual or small-sample studies. The addition of the CO-imaged ATLAS^{3D} sources increases this amount to over 50, and provides a largely unbiased sample. Combined with the maps from the SAURON integral-field spectrograph, the CO-mapped ATLAS^{3D} galaxies thus provide the most robust picture of molecular gas-rich ETGs.

We now focus our analysis on the CO-rich ATLAS^{3D} ETGs only, adding the ten ATLAS^{3D} galaxies imaged in CO with the Berkeley-Illinois-Maryland Array (BIMA), the Owens Valley Radio Observatory (OVRO) and the Plateau de Bure Interferometer (PdBI) prior to the CARMA effort. Between the 30 CARMA galaxies and 10 previously published galaxies (excluding two overlapping objects; see Table 4), we imaged 40 galaxies or 65% of the CO detections in Paper IV, more than 90% of the total molecular gas mass in those detections, and are complete down to a CO(1–0) integrated flux of $18.5 \text{ Jy km s}^{-1}$.

4.1 Comparison to the dust

Figure 3 shows the CO moment0 contours of each galaxy overlaid on a $g - r$ colour image. The dust distributions are shown by creat-

Table 4. Properties of the ATLAS^{3D} literature galaxies

Name	Distance (Mpc)	Morph. class. ^a	Virgo membership	Reference
NGC 524	23.3	D	0	6
NGC 2685	16.7	R	0	1
NGC 2768	21.8	D	0	4
NGC 3032	21.4	D	0	3
NGC 3489	11.7	S	0	6
NGC 4459	16.1	D	1	3
NGC 4476	17.6	D	1	2
NGC 4477	16.5	R	1	6
NGC 4526	16.4	D	1	3
NGC 4550	15.5	D	1	5

References: (1) Schinnerer & Scoville (2002); (2) Young (2002); (3) Young, Bureau & Cappellari (2008); (4) Crocker et al. (2008); (5) Crocker et al. (2009); (6) Crocker et al. (2011)

Notes:

^aCO morphological classification based on the moment0 and moment1 maps. D = disc, X = strongly disrupted, R = ring, M = mildly disrupted, B = bar/ring, S=spiral.

ing $g - r$ colour SDSS images (and for NGC 1222 and NGC 7465, for which SDSS images are unavailable, on INT images, and for NGC 1266, on CTIO b and r band images from the SINGS survey; Kennicutt et al. 2003). In order to create the $g - r$ images, the Goddard IDL library task SKY was used to determine the background sky level, then subtracted from the images. The $g - r$ colour images were then created by dividing the sky-subtracted g -band image from the sky-subtracted r -band image. The $g - r$ imaging enhances the visibility of dust features by directly tracing extinction and provides a qualitative view of the distribution of the filamentary dust in each galaxy of the ATLAS^{3D} CARMA sample. This dust, for the most part, is a reasonable indicator of the distribution of the molecular gas.

For simplicity we refer to the $g - r$ colour images as “dust images” for the remaining text, even if they are intrinsically only representations of stronger dust-obscured regions. Indeed, the CO is nearly always (28/29 instances) associated with evidence of dust obscuration. It is evident that the converse is not true, as a Hubble Space Telescope (HST) survey of nearby ellipticals revealed that they contain dust in nearly half the cases (Tran et al. 2001; Lauer et al. 2005), much more than the CO detection rate of ATLAS^{3D}. Additional dust is seen beyond the limits of the detected CO emission in most galaxies, but notably in NGC 1266, NGC 3619, NGC 4150, NGC 4694 and NGC 4753. However, there is no noticeable dust beyond the detected extent of the CO in others. It thus appears that in most cases where the dust and CO are co-spatial, dust provides a good, high spatial resolution rendering of the molecular gas structure. Where dust is more extended than the CO, it could simply be that the outer CO is below our detection threshold, or that the ISM is not molecular at all (for instance, it could be atomic or warm). With this caveat in mind, we use the dust images as a useful guide to the morphological structures in which the cold ISM resides. We exploit this fact below when the CO morphological class is difficult to determine (e.g. IC 676 and NGC 4435).

4.2 Morphologies of the molecular gas

The CO-imaged ATLAS^{3D} survey illustrates that the molecular gas in ETGs comes in a large variety of morphologies. We have identified six different morphologies, including smooth discs (D),

³ <http://carma-server.ncsa.uiuc.edu:8181/>

⁴ <http://purl.org/atlas3d>

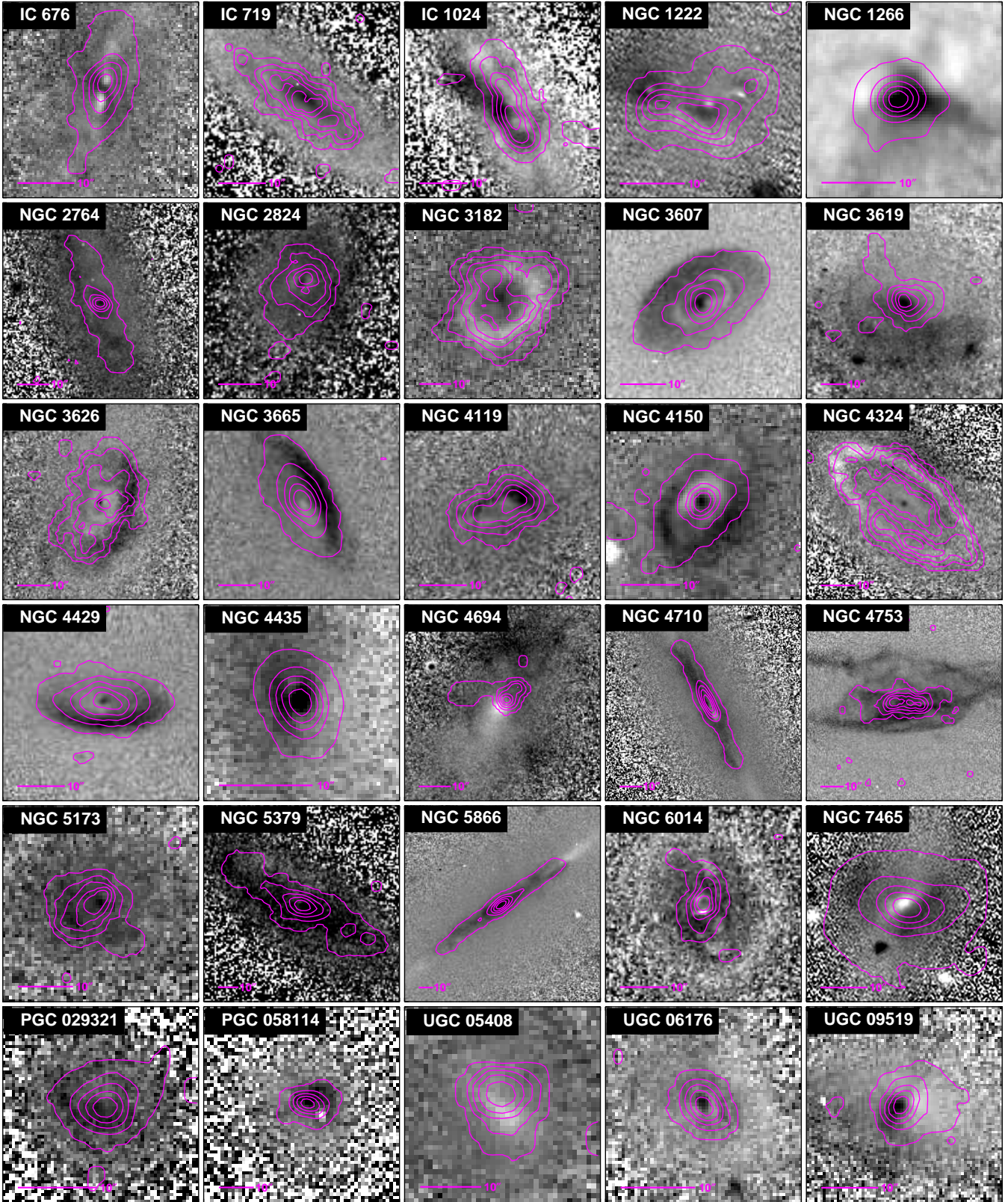


Figure 3. Comparison of the integrated CO(1–0) distribution (magenta contours) and the dust distribution as represented by $g - r$ colour images (grayscale) for the 30 galaxies of the ATLAS^{3D} CARMA sample. It appears that galaxies with disrupted CO morphologies also exhibit disturbance in the dust distribution, and overall the molecular gas in the galaxies traces the filamentary dust.

Table 5. CO morphologies of the ATLAS^{3D} interferometric sample.

Morphological configuration	Symbol	Number (out of 40)	Fraction (%)
Disc	D	20	50
Spiral	S	2	5
Ring	R	6	15
Bar+Ring	B+R	4	10
Mild disruption	M	5	12.5
Strong disruption	X	3	7.5

spirals (S), rings (R), bars+rings (B+R), as bars are always found with rings, never alone, mildly disrupted objects (M), and strongly disrupted objects (X). These classifications are strictly for the molecular gas, as all galaxies are optically-classified as ETGs. The CO morphological classification of each galaxy was based on an analysis of its moment0 and dust maps (Fig. 3), moment1 map (Fig. 2) and major-axis PVD (Figs. A1-30). In many cases the moment0 and moment1 map allowed us to unambiguously classify a galaxy. For ambiguous cases, the PVD was used to search for distinct kinematic signatures. Finally, the dust map was used as a higher spatial resolution proxy for the molecular gas.

The criteria for each CO morphological class are as follows. Galaxies classified as discs (D) show regular rotation and a smooth elliptical shape. The PVD of D-class objects also show smooth velocity variations with no discontinuity. Galaxies classified as spirals (S) show regular rotation, but the moment0 and/or dust maps exhibit discrete spiral arms. Galaxies classified as rings (R), like discs, exhibit regular rotation, but unlike discs, the PVD of R-class objects include a solid-body component and/or a discontinuity in velocity. Well-resolved rings show a central hole in the moment0 map. In the most ambiguous cases, the dust map was consulted to search for a dust ring (e.g. NGC 4119 and NGC 4435). Bar+Ring systems (B+R) were identified either directly from the moment1 map, when the bar and ring are both distinctly visible, or using the PVD and searching for an X-shaped pattern (in the case of edge-on systems; see §4.2.2). Galaxies classified as mildly disrupted (M) have mainly regular disc morphologies, but include small deviations in their moment0 and moment1 maps. Finally, a galaxy is classified as strongly disrupted (X) for showing strong irregularities in the CO kinematics.

4.2.1 Strongly and mildly disrupted objects

The origin of the strongly disrupted (X) objects is the most easily explained. These galaxies show highly irregular CO distributions and kinematics, that are normally characteristic of interacting systems, a fact often confirmed by observations at other wavelengths. In the case of NGC 1222 and NGC 4694, it is clear that they acquired their gas via external accretion (see Beck et al. 2007 and Duc et al. 2007 for details on each galaxy). NGC 5173 is known to host a large misaligned H I disk (Paper XIII).

Mildly disrupted CO distributions (M) also appear to be in less relaxed systems than the rest. In some cases, there is strong evidence that the gas is being acquired externally, such as in NGC 7465 (Li & Seaquist 1994), which is accreting from an external H I reservoir via a close interaction with other galaxies. NGC 3619 and UGC 09519 are known to host large misaligned H I discs (Paper XIII), providing a likely source for the molecular gas. The irregular dust filaments in NGC 4753 are the main reason that the CO is classified as an M morphology.

The NGC 4753 dust structure is well explained by a precessing twisted disc after the accretion of a gas-rich dwarf companion (Steiman-Cameron et al. 1992). The original BIMA observations of NGC 4150 (Young, Bureau & Cappellari 2008) show a pronounced low-surface density elongated tail that was not recovered by CARMA, both due to a smaller field of view and higher spatial resolution. A study of the gas-phase metallicity of NGC 4150 also show it to be sub-Solar ($Z \approx 0.3 - 0.5 Z_{\odot}$), therefore the molecular gas is likely to originate from an external accretion event (Crockett et al. 2011).

It appears that field galaxies are far more likely to exhibit disrupted morphologies than Virgo cluster galaxies, with $24 \pm 8\%$ (7/29) of field galaxies classified as either M or X as opposed to $9 \pm 9\%$ (1/11) for Virgo galaxies. This is not surprising given the results of Paper X, which suggested that galaxies virialised within the cluster are unable to replenish their stores of molecular gas via external accretion, and thus only longer-lived phenomena survive, such as bars and rings. Overall, the M- and X-class objects seem to host gas that has an external origin, and they are probably dynamically younger than the other objects, explaining the dearth of such objects within Virgo.

4.2.2 Molecular rings and bars

Rings (R) and bars+rings (B+R) also make up a non-negligible fraction of the ATLAS^{3D} molecular gas morphologies, representing about a fifth (8/40) of the CO sample. It is of note that cold gas in barred galaxies accumulates in rings associated with the major resonances (e.g. Buta & Combes 1996), so it is possible that bar+ring systems are simply in an early stage of an evolutionary sequence, whereby the bar funnels gas into the centre (e.g. Bournaud & Combes 2002), evacuating the central (but not nuclear) regions of molecular gas, and later leaving the ring structure intact, without a molecular gas-rich bar. This scenario would explain why bars are only seen with rings, but not the converse.

Figure 4 shows the PVDs of three galaxies (NGC 2764, NGC 4710 and NGC 5866) that possess two velocity components along the line-of-sight. All three galaxies are edge-on, and the characteristic X-shaped PVDs observed are normally associated with the kinematic signature of a bar in an edge-on disc. The material in the inner rapidly-rising component of each PVD is associated with gas on x_2 orbits (elongated perpendicular to the bar and located within the inner Lindblad resonance, ILR), while the material in the outer slowly-rising component is associated with gas on nearly circular orbits beyond corotation. The intermediate region has been largely swept free of gas by the bar, due to inflows toward the ILR (see Sellwood et al. 1993 for a review of bar dynamics). The signature is analogous to that of the Milky Way bar in a Galactic longitude-velocity diagram. It was first proposed in external galaxies by Kuijken & Merrifield (1995), later refined by Bureau & Athanassoula (1999) and Athanassoula & Bureau (1999), who both identified multiple examples observationally (Merrifield & Kuijken 1999; Bureau & Freeman 1999). The bar signatures in NGC 2764 and NGC 5866 are observed here for the first time, but that in NGC 4710 was previously observed in CO by Wrobel et al. (1992). The link between bars and boxy-shaped bulges (such as that in NGC 4710) has long been established, but the presence of a bar in NGC 5866 is rather unexpected given its large classical bulge (see Athanassoula 2005 for the different bulge types and the bar-boxy bulge relationship).

The fraction of molecular gas-rich ETGs (6/40) that contain a ring structure is also a factor of ≈ 2 larger than that of LTGs, based

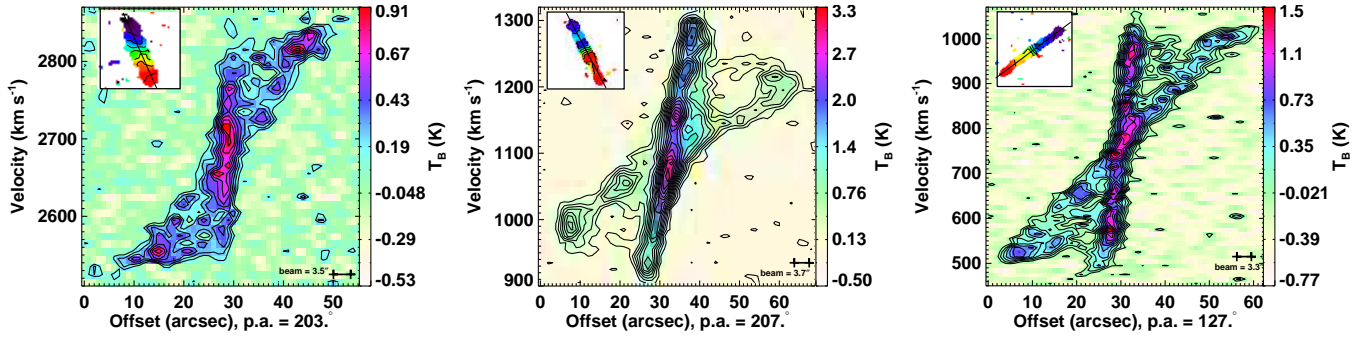


Figure 4. Position-velocity diagrams of the three CARMA ATLAS^{3D} ETGs with clear two-component velocity profiles, that are not properly represented by the moment1 maps. The galaxies are NGC 2764 (left), NGC 4710 (middle) and NGC 5866 (right). All 3 galaxies are edge-on or almost edge-on and show the characteristic X-shaped PVD signature of an edge-on bar (see §4.2.2)

on the BIMA Survey of Nearby Galaxies (SONG) sample (3/39; Sheth et al. 2002; Helfer et al. 2003) modified to match the average noise and redshift of the ATLAS^{3D} sample (as in Paper XIV and §4.2.3). Also, unlike for LTGs, the molecular gas morphology does not necessarily follow the stellar morphology, most notably stellar bars. Galaxies with stellar bars identified in Paper II are as likely to have a disc-like (D) CO morphology as R and B+R morphologies.

It also appears that Virgo cluster galaxies are slightly more likely to have R and B+R structures than field galaxies, with $45 \pm 15\%$ (5/11) of Virgo galaxies classified as either R or B+R, as opposed to $17 \pm 7\%$ (5/29) for field galaxies. Paper X has shown that the molecular gas in ETGs is preferentially kinematically-aligned with the stars in Virgo galaxies, so it is perhaps not surprising to find relatively more bars and rings there, where the gas has been under the influence of secular processes without external gas interference for some time. This may also point to these morphologies being long-lived, as opposed to the M and X morphologies discussed above. It is also quite possible that the slightly higher detection rate of R and B+R structures in Virgo with respect to the field galaxies is due to a spatial resolution effect, as Virgo galaxies are closer on average ($D \approx 16.5$ Mpc; Mei et al. 2007) than the field galaxies in the sample ($D \approx 28$ Mpc). If we redshift the Virgo galaxies to the average distance of field galaxies, the detection rate of R and B+R structures drops from 45 to 18% and is then statistically consistent with the field rate (NGC 4119, NGC 4435 and NGC 4477 become unresolved). Higher resolution and deeper imaging is required to determine whether the higher rate in Virgo is truly a resolution effect or an intrinsic property.

4.2.3 Molecular discs and spirals

Smooth molecular discs make up the largest fraction of the CO morphologies that are seen in the CO-imaged ATLAS^{3D} galaxies, while spirals make up the smallest fraction. This relative dearth of discrete spirals as compared to smooth discs seems to indicate that there is something fundamentally different about the way in which molecular gas behaves within an ETG as opposed to a LTG. A caveat to this scenario is that galaxies with dominant molecular gas spirals (and associated star formation) would likely be classified as LTGs, and thus be excluded from the sample.

It is possible that molecular gas in ETGs remains in a smooth distribution and lacks distinct spiral arms for dynamical reasons. For example, the steep potential wells in the central parts of ETGs (where the molecular gas resides) yield high epicyclic frequencies,

and may thus prevent gravitational instabilities linked to spiral arms from developing (Toomre Q parameter; e.g. Toomre 1981).

It is also possible that some of the D morphologies would have been classified otherwise with observations of better sensitivity and/or spatial resolution. For instance, much higher spatial resolution CO observations of NGC 1266 presented in Alatalo et al. (2011) reveal a disrupted nuclear disc and a molecular outflow, both of which are unresolved here. In addition, if only the peak of a spiral structure were detected, and convolved with a large beam, it could well be classified as a disc. In fact, as much as half of BIMA SONG spirals (Helfer et al. 2003) would be classified as D if they were located at the average distance of the ATLAS^{3D} sample, with similar noise properties and beam sizes (see Paper XIV for a full discussion of properly redshifting the BIMA SONG data to match ATLAS^{3D}). However, even assuming that half of the current CO-rich ETGs classified as D actually harbour spatially-unresolved spirals, the spiral fraction of ATLAS^{3D} galaxies would be $30 \pm 7\%$, still much lower than the spiral fraction of BIMA SONG galaxies ($62 \pm 10\%$).

While obtaining higher resolution molecular gas maps is the only rigorous way to directly break the S/D degeneracy, we use here the unsharp-masked dust images as proxies. As mentioned in §4.1, the molecular gas morphology follows the dust morphology faithfully in the majority of cases. The unsharp-masked images therefore may be utilized to provide the higher spatial resolution and sensitivity required to separate the S and D classifications. The dust comparison indicates that in the majority of cases (with the possible exceptions of NGC 3619, NGC 3626 and NGC 3665), and contrary to LTGs, a disc morphology without distinct spiral arms is indeed the most common morphology for the molecular gas in ETGs.

4.2.4 Summary of the gas morphologies

Table 5 lists the total number of ATLAS^{3D} ETGs within each CO morphological class. Overall, it thus appears that the CO in ETGs is most likely to be in a settled morphology, either in regular discs (comprising 50% of the galaxies) or ring, bar+ring and spiral morphologies (comprising another 30% of the sample). This means that the majority (80%) of ETGs have a dynamically settled molecular gas morphology. The dynamically unsettled (M and X) systems comprise the remaining 20%, and just over half of those are only mildly disrupted. Of course, the CO structures observed here are rather compact spatially, with an average extent of only 1 kpc (Paper XIV), and have correspondingly small dynamical timescales

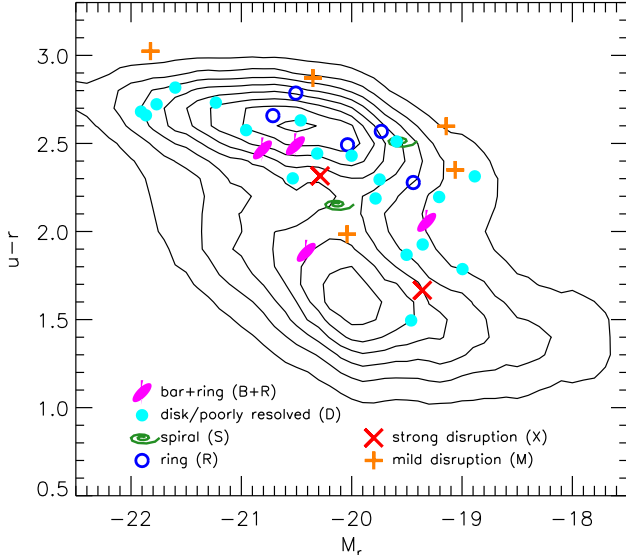


Figure 5. Color-magnitude diagram of the CO-imaged ATLAS^{3D} galaxies, sorted based on the CO morphological classifications. The contours (black) are from the SDSS Data Release 8 (DR8; Aihara et al. 2011), and represent all galaxies with redshift $z > 0.08$. Data for the ATLAS^{3D} ETGs are either from the SDSS DR8 u , r and M_r catalog products or the INT (NGC 524, NGC 3489 and NGC 7465; Paper XXI). Colour information is unavailable for NGC 1222 and NGC 1266 due to poor u -band photometry, for PGC 058114 because of the presence of a bright star less than a degree from the galaxy, and for NGC 4710 due to erroneous SDSS photometry.

($10^7 - 10^8$ yrs). The CO distributions are thus expected to relax and reach equilibrium rapidly.

Figure 5 shows the $u - r$ vs. M_r color-magnitude diagram (CMD) of the CO-imaged ATLAS^{3D} sample, from SDSS and INT data, overlaid upon the SDSS Data Release 8 distribution of all galaxies with redshift $z > 0.08$ (Aihara et al. 2011). There is no clear separation of the morphological groups, although some trends do appear. The brightest objects ($M_r < -21$) tend to be classified as D galaxies, with the exception of NGC 4753, which was discussed in §4.2.1. The CO discs in these massive galaxies are also generally well-resolved, limiting the chance that these objects are poorly resolved rings or spirals. It also appears that although B+R galaxies can be found throughout the CMD, galaxies classified as R only seem to cluster on the red sequence, perhaps indicating a later evolutionary stage.

4.3 CO spectral asymmetries

It is worth mentioning that a fraction of the CO spectra exhibit asymmetries, and have representatives in many CO morphological classes (as opposed to solely M and X-class objects). Although asymmetries detected from a single-dish spectrum could be due to a slightly offset pointing, interferometric identifications of spectral asymmetries are more robust. Asymmetric spectra have long been known within H I discs (Baldwin et al. 1980). Within the Westerbork H I sample of Spiral and Irregular Galaxies (WHISP) at least 80% of all galaxies contain some amount of asymmetry (van Eymeren et al. 2011). In fact, asymmetries are found at small radii in at least 60% of H I discs from the WHISP survey. Despite the different dynamical timescales at the radii where the CO has been found, finding a few asymmetric objects within the CARMA ATLAS^{3D} sample is unsurprising.

Asymmetric H I spectra generally trace lopsided spatial distributions, and lopsided molecular gas discs are likely a result of the molecular gas responding to a change in the gravitational potential. In particular, long-lived lopsided H I discs are well reproduced in models where the gas is off-centre with respect to the galactic halo (e.g. Levine & Sparke 1998). Other possible causes for lopsidedness include responding to an interaction (e.g. Jog & Combes 2009), or possibly an internal instability that perturbs both the $m = 1$ (lopsided) and $m = 2$ (barred) modes (Masset & Tagger 1997; Bournaud et al. 2005; Jog & Combes 2009). In the strongest case of asymmetry (IC 1024), it is likely that the molecular gas disc is responding to a tidal interaction, which is also seen in the optical data (Paper II). IC 1024, despite being lopsided, is dynamically relaxed (Paper XIV) and shows regular kinematics and a CO disc morphology in the moment0 map. This may suggest that the tidal interaction happened sufficiently long ago for any detectable morphological and kinematic disturbance of the molecular gas to subside, while preserving the spectral asymmetry.

In the context of H I, the structures are well resolved, extended, and clearly “lopsided”, and the H I cloud size is small compared to the global structure, and thus inferences can be made in most cases that the driver of the asymmetries are global, on a long timescale. Structures traced by the CO distributions are much less extended compared to the rest of the galaxy (Paper XIV), and thus the interpretation of CO asymmetries is less straightforward. A more comprehensive study of asymmetries and lopsidedness in CO distributions within galaxies would likely address these issues, as well as uncover many other yet unstudied properties of molecular gas distributions in galaxies, but is beyond the scope of this paper.

4.4 Mass of externally-acquired molecular gas in ETGs

Paper X discusses the origins of the molecular gas in ETGs, and identifies galaxies that likely have externally-acquired gas. Using the criteria set forth in Paper X, that the kinematic major axis of the ionized gas must be misaligned with the kinematic major axis of the stars by at least 30° , at least thirteen CO-imaged ATLAS^{3D} galaxies are identified as having externally-acquired gas: IC 719, NGC 1266, NGC 2685, NGC 2768, NGC 3032, NGC 3626, NGC 4694, NGC 5173, NGC 7465, PGC 029321, PGC 058114 and UGC 09519. NGC 3619 is classified as M in this work, exhibiting an unsettled CO morphology, but the origin of the CO is difficult to determine, with a kinematic misalignment angle of only $24 \pm 3^\circ$, right at the boundary of being classified as external (Paper X), and the galaxy contains a kinematically-misaligned H I disc (Paper XIII). Although it is possible that the CO indeed has an external origin, there is no conclusive measurement to classify it as such, and NGC 3619 will not be considered as having external CO in the following discussion. The CO of NGC 4150 is included here as being external in origin, as studies show that its gas-phase metallicity is sub-Solar, and thus is very likely from the accretion of a gas-rich companion in a minor merger (Crockett et al. 2011). NGC 4753 is classified as M in this work, and Steiman-Cameron et al. (1992) make a compelling argument that the molecular disc is unsettled, and must come from an external source. For this reason, we include here NGC 4753 in the category of gas acquired externally. The disrupted stellar and gas kinematics of NGC 1222 (CO class X), which is currently undergoing a strong three-way interaction (Beck et al. 2007), also suggest that the molecular gas is likely to be of external origin. Including these three additions, 15 (38%) of the 40 gas-rich CARMA ETGs contain external gas, in good agree-

ment with the fraction of externally-acquired gas estimated in Paper X (36%).

The fact that the majority of galaxies with unsettled gas morphologies are identified as having an external gas origin is unsurprising, as a parcel of gas falling into a galaxy takes time to virialise, which is not the case for internal gas (stellar mass loss). The rest of the galaxies with external gas have disc morphologies (IC 719, NGC 3032, NGC 3626, PGC 029321 and PGC 058114), represented at about the same rate as in the sample as a whole. NGC 2685 and NGC 2768 are both known polar rings/discs, and are discussed in detail in Schinnerer & Scoville (2002) and Crocker et al. (2008), respectively.

We use the H₂ masses from CARMA, where available, and find that the sum of the molecular gas masses in the 15 sources with external CO is $8.26 \times 10^9 M_{\odot}$, assuming $X_{\text{CO}} = 3 \times 10^{20} (\text{K km s}^{-1})^{-1} \text{ cm}^{-2}$ (Dickman, Snell & Schloerb 1986), and accounts for 44% of the total molecular gas mass in our sample of 40 CO-rich galaxies with interferometric maps. There is reasonable agreement between the external number (38%) and mass (44%) fractions. We note that these fractions are lower limits, due to the fact that we can only unambiguously assign galaxies with misaligned stellar and gas kinematics as external accretors, while some fraction of aligned galaxies are also likely to be so.

Galaxies that were originally detected in molecular gas (Paper IV) but were not mapped interferometrically have a higher rate of ionised gas kinematically-aligned with the stars, compared to those actually mapped here (i.e. brighter CO; see Paper X). This likely means that the un-imaged CO-detected ETGs contribute negligibly (< 6%) to the total external molecular gas mass. It is also likely that undetected galaxies do not contribute significantly to the total gas mass, with an upper limit to the contribution of $\approx 3 \times 10^9 M_{\odot}$, assuming that 42.5% upper limits in undetected field galaxies are due to an external phenomenon (Paper X).

Assuming the molecular gas is depleted through star formation and reasonable gas depletion timescales (≈ 1 Gyr; Saintonge et al. 2011) and star formation histories (allowing us to adopt the mean current-to-initial molecular gas mass correction factor calculated by Kaviraj et al. 2012 for ETGs with prominent dust lanes), we can infer the amount of molecular gas each galaxy acquired before star formation activity consumed some of the molecular gas. The total amount of molecular gas originally acquired externally within the ATLAS^{3D} sample is then approximately $2.48 \times 10^{10} M_{\odot}$. At the rate of 30 minor mergers in the sample detailed in §1 and from the rate of Lotz et al. (2008), this would mean approximately $8.3 \times 10^8 M_{\odot}$ of H₂ per minor merger per molecular gas depletion time (1 Gyr; Saintonge et al. 2011). We derive an average stellar mass ratio for these minor mergers by first converting the molecular gas mass to an atomic mass using the 1:3 H₂-to-H I ratio seen in the Milky Way (Wolfire et al. 2003). We then use the average H I-to-stellar mass fraction of minor merger companions from Kannappan (2004) of 20% to calculate the average stellar mass of the accreted companions, $1.25 \times 10^{10} M_{\odot}$. For the mass of the accreting galaxy, we take the average stellar mass of the non-Virgo ETGs in the CO-imaged ATLAS^{3D} sample, $\approx 6.5 \times 10^{10} M_{\odot}$. This results in a merger stellar mass ratio of 1:5.2, consistent with the minor merger stellar mass ratios we expect. We therefore conclude that our results are in good agreement with the origin of the external gas being due to minor mergers.

5 CONCLUSIONS

We have presented millimeter-wave data products as part of the CARMA ATLAS^{3D} survey of galaxies, an imaging survey of the CO J = 1–0 emission of 30 nearby CO-rich ETGs, part of the ATLAS^{3D} survey. The main conclusions drawn from these data are:

1. The CO-imaged ATLAS^{3D} survey is the largest CO imaging survey of ETGs to date, and provides the most detailed view of the nature of molecular gas in ETGs.

2. The molecular gas found in ETGs appears to be co-spatial with dust features (as traced by $g - r$ colour images), though the dust features often appear to be more extended, likely because we are unable to trace small molecular gas surface densities.

3. The molecular gas present in ETGs comes in a variety of morphologies: 50% of the objects have their CO in inclined gas discs or is poorly resolved structures (D), 5% show spiral arms or spiral structure (S), 15% have resolved rings (R), 10% have bar+ring systems (B+R), 12.5% have mildly disrupted distributions (M) and 7.5% have strongly disrupted distributions (X).

4. The CO morphology does not show a strong correlation with the $u - r$ color or total magnitude of the galaxy, although there appear to be weak trends. For example, the most massive galaxies in this sample tend to have D CO morphologies, and R morphologies tend to lie on the red sequence whereas B+R morphologies tend to also be present in the blue cloud.

5. We currently observe a total of $8.26 \times 10^9 M_{\odot}$ of molecular gas that is likely of external origin in 15/40 of our galaxies. Using the correction factor derived in Kaviraj et al. (2012), we estimate that the total externally acquired molecular gas prior to the consumption of some of it by star formation was $\approx 2.48 \times 10^{10} M_{\odot}$. In conjunction with the minor merger rate of Lotz et al. (2008) and assumptions about gas mass fractions, this amount of externally accreted molecular gas is consistent with a minor merger origin.

6. The CARMA ATLAS^{3D} (as well as 9 additional literature galaxy) data products including data cubes and moment0 and moment1 maps in FITS format, will be publicly released and hosted through the CARMA data archive⁵ and will be reachable from our project website⁶.

ACKNOWLEDGMENTS

We thank the anonymous referee for insightful comments and suggestions. K.A. thanks C. Heiles, K. Nyland, G. Graves, R. Plambeck, E. Rosolowsky and J. Carpenter for useful conversations. K.A. also wants to thank Lisa Wei in particular for collaboration on NGC 5173. The research of K. Alatalo is supported by the NSF grants AST-0838258 and AST-0908572. The research of K. Alatalo is also supported by NASA grant HST-GO-12526. MC acknowledges support from a STFC Advanced Fellowship (PP/D005574/1) and a Royal Society University Research Fellowship. PS is a NWO/Veni fellow. RMCD is supported by the Gemini Observatory, which is operated by the Association of Universities for Research in Astronomy, Inc., on behalf of the international Gemini partnership of Argentina, Australia, Brazil, Canada, Chile, the United Kingdom, and the United States of America. RLD and MB are supported by the rolling grants ‘Astrophysics at Oxford’

⁵ <http://carma-server.ncsa.uiuc.edu:8181/>

⁶ <http://purl.org/atlas3d>

PP/E001114/1 and ST/H002456/1 from the UK Research Councils. RLD acknowledges travel and computer grants from Christ Church, Oxford and support from the Royal Society in the form of a Wolfson Merit Award 502011.K502/jd. TN acknowledges support from the DFG Cluster of Excellence: "Origin and Structure of the Universe." Support for CARMA construction was derived from the states of California, Illinois, and Maryland, the James S. McDonnell Foundation, the Gordon and Betty Moore Foundation, the Kenneth T. and Eileen L. Norris Foundation, the University of Chicago, the Associates of the California Institute of Technology, and the National Science Foundation. Ongoing CARMA development and operations are supported by the National Science Foundation under a cooperative agreement, and by the CARMA partner universities. This paper is partly based on observations carried out with the IRAM 30m telescope. IRAM is supported by INSU/CNRS (France), MPG (Germany) and ING (Spain). We acknowledge use of the HYPERLEDA database (<http://leda.univ-lyon1.fr>) and the NASA/IPAC Extragalactic Database (NED) which is operated by the Jet Propulsion Laboratory, California Institute of Technology, under contract with the National Aeronautics and Space Administration.

REFERENCES

- Aihara H., Allende Prieto C., An D., et al., 2011, *ApJS*, 193, 29
 Alatalo, K. et al., 2011, *ApJ*, 735, 88
 Athanassoula, E., 2005, *MNRAS*, 358, 1477
 Athanassoula, E., Bureau, M., 1999, *ApJ*, 522, 699
 Baldry, I. K. et al., 2004, *ApJ*, 600, 681
 Baldwin, J. E., Lynden-Bell, D., Sancisi, R. 1980, *MNRAS*, 193, 313
 Bauermeister, A., et al. 2012, CARMA Memo, No. 59 (http://www.mmarray.org/memos/carma_memo59.pdf)
 Beck, S. C., Turner, J. L., Kloosterman, J., 2007, *AJ*, 134, 1237
 Bigiel, F. et al., 2008, *AJ*, 136, 2846
 Böhringer, H. et al., 1994, *Nature*, 368, 828
 Bournaud, F., Combes, F., 2002, *A&A*, 392, 83
 Bournaud, F., Combes, F., Jog, C. J., Puerari, I., 2005, *A&A*, 438, 507
 Bower, R. G., Lucey, J. J., Ellis, R. S., 1991, *MNRAS*, 254, 601
 Bureau M., Athanassoula E., 1999, *ApJ*, 522, 686
 Bureau M., Freeman K. C., 1999, *AJ*, 118, 126
 Buta, R., Combes, F., 1996, *FCPh*, 17, 95
 Cappellari, M. et al., 2011a, *MNRAS*, 413, 813; Paper I
 Cappellari, M. et al., 2011b, *MNRAS*, 416, 1680; Paper VII
 Cayatte, V., van Gorkom, J. H., Balkowski, C., Kotanyi, C., 1990, *AJ*, 100, 604
 Ciotti, L., D'Ercole, A., Pellegrini, S., Renzini, A., 1991, *ApJ*, 376, 380
 Combes, F., Young, L. M., Bureau, M., 2007, *MNRAS*, 377, 1795
 Crocker, A. C., Bureau, M., Young, L. M., Combes, F., 2008, *MNRAS*, 368, 1811
 Crocker, A. C. et al., 2009, *MNRAS*, 393, 1255
 Crocker, A. C. et al., 2011, *MNRAS*, 410, 1197
 Crocker, A. C. et al., 2012, *MNRAS*, 421, 1298; Paper XI
 Crockett, R. M. et al., 2011, *ApJ*, 727, 115
 Davis, T. A. et al., 2011a, *MNRAS*, 414, 968; Paper V
 Davis, T. A. et al., 2011b, *MNRAS*, 417, 882; Paper X
 Dickman, R. L., Snell, R. L., Schloerb, F. P. 1986, *ApJ*, 309, 326
 Duc, P.-A., Braine, J., Lisenfeld, U., Brinks, E., Boquien, M., 2007, *A&A*, 475, 187
 Duc, P.-A. et al., 2011, *MNRAS*, 417, 863; Paper IX
 Faber, S. M., Gallagher, J. S., 1976, *ApJ*, 204, 365
 Faber, S. M. et al., 2007, *ApJ*, 665, 265
 Giovanelli, R. et al., 2005, *AJ*, 130, 2598
 Harker, J. J., Schiavon, R. P., Weiner, B. J. Faber, S. M., 2006, *ApJL*, 647, L103
 Hawarden, T. G. et al., 1981, *MNRAS*, 196, 747
 Helfer, T. T. et al., 2003, *ApJS*, 145, 259
 Hubble, E., 1926, *ApJ*, 64, 321
 Jeong, H. et al., 2009, *MNRAS*, 398, 2028
 Jura, M., 1986, *ApJ*, 306, 483
 Jog, C. J., Combes, F. 2009, *Physics Reports*, 471, 75
 Kannappan, S. J., 2004, *ApJL*, 611, 89
 Kaviraj, S., et al. 2012, *MNRAS*, 423, 49
 Kennicutt, R. C., 1998, *ApJ*, 498, 541
 Kennicutt, R. C. et al. 2003 *PASP*, 115, 928
 Knapp, G. R., Turner, E. L., Cuniffe, P. E., 1985, *AJ*, 90, 3
 Knapp, G. R., Guhathukarta, P., Kim, D.-W., Jura, M., 1989, *ApJS*, 70, 329
 Krajnović, D. et al., 2011, *MNRAS*, 414, 2923
 Kuijken K., Merrifield M. R., 1995, *ApJ*, 443, L13
 Lauer, T. R. et al. 2005, *AJ*, 129, 2138
 Lees, J. F., Knapp, G. R., Rupen, M. P., Phillips, T. G. 1991, *ApJ*, 379, 177
 Levine, S. E., Sparke, L. S. 1998, *ApJL*, 496, 13
 Li, J. J., Seaquist, E. R., 1994, *AJ*, 107, 1953
 Lotz, J. M. et al., 2008, *ApJ*, 672, 177
 Lotz J. M. et al., 2011, *ApJL*, 742, 103
 Martig, M., Bournaud, F., Teyssier, R., Dekel, A., 2009, *ApJ*, 707, 250
 Masset, F., Tagger, M. 1997, *A&A*, 322, 442
 Mei, S. et al. 2007, *ApJ*, 655, 144
 Merrifield M. R., Kuijken K., 1999, *A&A*, 345, L47
 Morganti, R. et al., 2006, *MNRAS*, 371, 157
 Oosterloo, T. et al., 2010, *MNRAS*, 409, 500
 Sage, L. J., Wrobel, J. M., 1989, *ApJ*, 344, 204
 Sage, L. J., Galletta, G., 1993, *ApJ*, 419, 544
 Sage, L. J., Welch, G. A., 2006, *ApJ*, 644, 850
 Sage, L. J., Welch, G. A., Young, L. M., 2007, *ApJ*, 657, 232
 Saintonge, A. et al. 2011, *MNRAS*, 415, 61
 Sault, R. J., Teuben, P. J., Wright, M. C. H., 1995, *ASPC*, 77, 433
 Schinnerer, E., Scoville, N., 2002, *ApJL*, 577, 103
 Sellwood J. A., Wilkinson A., 1993, *Reports Prog. Phys.*, 56, 173
 Serra, P., et al., 2012, *MNRAS*, 422, 1835; Paper XIII
 Shapiro, K. L. et al., 2010, *MNRAS*, 402, 2140
 Sheth, K. et al. 2002, *AJ*, 124, 2581
 Springel, V., Di Matteo, T., Hernquist, L., 2005, *MNRAS*, 361, 776
 Steiman-Cameron, T. Y., Kormendy, J., Durisen, R. H., 1992, *AJ*, 104, 4
 Tonry, J. L. et al. 2001, *ApJ*, 546, 681
 Toomre, A., Toomre, J., 1972, *ApJ*, 178, 623
 Toomre, A. 1981, in *The Structure and Evolution of Normal Galaxies*, ed. S. M. Fall & D. Lynden-Bell (Cambridge : Cambridge Univ. Press), 111
 Tran, H. D. et al., 2001, *AJ*, 191, 2928
 van Eymeren, J., Jütte, E., Jog, C. J., Stein, Y., Dettmar, R.-J. 2011, *A&A*, 530, 29
 Visvanathan, N., Sandage, A., 1977, *ApJ*, 216, 214
 Wei, L. H., Vogel, S. N., Kannappan, S. J., Baker, A. J., Stark, D. V., Laine, S., 2010, *ApJL*, 725, 62

- Wei, L. H., Kannappan, S. J., Vogel, S. N., Baker, A. J., 2010, ApJ, 708, 841
- Welch, G. A., Sage, L. J., 2003, ApJ, 584, 260
- Welch, G. A., Sage, L. J., Young, L. M., 2010, ApJ, 735, 100
- Wolfire, M. G., McKee, C. F., Hollenbach, D., Tielens, A. G. G. M., 2003, ApJ, 587, 278
- Wrobel, J. M., Kenney, J. D. P. 1992, ApJ, 399, 94
- Young, L. M., 2002, AJ, 124, 788
- Young, L. M., 2005, ApJ, 258, 271
- Young, L. M., Bureau, M., Cappellari, M., 2008, ApJ, 676, 317
- Young, L. M., Bendo, G. J., Lucero, D. M., 2009, AJ, 137, 3053
- Young, L. M. et al., 2011, MNRAS, 414, 940; Paper IV

APPENDIX A: CO CARMA DATA OF ATLAS^{3D} GALAXIES

For each galaxy of the CARMA ATLAS^{3D} sample, we provide six figures:

Top-left: *r*-band image (grayscale) either from SDSS or from the INT, overlaid with black contours. The CO integrated intensity (moment0) map is also overlaid (cyan contours corresponding to 20, 40, 60, 80 and 100% of the peak). The cyan box corresponds to the size of the individual moment maps in the middle-left and middle-centre panels.

Top-right: Comparison of the single-dish IRAM 30m CO(1–0) integrated flux (black) and the CARMA integrated flux (red). The total integrated CARMA flux is obtained by summing all flux above a given threshold (see §3.3). The grey dashed vertical lines indicate the total spectral range of CARMA. Both heliocentric velocities and velocities with respect to systemic (taken from Paper I) are indicated. The rms noise is shown as a single error bar in black for the IRAM 30m and red for CARMA.

Middle-left: CO(1–0) integrated intensity (moment0) map (colorscale), overlaid with black and grey contours (at equal increments of 20% of the peak). The colour table on the right provides the integrated flux scale. The dot-dashed gray circle corresponds to the 21''6 primary beam of the IRAM 30m telescope. The CARMA synthesized beam is shown in the bottom-right corner (black ellipse).

Middle-center: CO(1–0) mean velocity (moment1) map (colorscale and black contours at 20 km s^{−1} intervals unless otherwise stated). The colour table on the right provides the velocity scale with respect to the systemic velocity (taken from Paper I and indicated in the top-left corner of the panel). The dot-dashed gray circle corresponds to the 21''6 primary beam of the IRAM 30m telescope. The CARMA synthesized beam is shown in the bottom-right corner (black ellipse).

Middle-right: CO(1–0) position-velocity diagram (PVD) taken over a one synthesized beam width (5 pixels) slice at the position angle indicated in the top-right corner inset and at the bottom of the panel (see §3.3). Velocities are heliocentric. The synthesized beam along the PV slice direction is indicated in the bottom-right corner. Contours are spaced by 1 σ starting at 3 σ (unless otherwise stated), where σ is the rms noise in an individual channel multiplied by $\sqrt{5}$, to account for the summation over the synthesized beam width.

Bottom: CO(1–0) channel maps. The panels for velocity channels with flux are color-coded based on their velocity with respect to systemic (taken from Paper I). The mean velocity offset is listed in the top-left corner of each panel. The cross indicates a fixed reference position in all panels. Contours are spaced by 1 σ beginning at $\pm 2\sigma$ (unless otherwise stated), where 1 σ is the rms noise in an individual channel. Grey contours are negative. The CARMA synthesized beam is shown in the lower-right corner of the first panel (black ellipse).

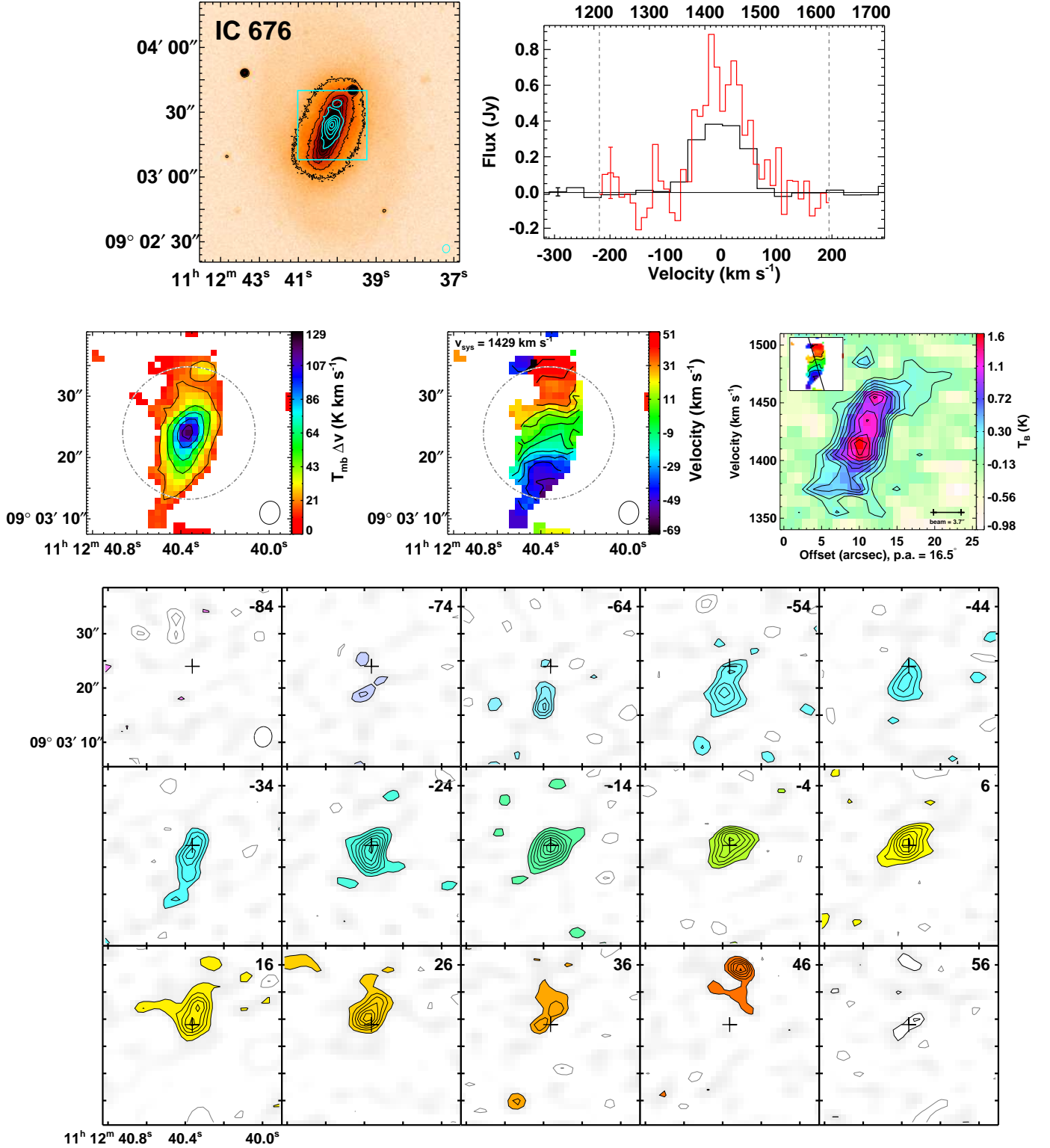


Figure A1. IC 676 is a field regular rotator ($M_K = -22.27$) with a bar and ring stellar morphology. It has a dust filament. The moment0 peak is 17 Jy beam⁻¹ km s⁻¹. The moment1 contours are placed at 10 km s⁻¹ intervals and the PVD contours are placed at 1.5σ intervals.

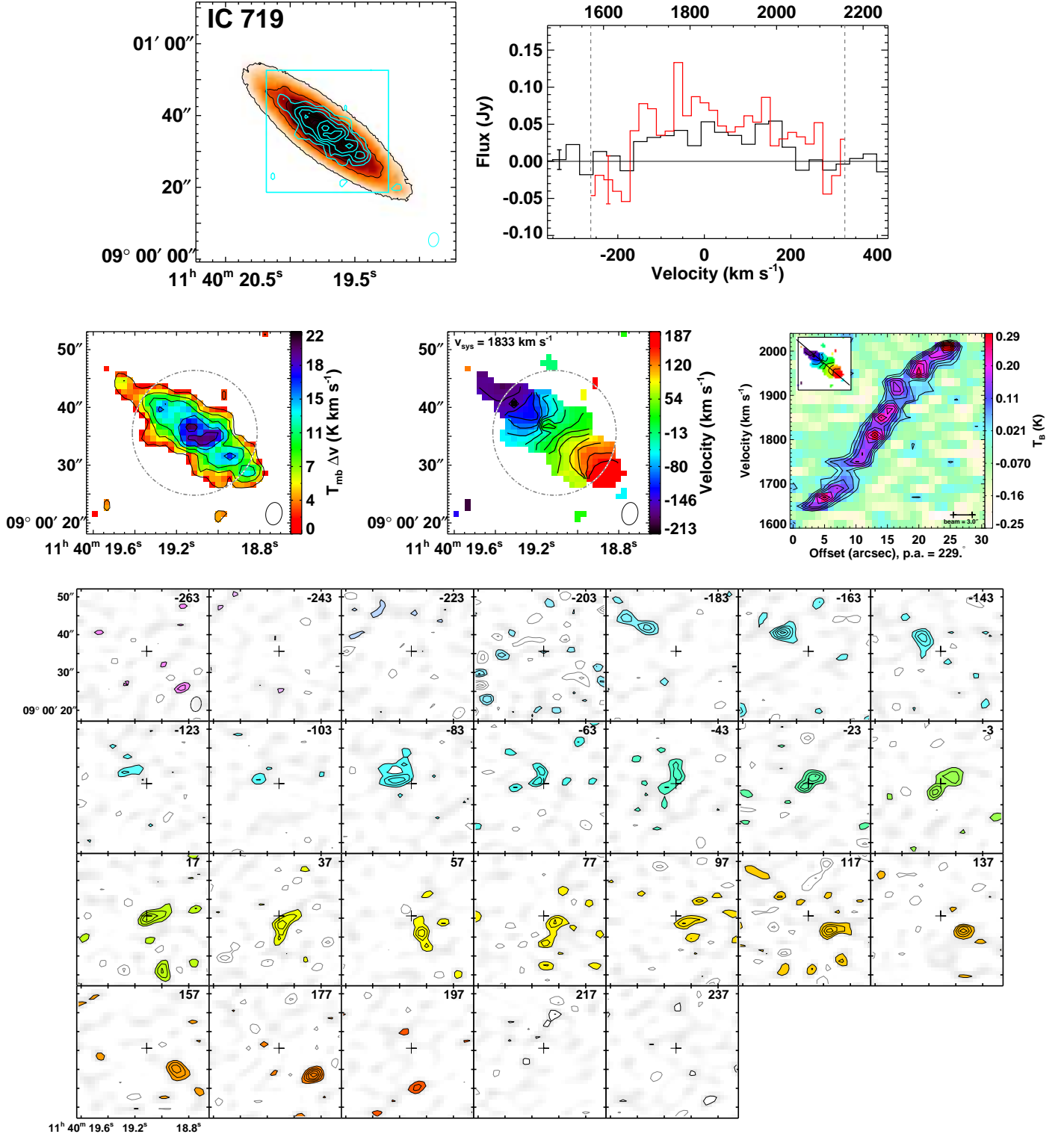


Figure A2. IC 719 is a field 2σ non-regular rotator ($M_K = -22.70$) with normal stellar morphology. It contains a dusty disc. The 2σ peak is the signature of two counter-rotating stellar discs with opposite angular momenta. The molecular gas is co-rotating with a kinematically decoupled core, and counter-rotating with respect to the dominant stellar component. The moment0 peak is $2.6 \text{ Jy beam}^{-1} \text{ km s}^{-1}$. The moment1 contours are placed at 25 km s^{-1} intervals.

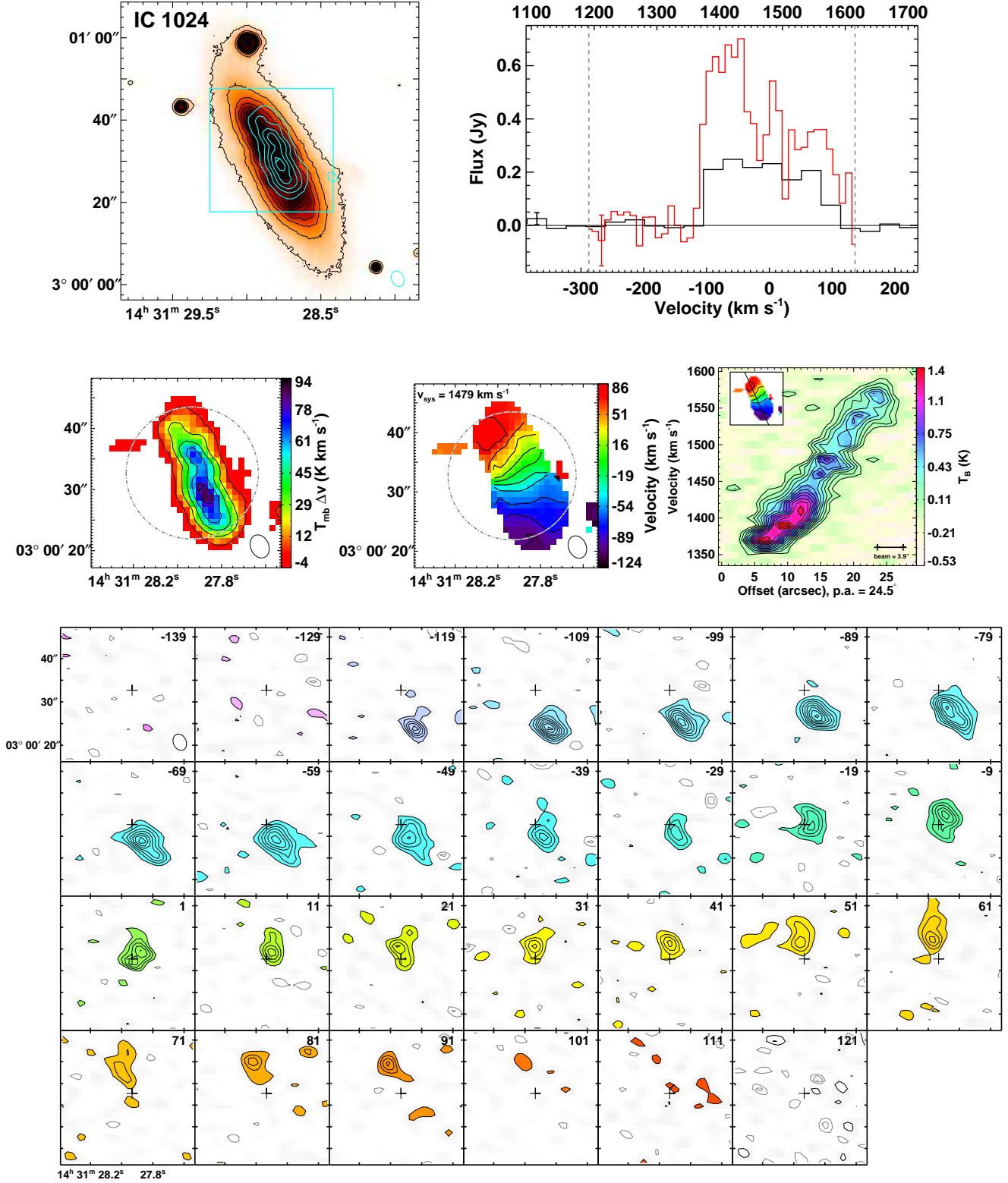


Figure A3. IC 1024 is a field regular rotator ($M_K = -21.85$) with stellar morphology that shows interaction features as well as a dust filament. The moment 0 peak is 14 Jy beam⁻¹ km s⁻¹. The channel map and PVD contours are placed at 1.5 σ intervals.

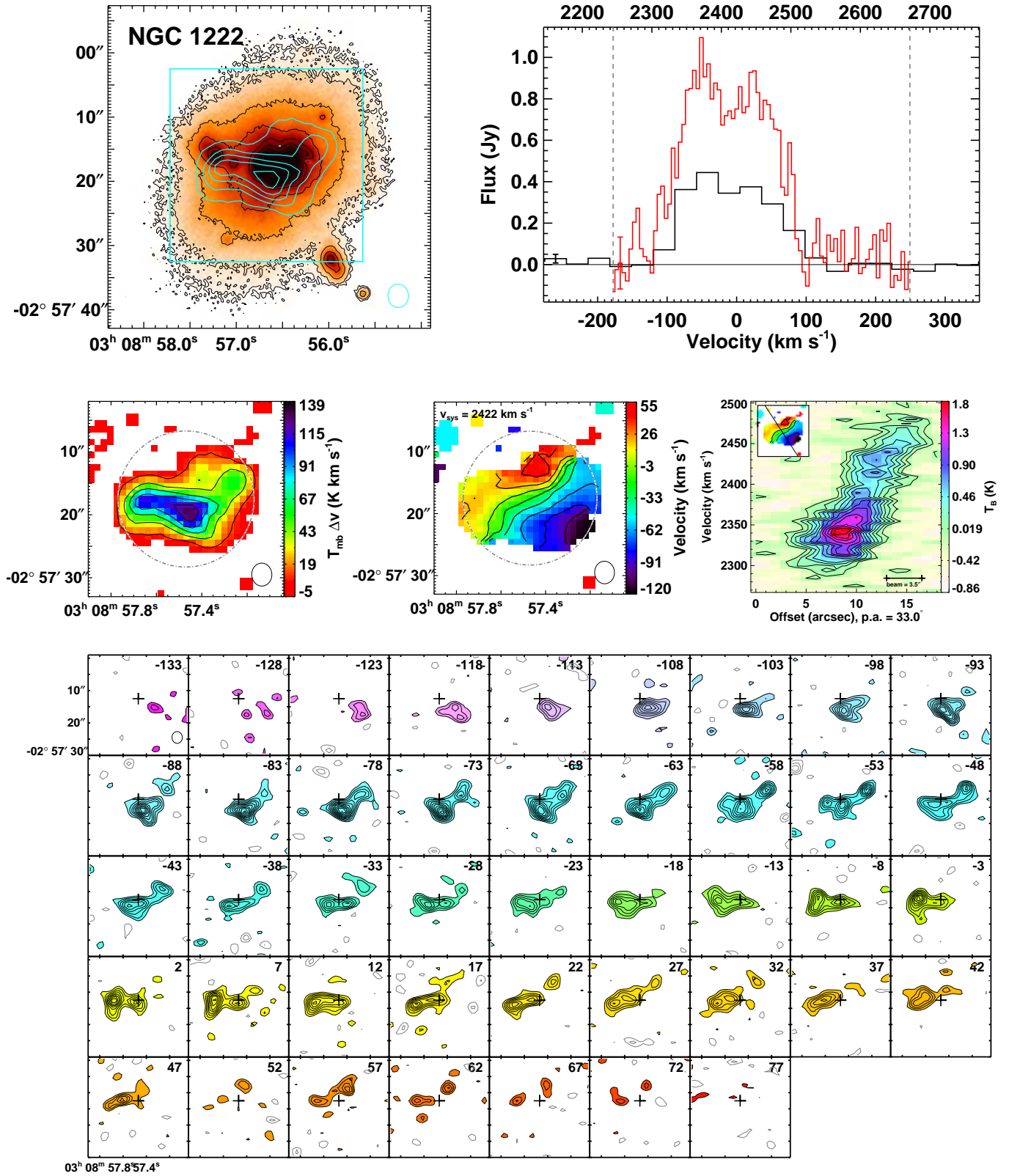


Figure A4. NGC 1222 is a field non-regular rotator ($M_K = -22.71$) with stellar morphology that shows interaction features as well as dust filaments. It is a well-known interaction, and cross-identified as Markarian 603 (Beck et al. 2007). The moment0 peak is $18 \text{ Jy beam}^{-1} \text{ km s}^{-1}$. The PVD contours are placed at 1.5σ intervals.

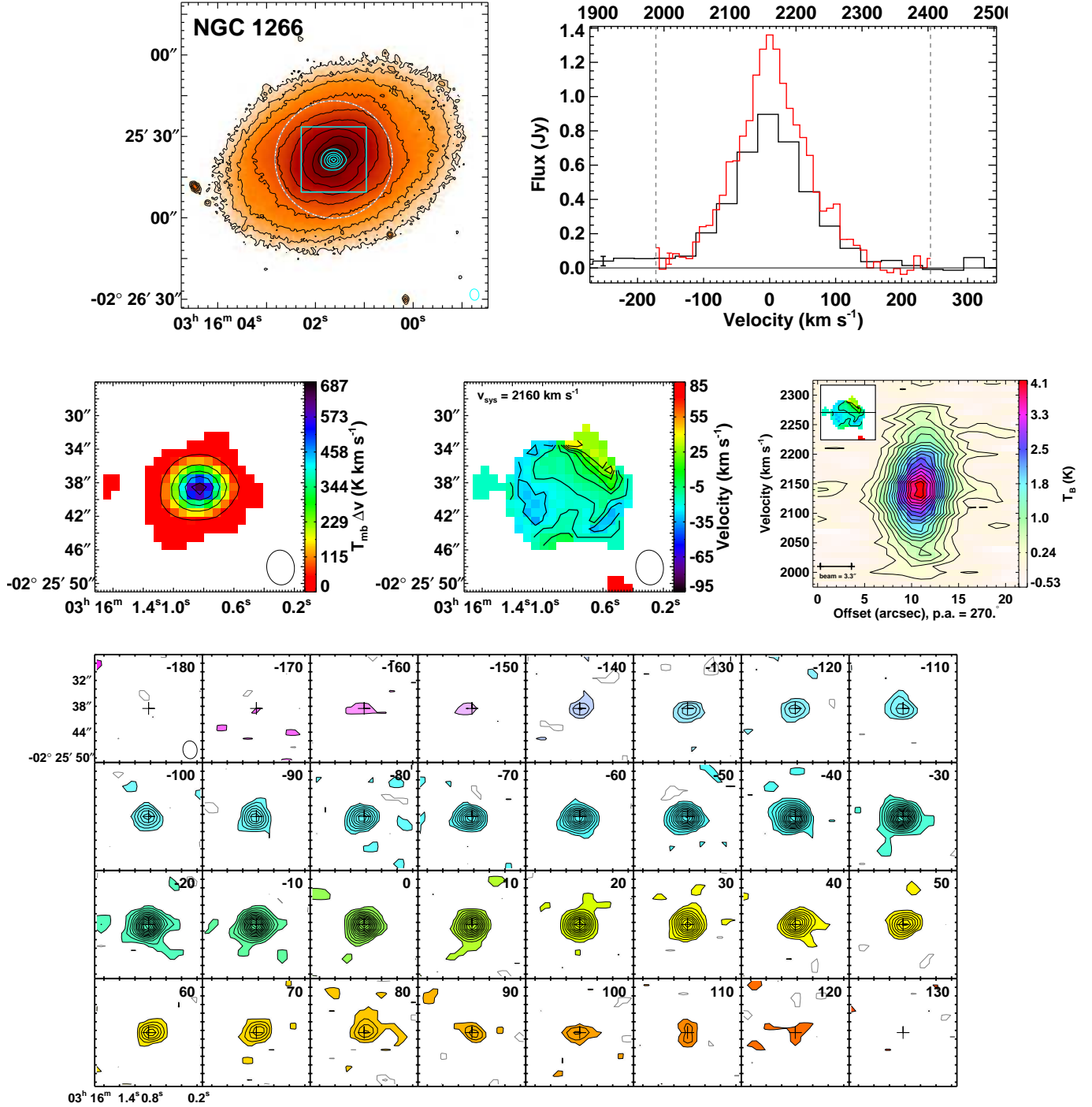


Figure A5. NGC 1266 is a field regular rotator ($M_K = -22.93$) with normal stellar morphology. It is also observed to have a dust filament. Not only was it the brightest detection in the sample, but it had the largest linewidths observed. It was initially unresolved in CARMA D-array, thus was observed in the much higher resolution arrays. NGC 1266 hosts a massive molecular outflow that appears to be driven by an AGN. Further details can be found in Alatalo et al. 2011. The moment0 peak is 100 Jy beam⁻¹. The moment1 contours are placed at 10 km s⁻¹ intervals. The channel map contours are placed at 2σ intervals and the PVD contours are placed at 3σ intervals.

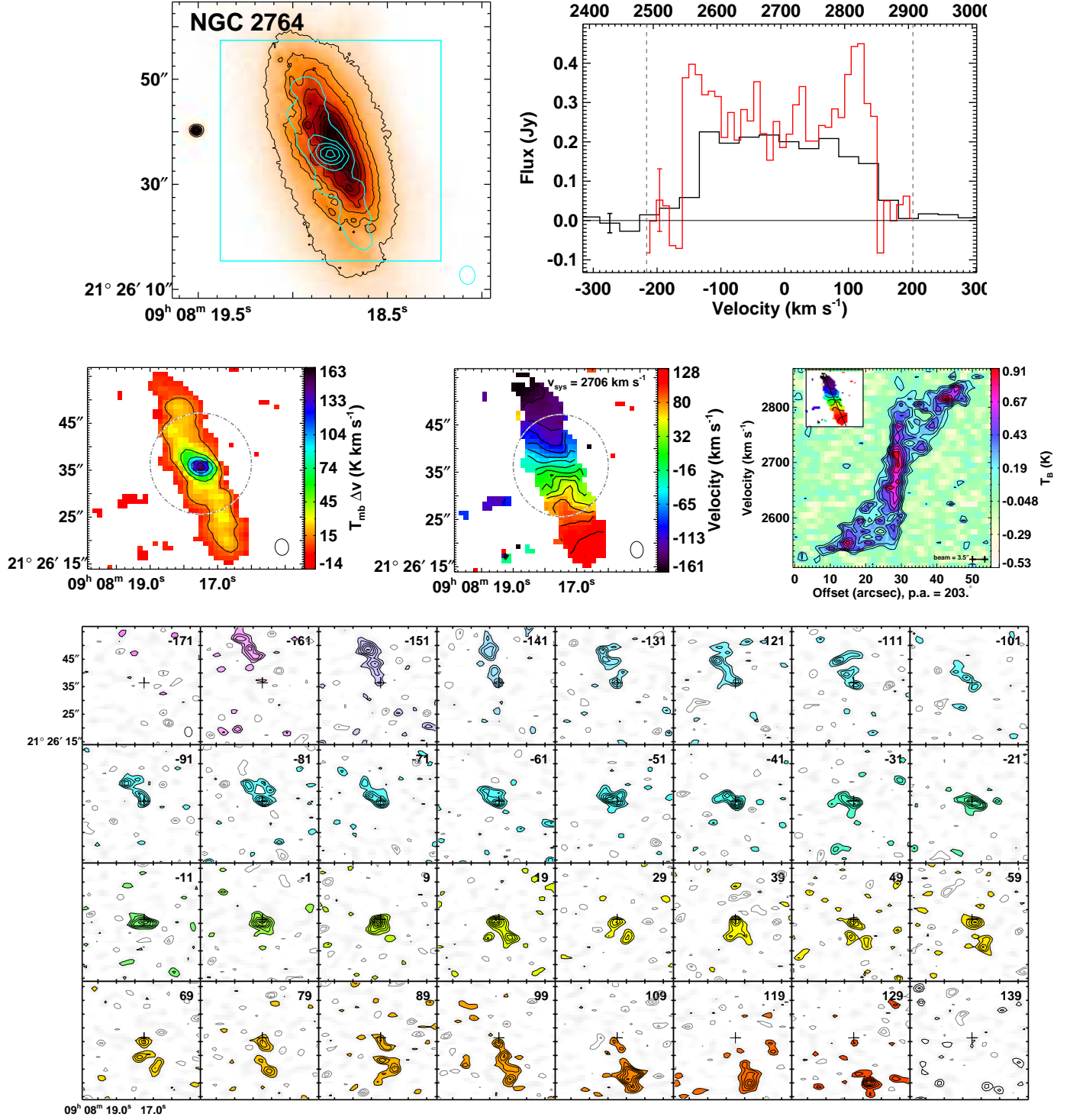


Figure A6. NGC 2764 is a field regular rotator ($M_K = -23.19$) with stellar morphology that indicates interaction. It is also observed to contain a blue nucleus and dust filaments. The moment0 peak is $18 \text{ Jy beam}^{-1} \text{ km s}^{-1}$. The PVD contours are placed at 1.5σ intervals.

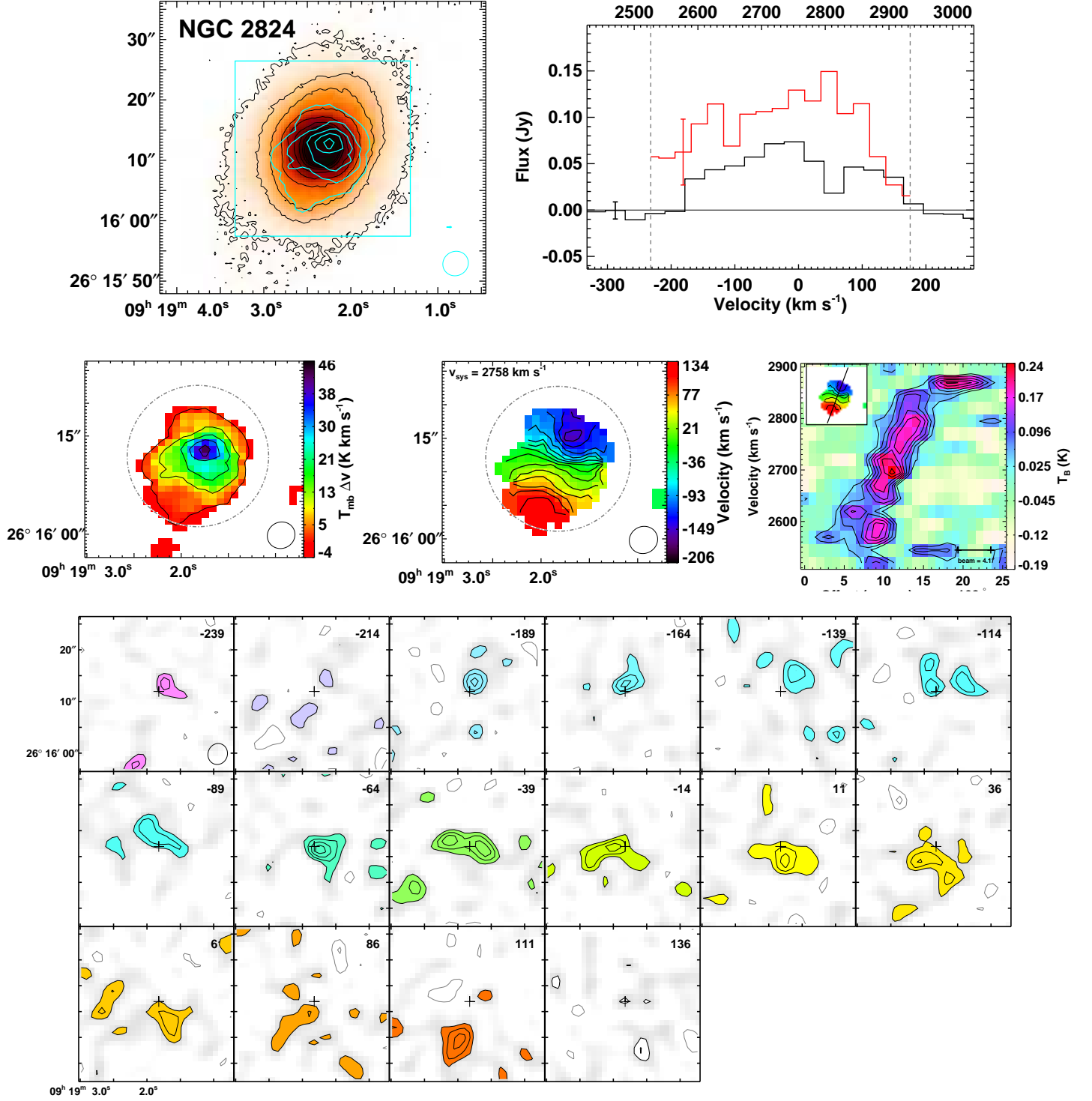


Figure A7. NGC 2824 is a field regular rotator ($M_K = -22.93$) with a ring stellar morphology. It contains a dust disc. The moment0 peak is $8.6 \text{ Jy beam}^{-1} \text{ km s}^{-1}$.

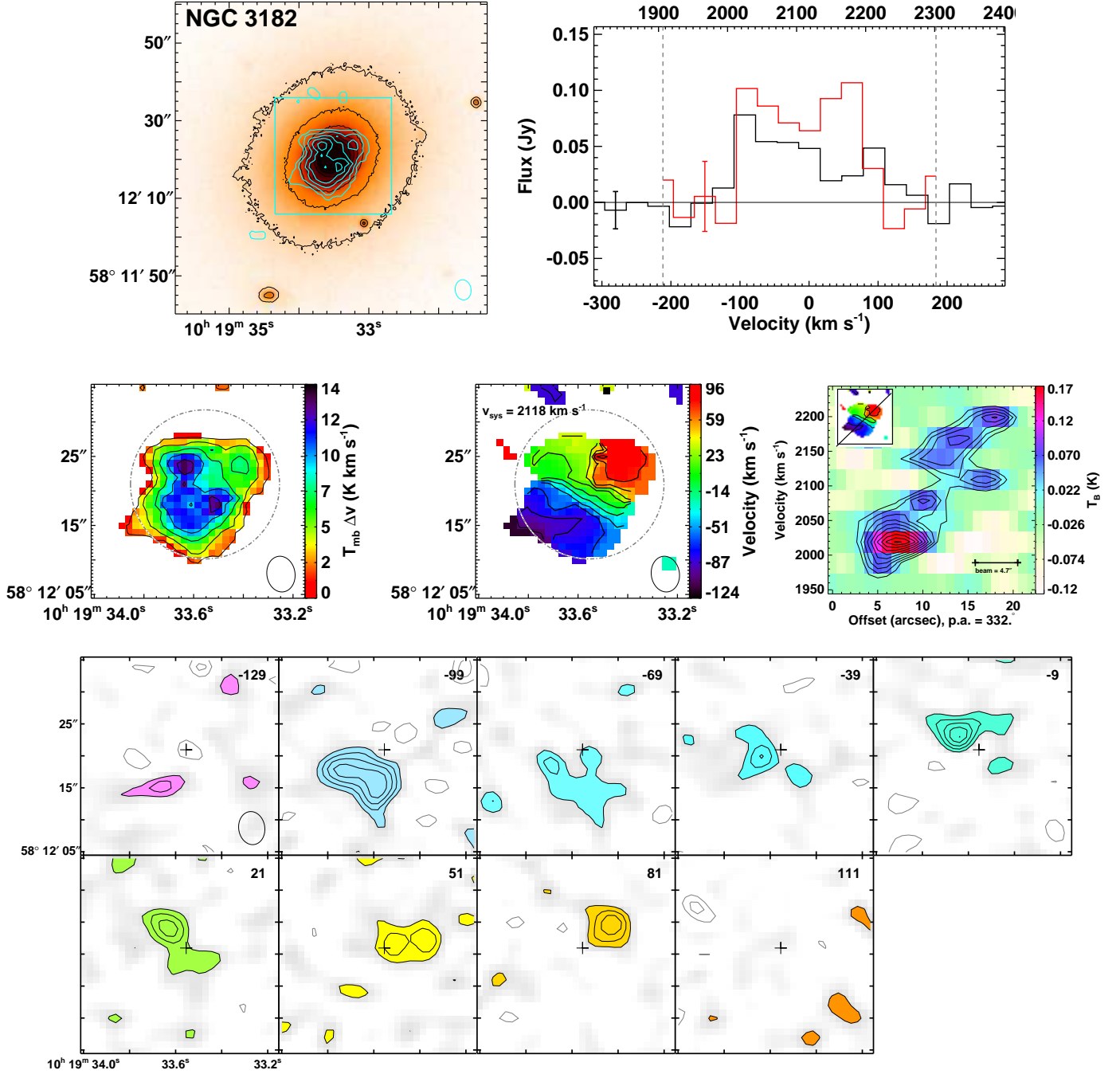


Figure A8. NGC 3182 is a field regular rotator ($M_K = -23.19$) with normal stellar morphology and contains a dust bar and ring. It is one of the faintest detections within the sample, thus it is likely much of the CO emission in this system is below the noise in the channel maps. The moment0 peak is $3.3 \text{ Jy beam}^{-1} \text{ km s}^{-1}$.

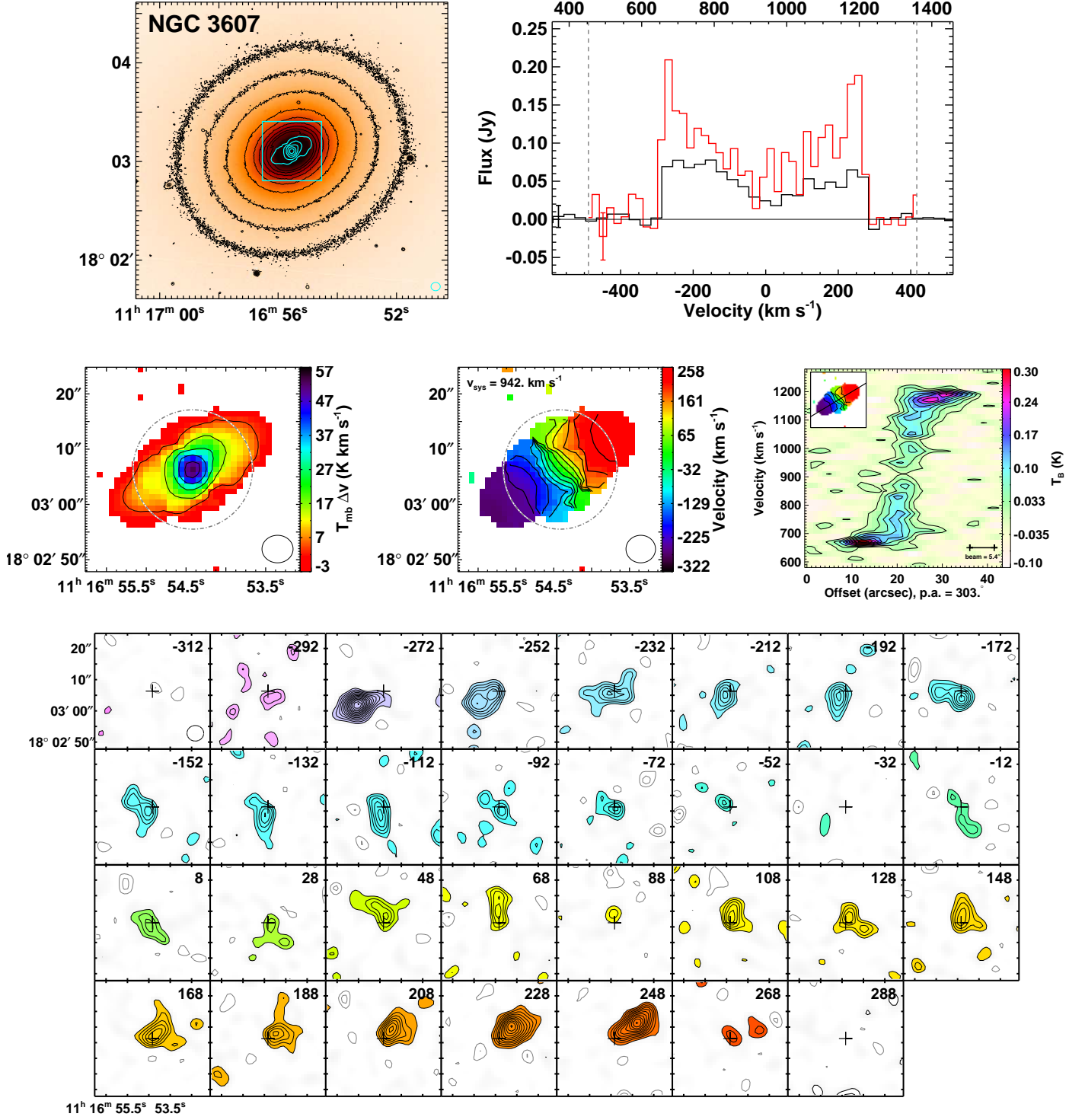


Figure A9. NGC 3607 is a field regular rotator ($M_K = -24.74$) with normal stellar morphology. It contains a dust disc. The moment0 peak is $17 \text{ Jy beam}^{-1} \text{ km s}^{-1}$. The moment1 contours are placed at 40 km s^{-1} intervals and the PVD contours are placed at 3σ intervals.

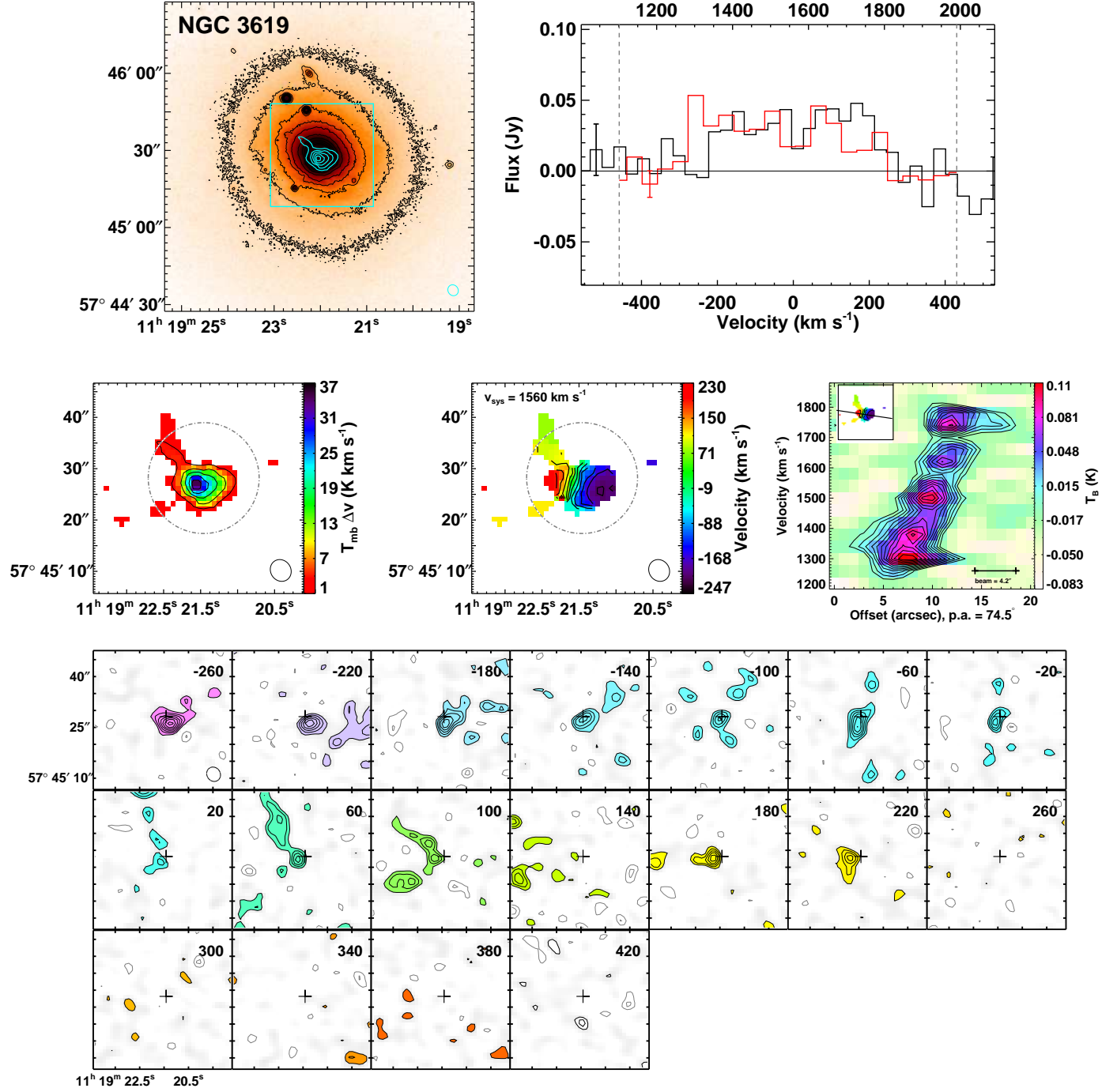


Figure A10. NGC 3619 is a field regular rotator ($M_K = -23.57$) with a shell stellar morphology. It contains dust filaments, bars and rings. It is very likely that CARMA has resolved out what is possibly an extended gas disc. Observations that are sensitive to larger size scales is required to confirm this. The moment0 peak is $6.9 \text{ Jy beam}^{-1} \text{ km s}^{-1}$. The moment1 contours are placed at 40 km s^{-1} intervals.

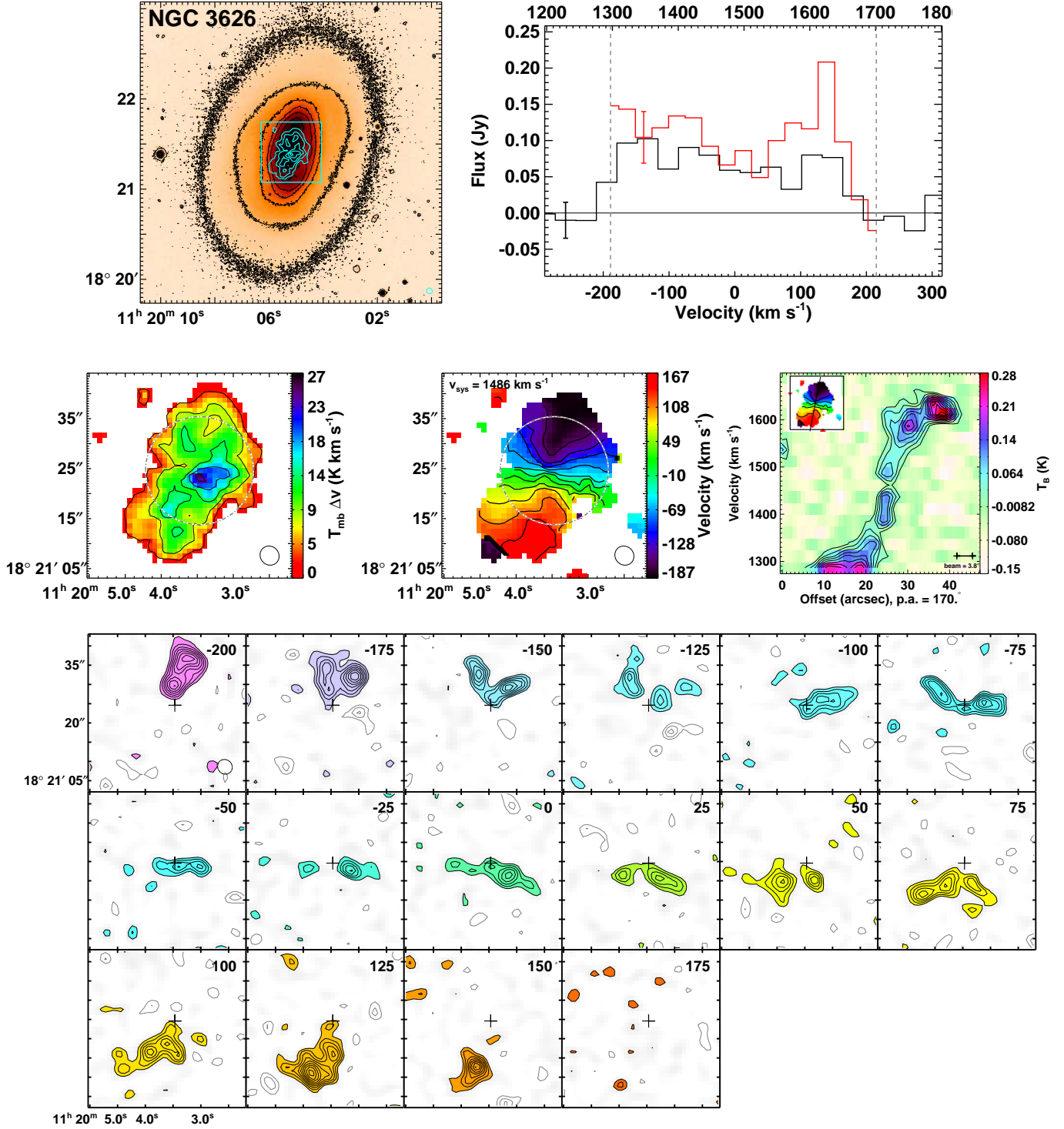


Figure A11. NGC 3626 is a group regular rotator ($M_K = -23.30$) that includes a double maximum velocity feature, with ring stellar morphology. It contains a dust disc. Unfortunately the central velocity of the observations were offset from v_{sys} , and due to its large linewidth, a small amount of the blueshifted spectrum was not within the 420 km s⁻¹ CARMA window. The moment0 peak is 4.3 Jy beam⁻¹ km s⁻¹. The moment1 contours are placed at 30 km s⁻¹ intervals and PVD contours are placed at 1.5 σ intervals.

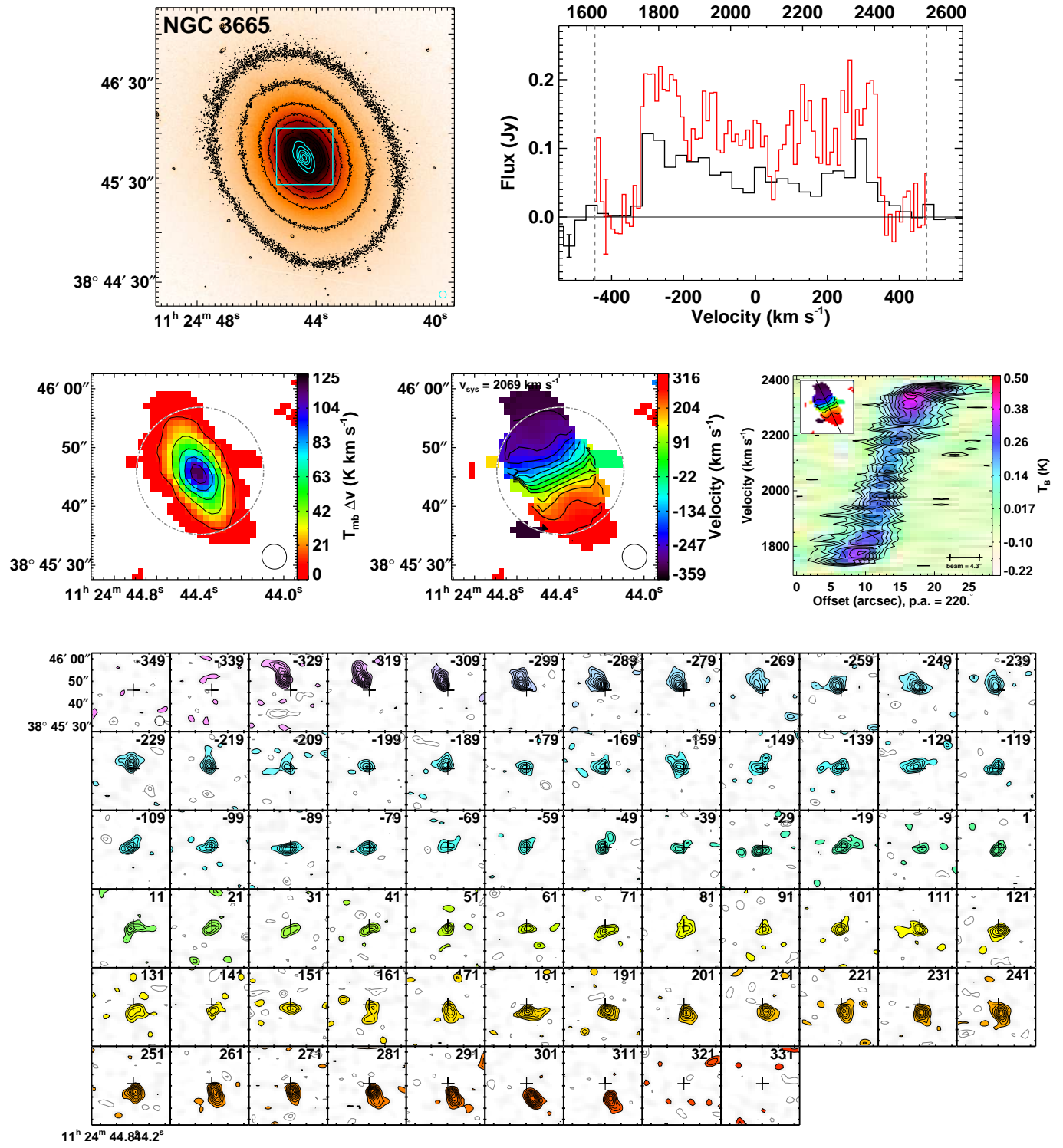


Figure A12. NGC 3665 is a group regular rotator ($M_K = -24.92$) with normal stellar morphology. It contains a dust disc. The moment0 peak is 24 Jy beam⁻¹ km s⁻¹. The moment1 contours are placed at 50 km s⁻¹ intervals and the PVD contours are placed at 2σ intervals.

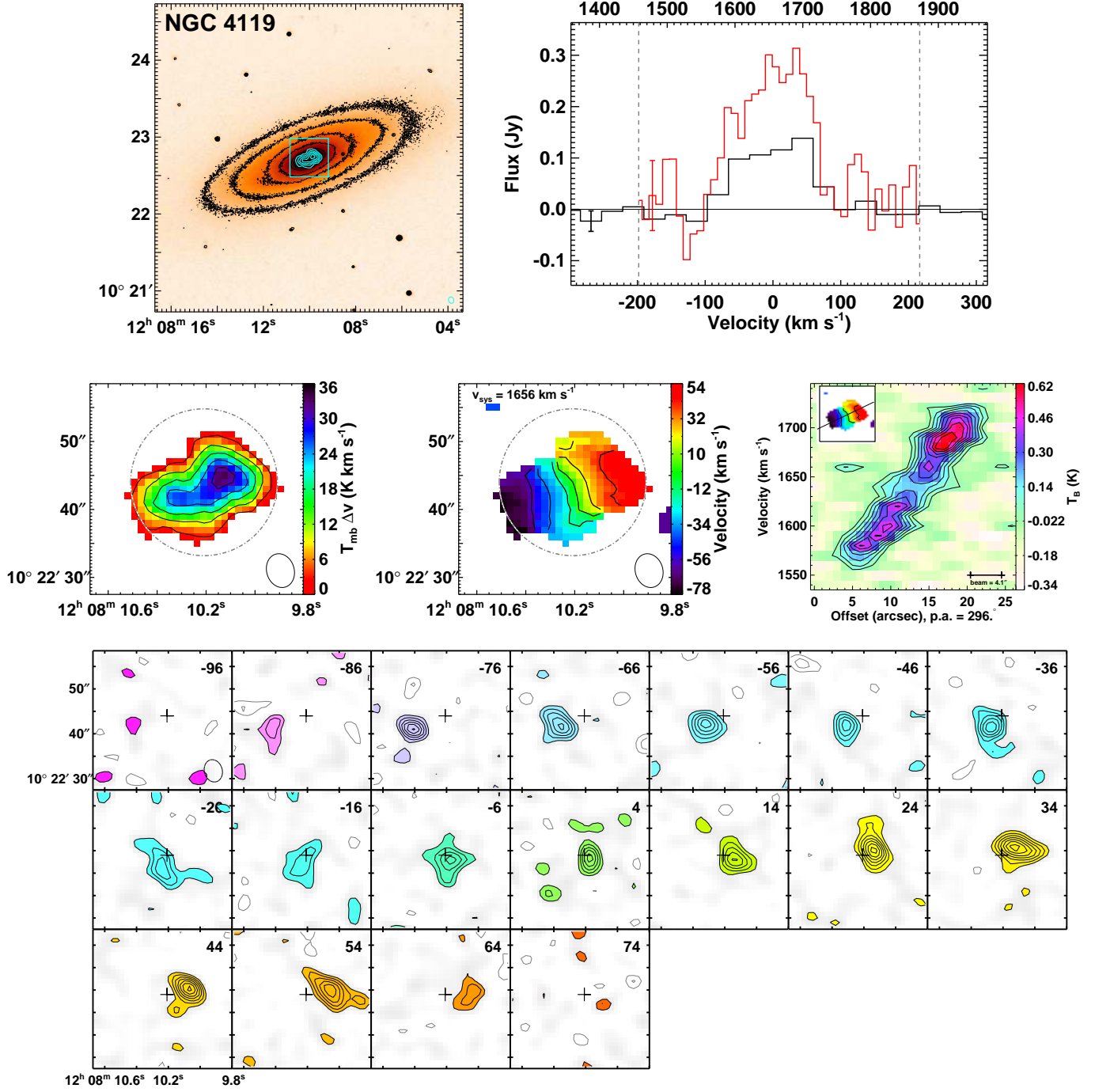


Figure A13. NGC 4119 is a Virgo regular rotator ($M_K = -22.60$) with normal stellar morphology. It contains a dust disc. The moment0 peak is $8.1 \text{ Jy beam}^{-1} \text{ km s}^{-1}$. The PVD contours are placed at 1.5σ intervals.

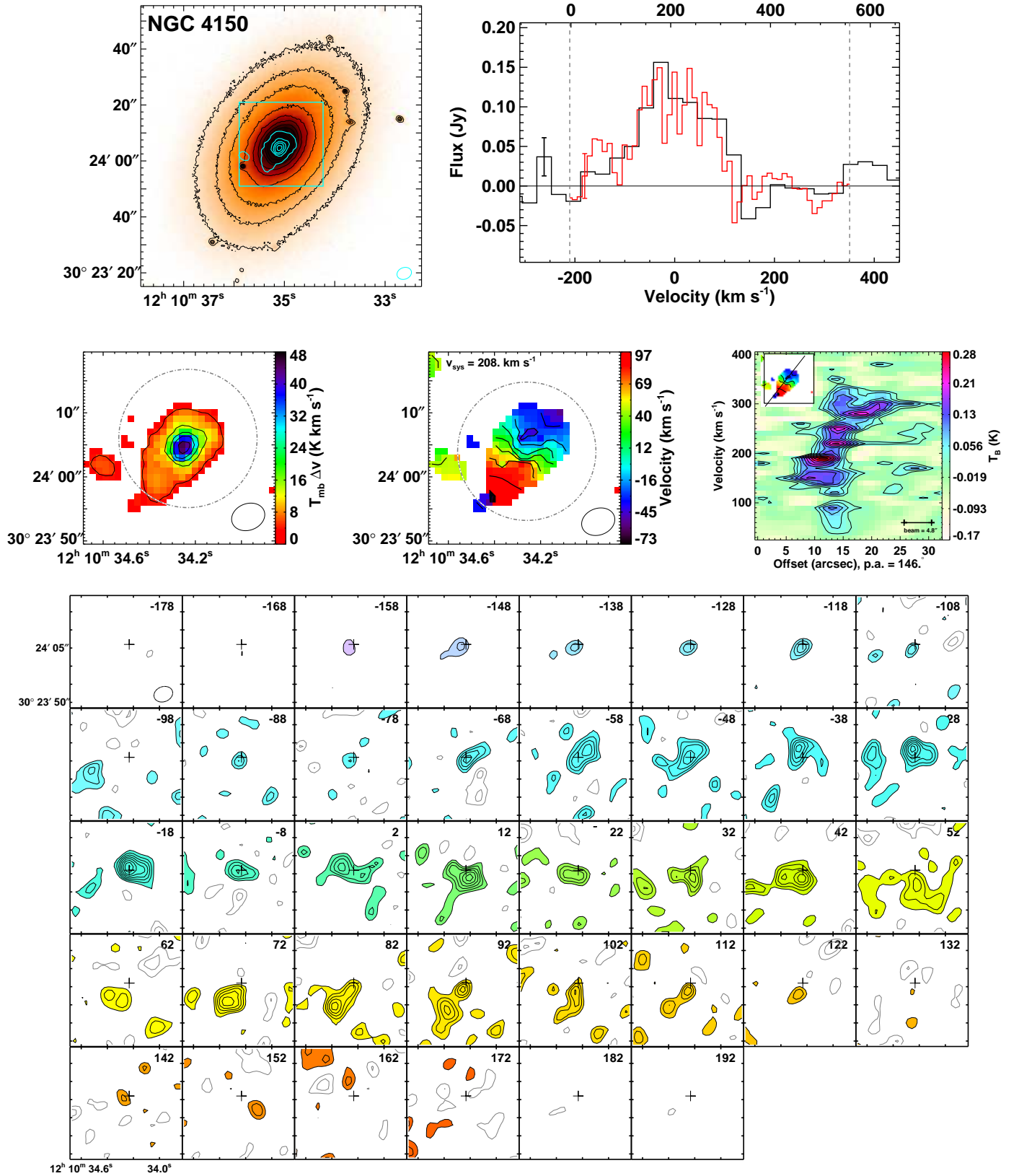


Figure A14. NGC 4150 is a Virgo regular rotator ($M_K = -21.65$) with normal stellar morphology. The moment0 peak is $9.9 \text{ Jy beam}^{-1} \text{ km s}^{-1}$. The PVD contours are placed at 1.5σ intervals.

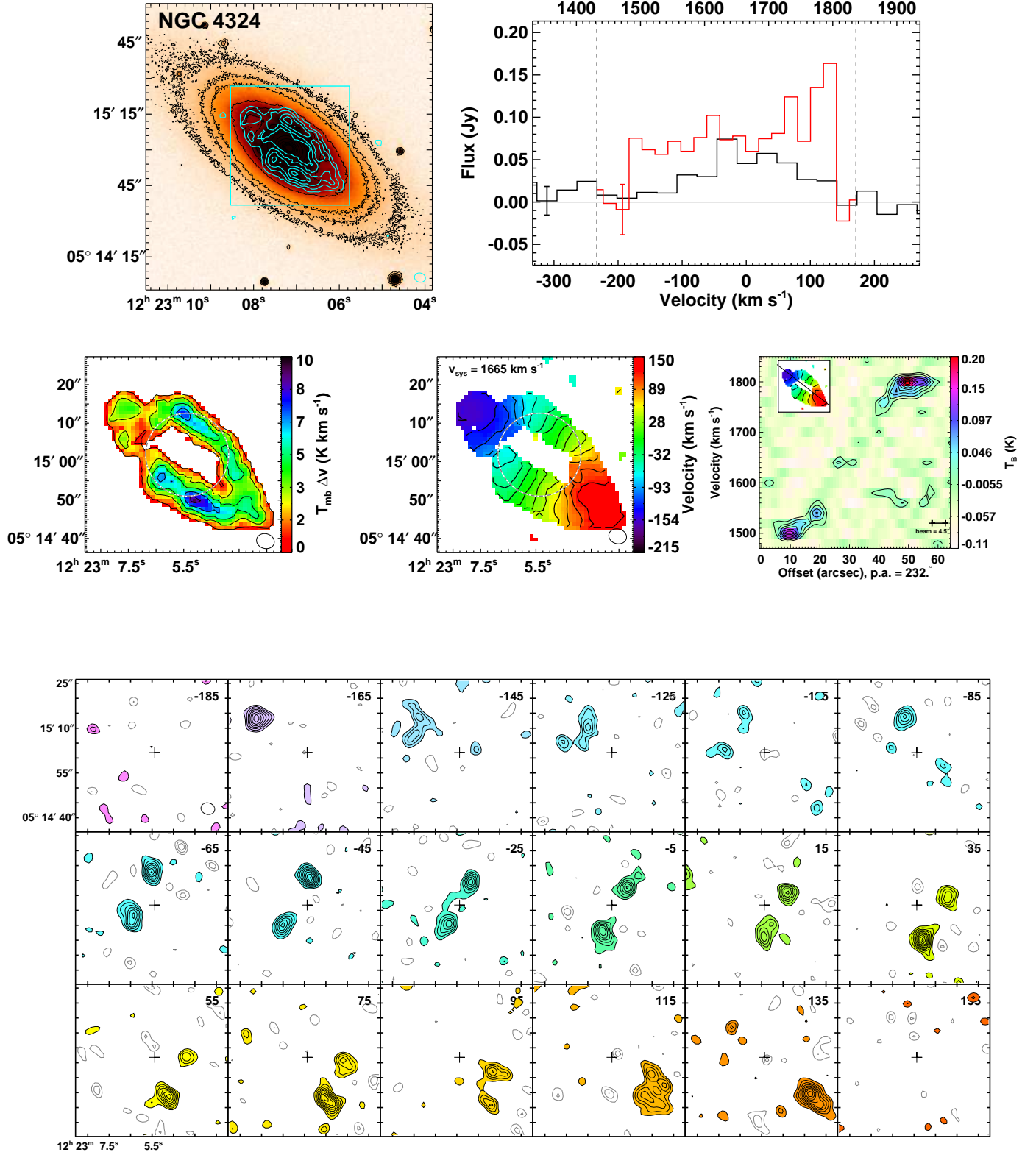


Figure A15. NGC 4324 is a field regular rotator ($M_K = -21.61$) that includes two velocity maxima. It contains a ring stellar morphology, as well as a dust disc, bar, and ring. The moment0 peak is $2.0 \text{ Jy beam}^{-1} \text{ km s}^{-1}$. The PVD contours are placed at 2σ intervals.

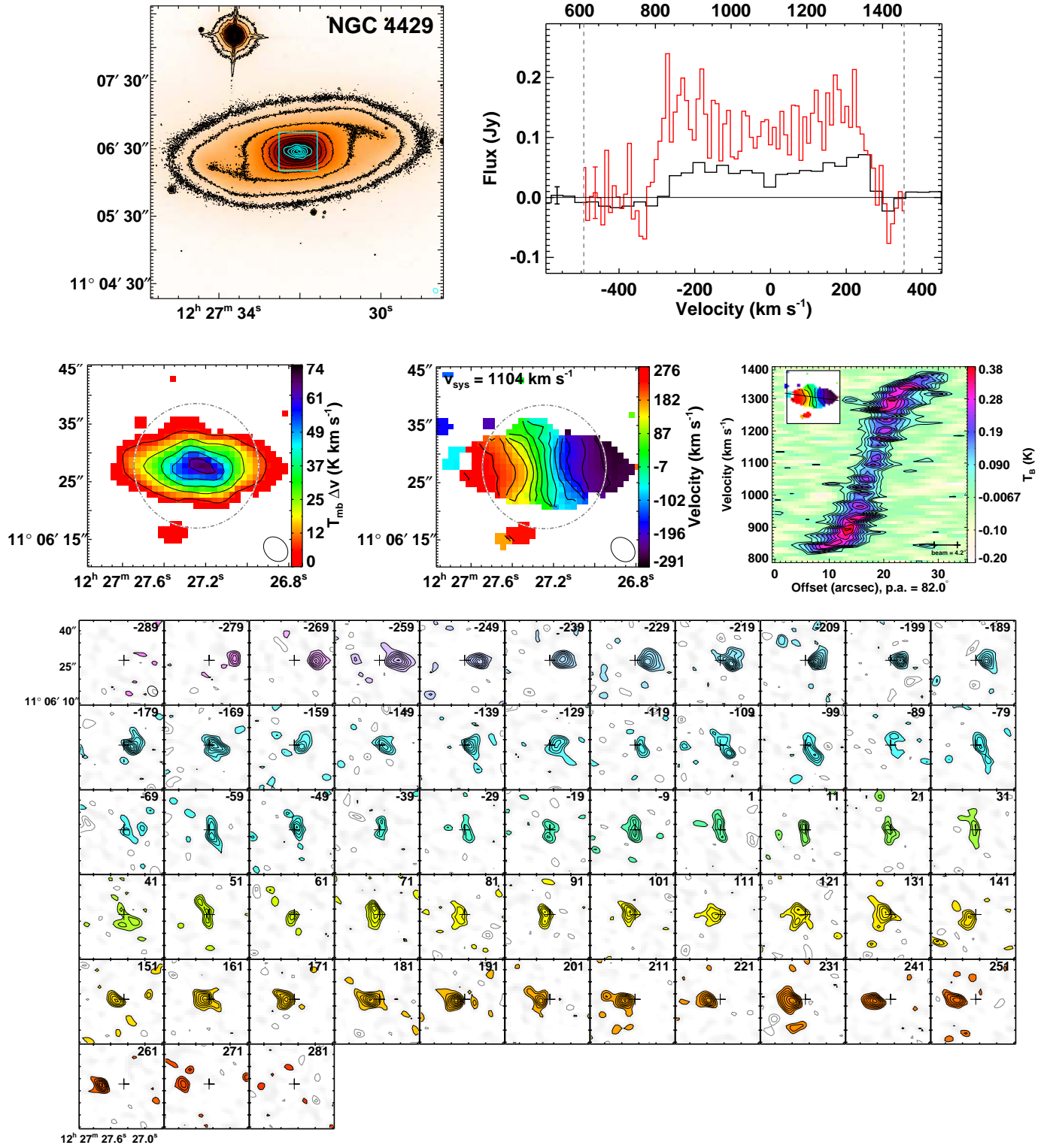


Figure A16. NGC 4429 is a Virgo regular rotator ($M_K = -24.32$) that includes two velocity maxima, with a bar and ring stellar morphology. It contains a dust disc. The moment0 peak is 14 Jy beam⁻¹ km s⁻¹. The moment1 contours are at 40 km s⁻¹ intervals and the PVD contours are placed at 1.5σ intervals.

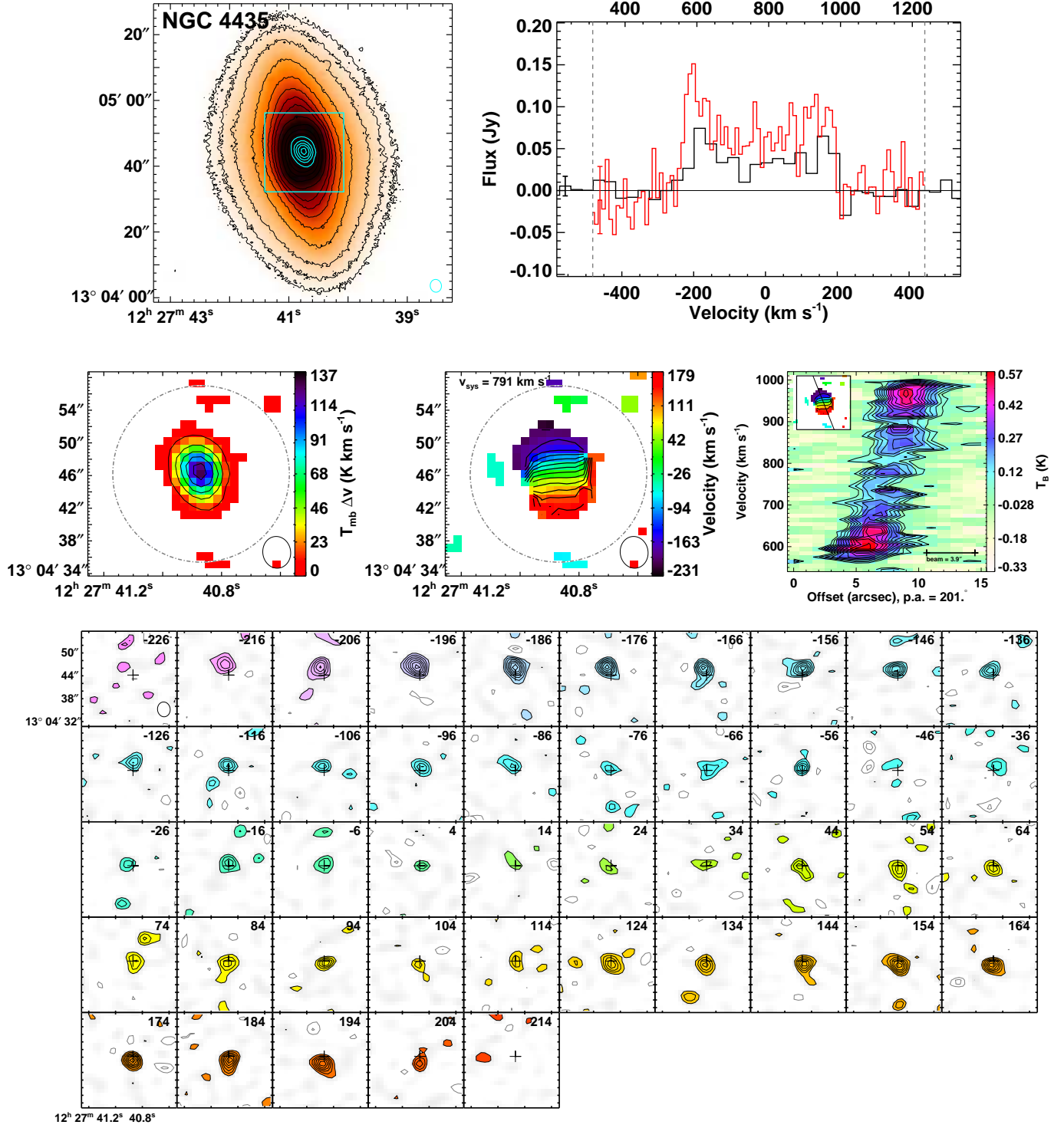


Figure A17. NGC 4435 is a Virgo regular rotator ($M_K = -23.82$) that includes two velocity maxima, with a normal stellar morphology. It contains a dust disc. The moment0 peak is 20 Jy beam⁻¹ km s⁻¹. The moment1 contours are at 30 km s⁻¹ intervals.

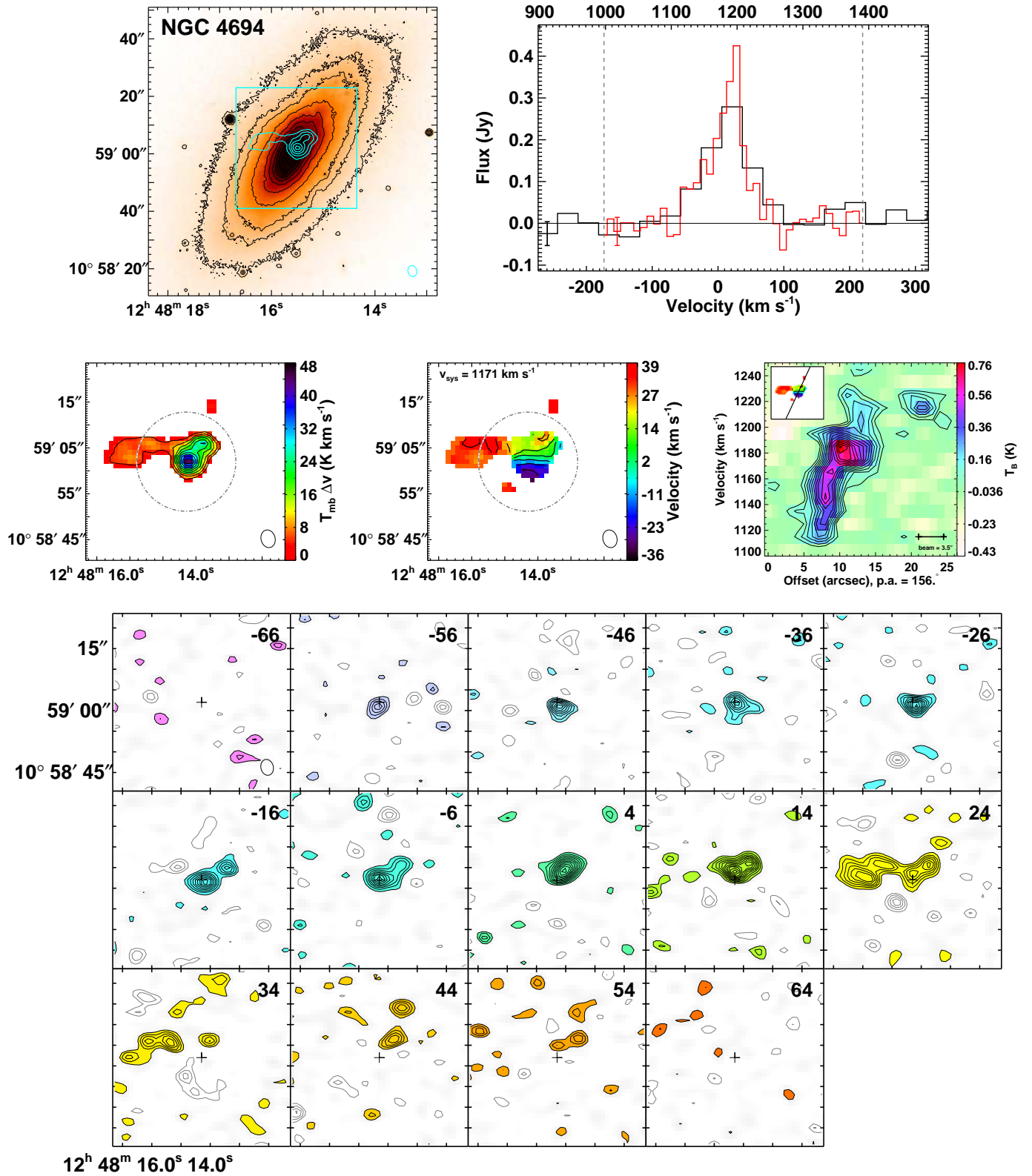


Figure A18. NGC 4694 is a Virgo regular rotator ($M_K = -22.15$) with normal stellar morphology. It appears to be on its first approach into Virgo. It contains a dust filaments and bars. The moment0 peak is $6.0 \text{ Jy beam}^{-1} \text{ km s}^{-1}$. The moment1 contours are placed at 10 km s^{-1} intervals and the PVD contours are placed at 1.5σ intervals.

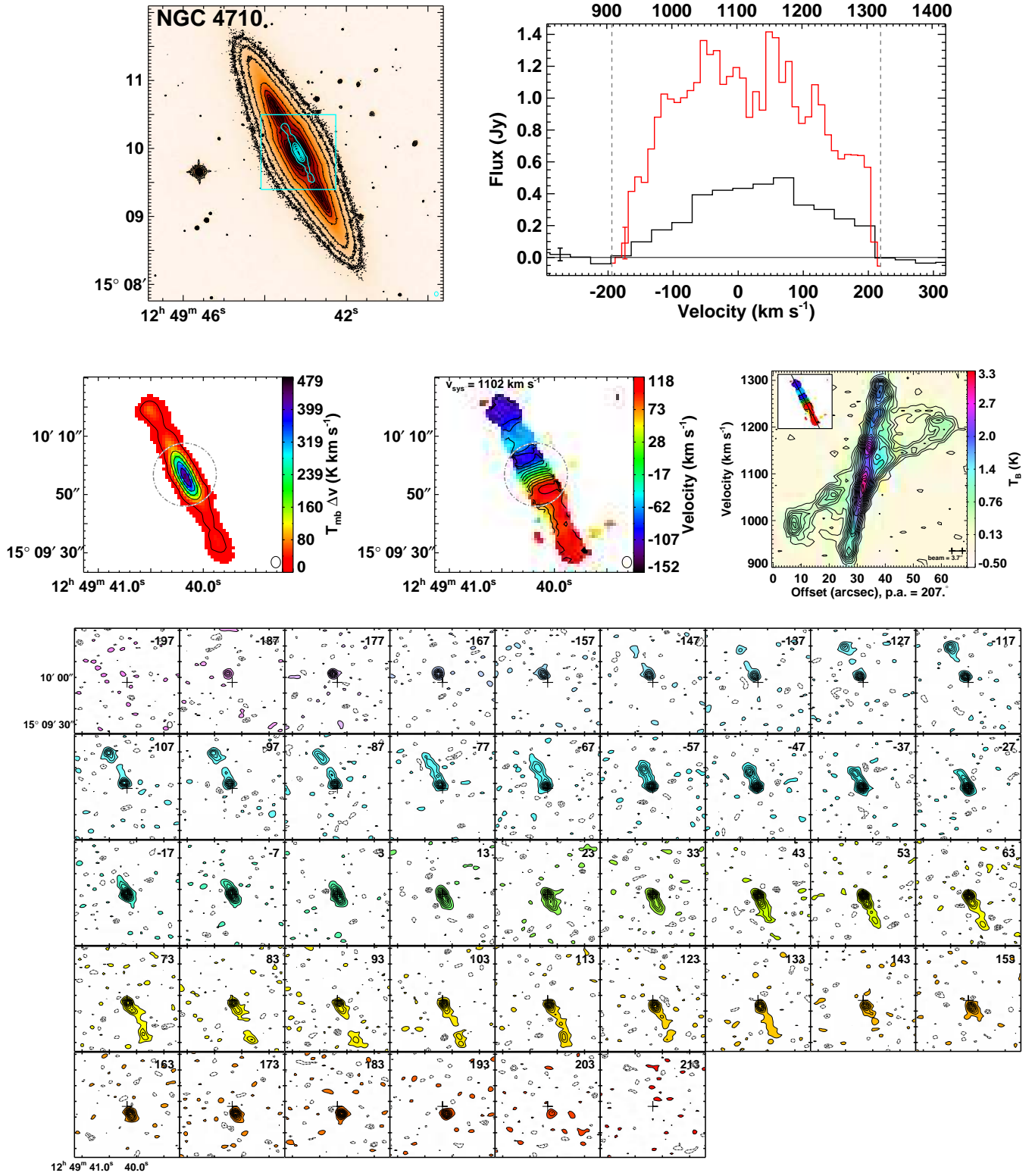


Figure A19. NGC 4710 is a Virgo regular rotator ($M_K = -23.52$) with normal stellar morphology. It appears to be on the outskirts of Virgo and is likely to be on its first approach. It contains a dust disc, and is one of the nearest to edge-on systems in the sample. The moment0 peak is $62 \text{ Jy beam}^{-1} \text{ km s}^{-1}$. Channel map and PVD contours are placed at 3σ intervals.

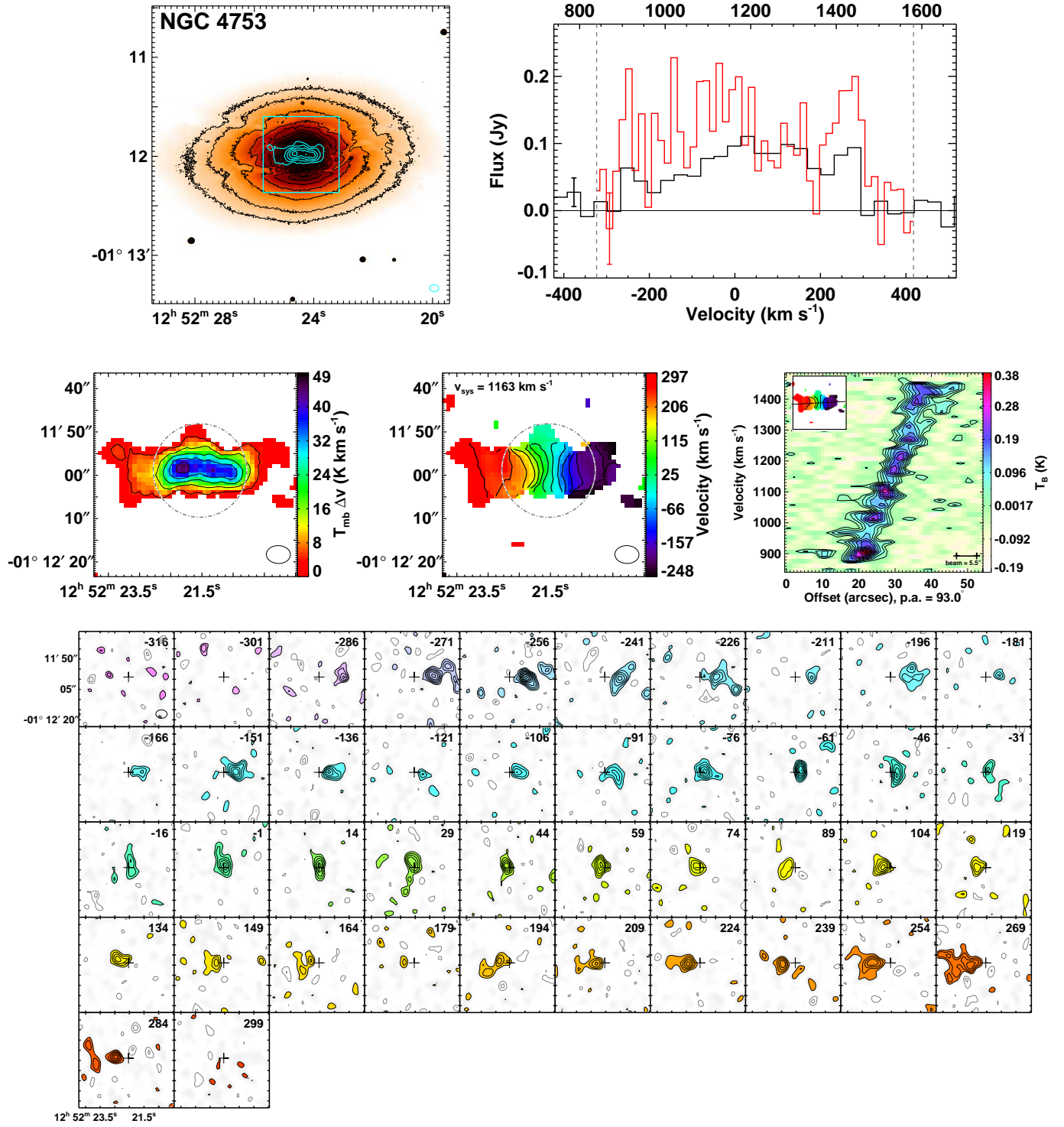


Figure A20. NGC 4753 is a field regular rotator ($M_K = -25.09$) that includes two velocity maxima, with stellar morphology consistent with interaction. It contains a dust filament. It is also the most massive galaxy in the CARMA ATLAS^{3D} survey. The moment0 peak is 12 Jy beam⁻¹ km s⁻¹. Moment1 contours are placed at 40 km s⁻¹ intervals and PVD contours are placed at 1.5 σ intervals.

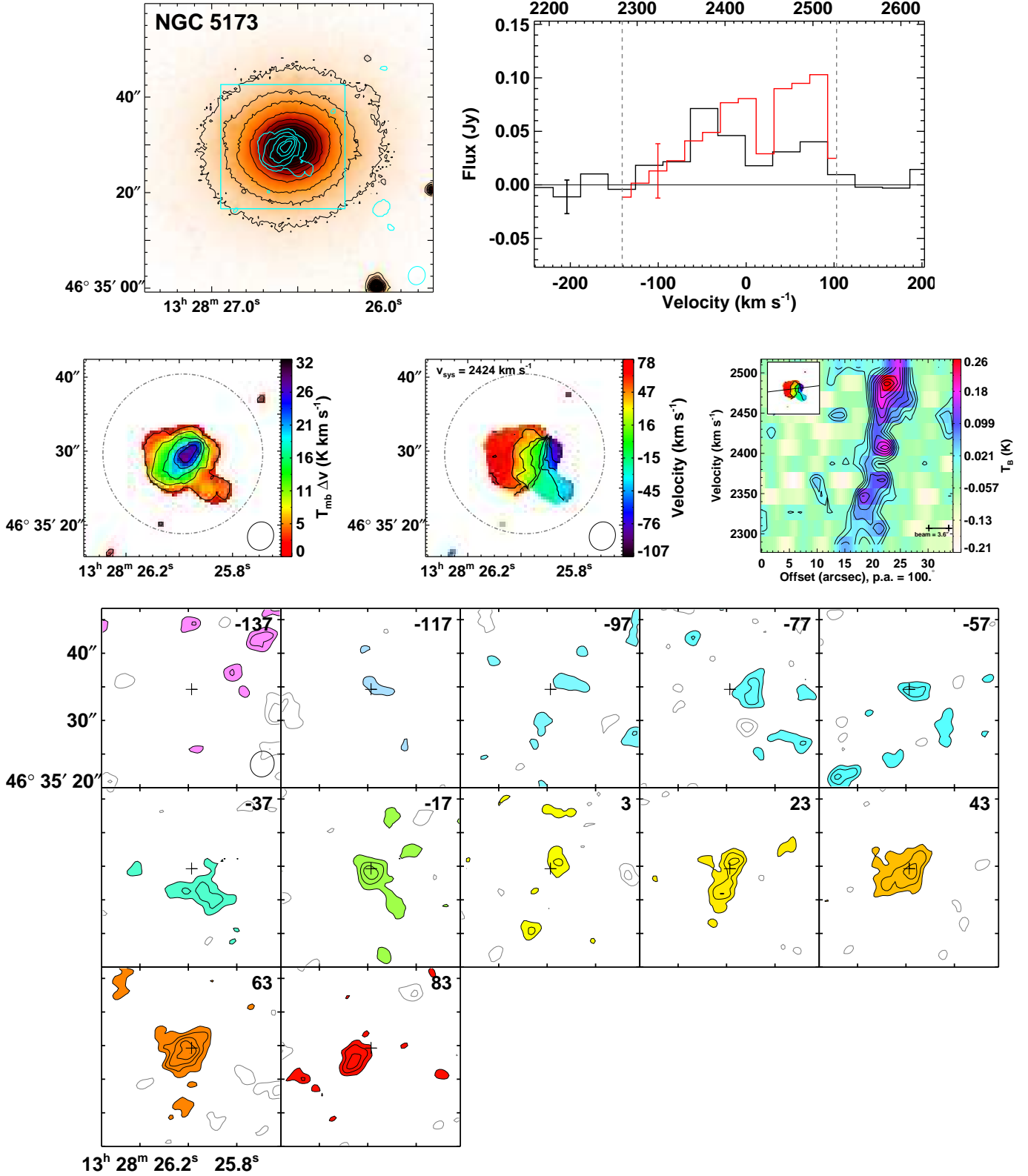


Figure A21. NGC 5173 is a group regular rotator ($M_K = -22.88$) with normal stellar morphology. It contains a dust bar. NGC 5173 was observed in CARMA D- and C- arrays, and the data were shared between this survey, and the work of Wei et al. 2010b, and thus uses the smaller pixel size of $0.4''$, to reflect the superior resolution of the observations. The moment0 peak is $4.6 \text{ Jy beam}^{-1} \text{ km s}^{-1}$. PVD contours are placed at 1.5σ intervals.

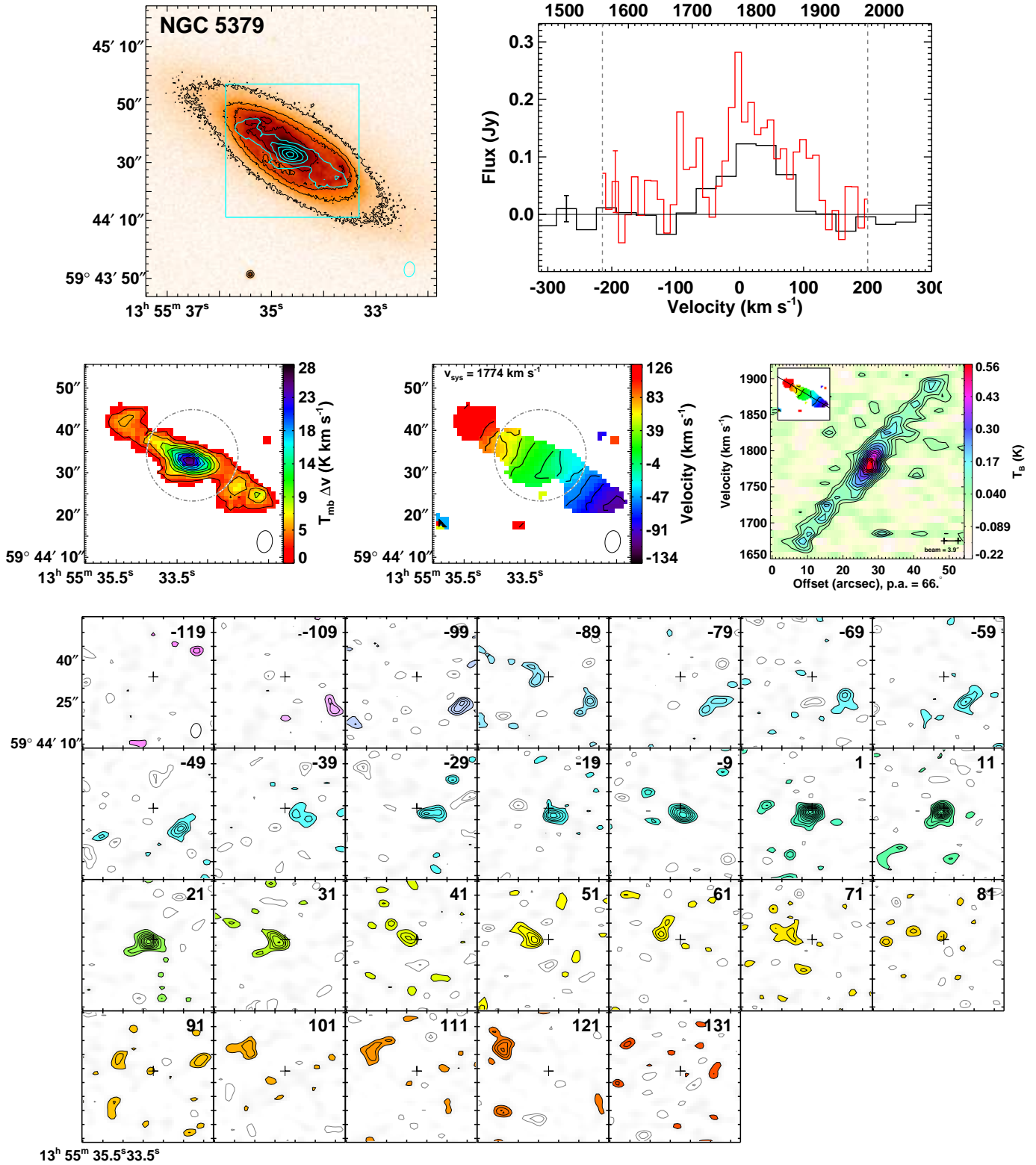


Figure A22. NGC 5379 is a group regular rotator ($M_K = -22.08$) with ring stellar morphology. It contains a dust bar, ring, and filaments. The moment0 peak is 5.7 Jy beam⁻¹ km s⁻¹. PVD contours are placed at 1.5 σ intervals.

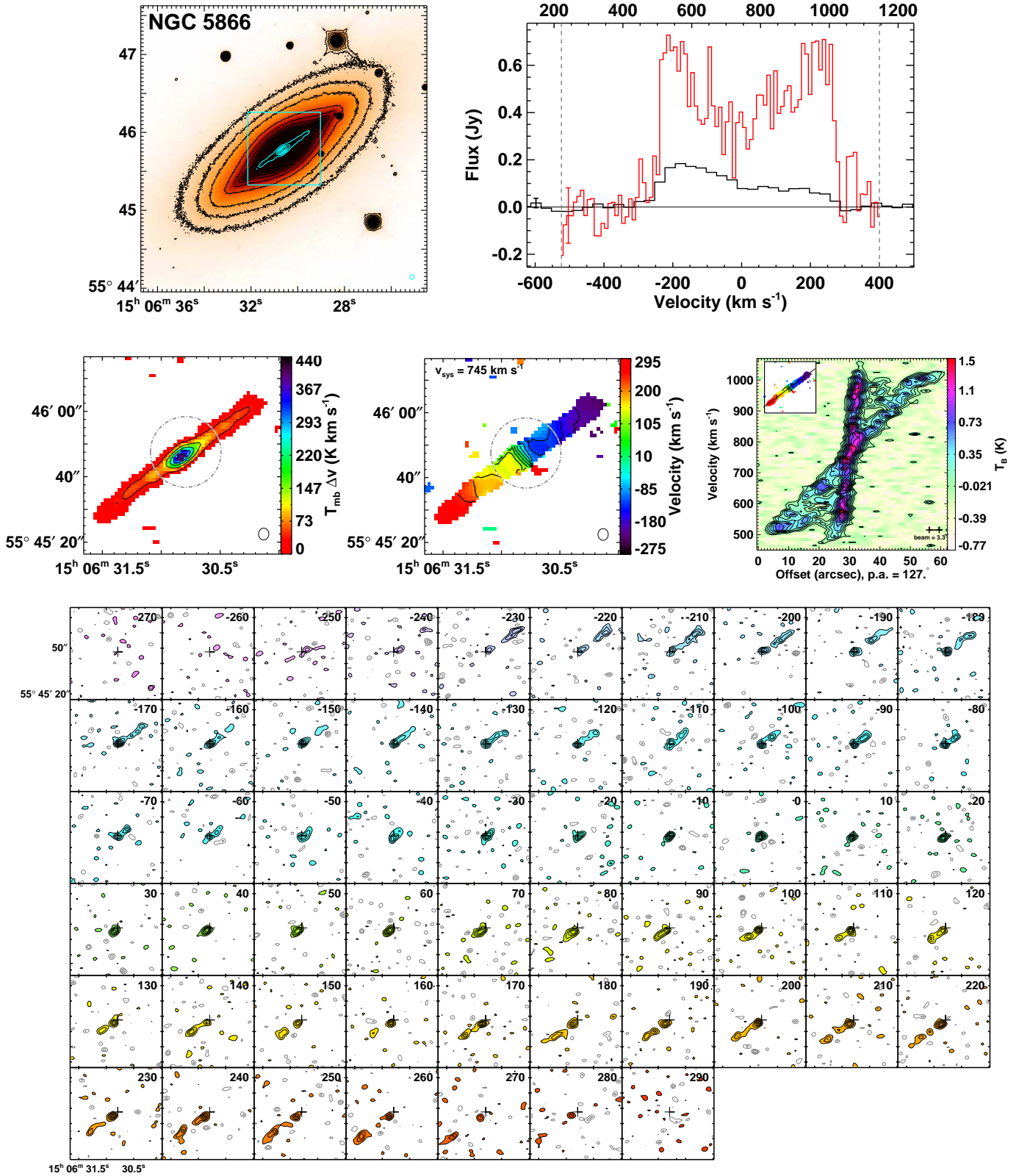


Figure A23. NGC 5866 is a field regular rotator ($M_K = -24.00$) with normal stellar morphology. It contains a dust disc. The molecular gas also strongly suggests that this galaxy contains a bar. The moment0 peak is $54 \text{ Jy beam}^{-1} \text{ km s}^{-1}$. Moment1 contours are placed at 40 km s^{-1} intervals. Channel map contours are placed at 2σ intervals and PVD contours are placed at 2σ intervals.

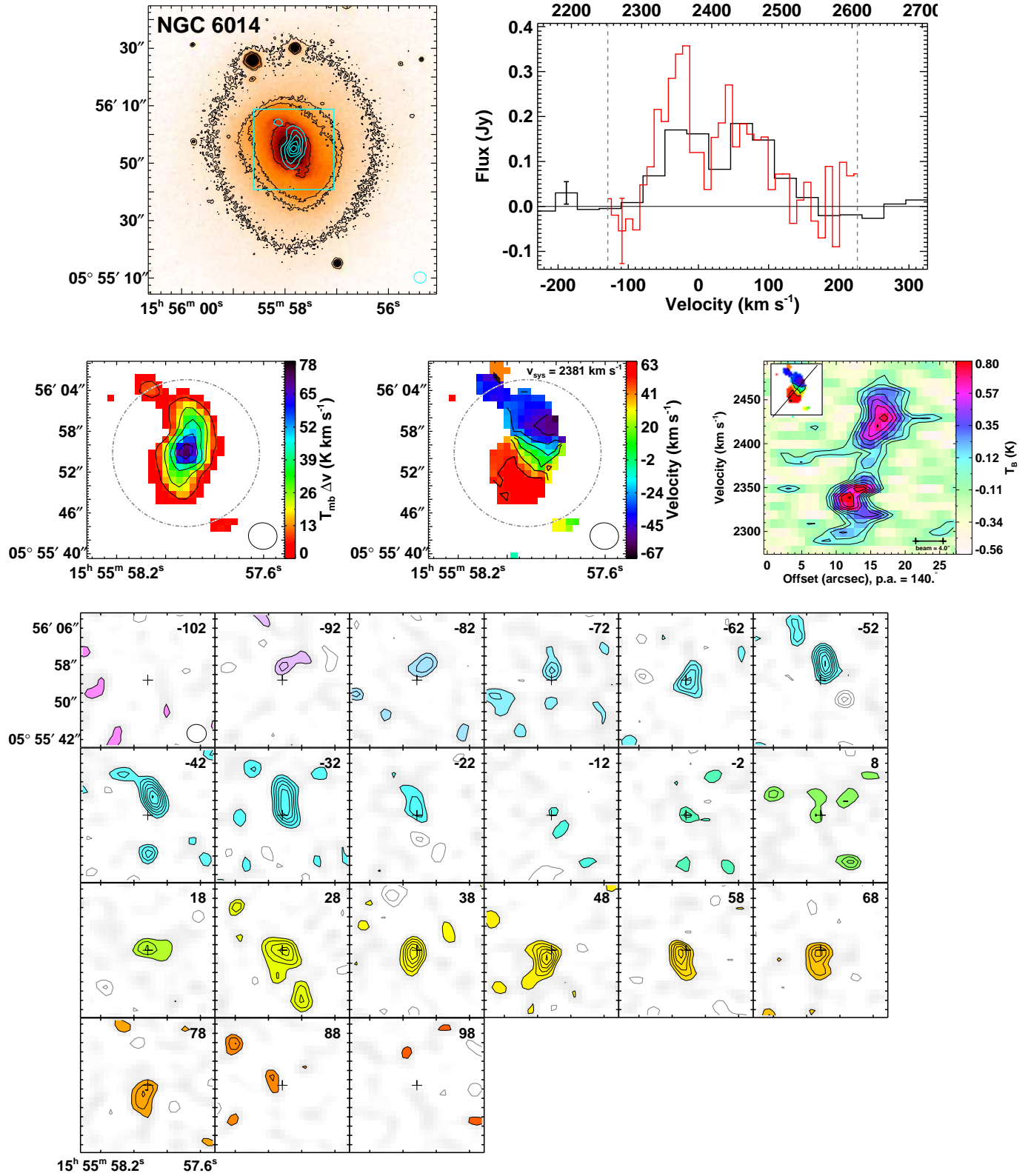


Figure A24. NGC 6014 is a field regular rotator ($M_K = -22.99$) with normal stellar morphology. It contains a dust bar, ring and filaments. The moment0 peak is $14 \text{ Jy beam}^{-1} \text{ km s}^{-1}$. PVD contours are placed at 1.5σ intervals.

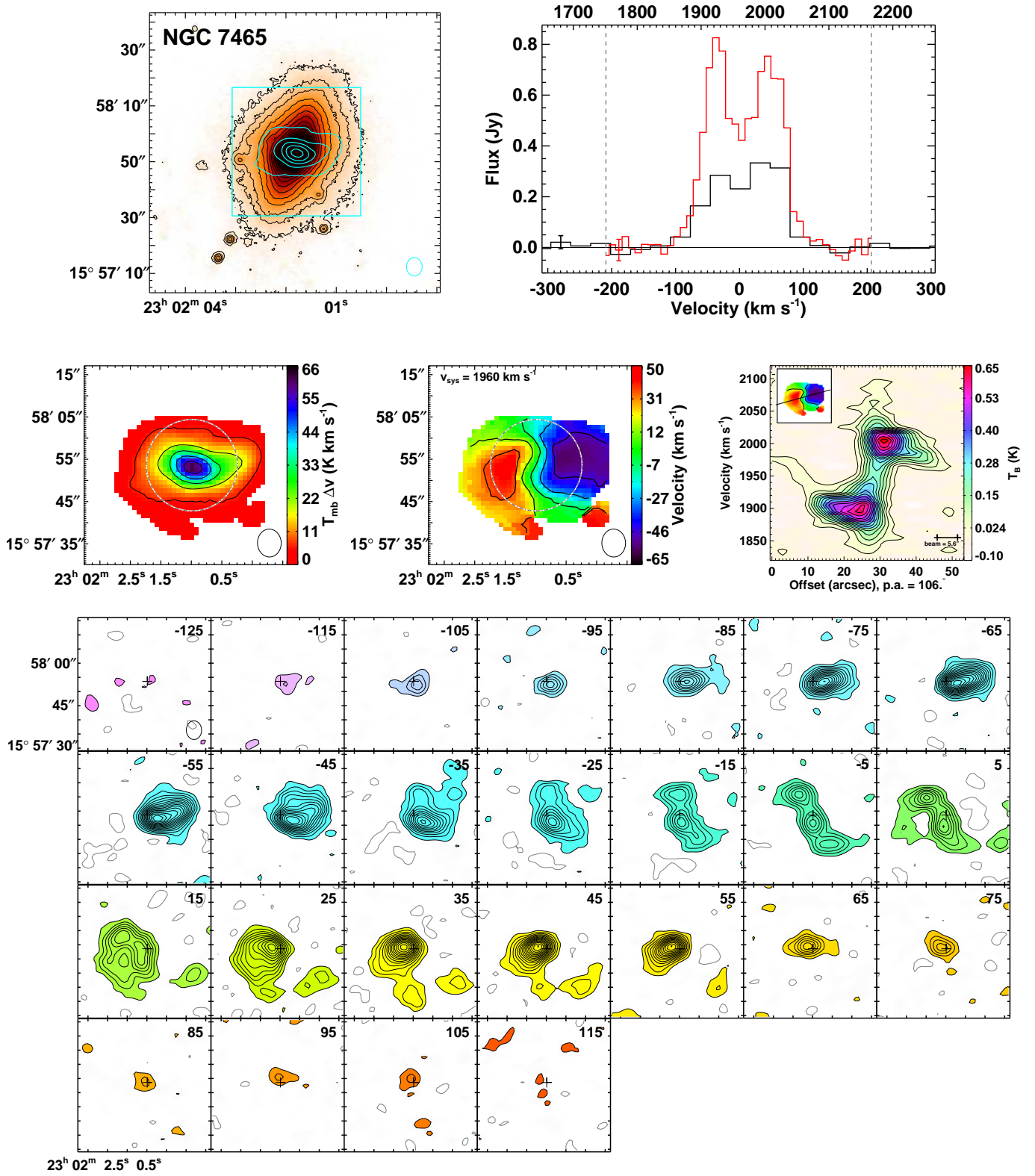


Figure A25. NGC 7465 is a field non-regular rotator ($M_K = -22.82$) with a kinematically-decoupled core (KDC) with stellar morphology indicative of interaction. It contains dust filaments. The moment0 peak is $26 \text{ Jy beam}^{-1} \text{ km s}^{-1}$. Channel map contours are placed at 2σ intervals and PVD contours are placed at 4σ intervals.

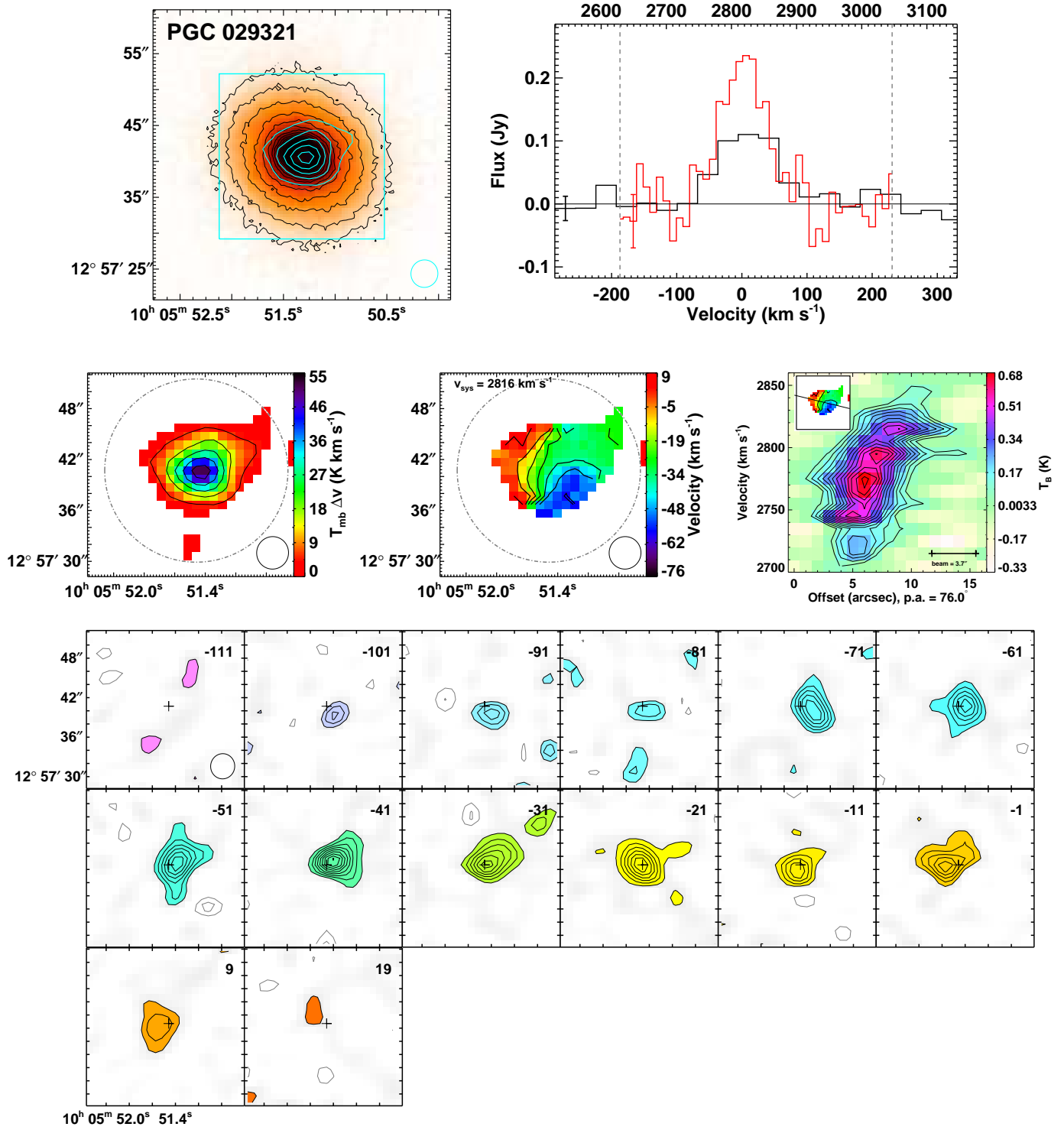


Figure A26. PGC 029321 is a field regular rotator ($M_K = -21.66$) with normal stellar morphology. It contains dust filaments. The moment0 peak is $8.5 \text{ Jy beam}^{-1} \text{ km s}^{-1}$.

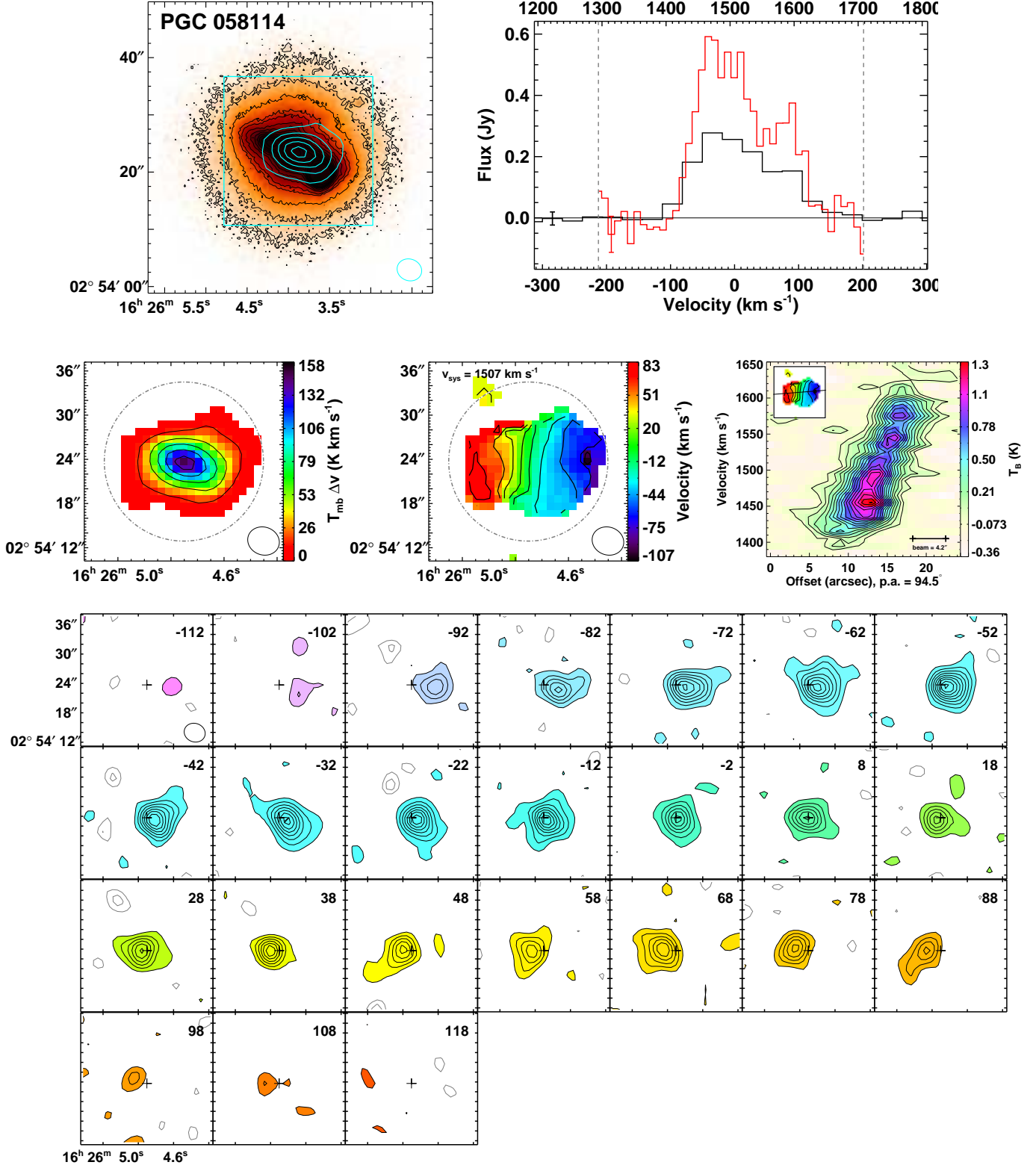


Figure A27. PGC 058114 is a field galaxy ($M_K = -21.57$) with unknown kinematic structure or morphology. The moment0 peak is $28 \text{ Jy beam}^{-1} \text{ km s}^{-1}$. Channel map and PVD contours are placed at 2σ intervals.

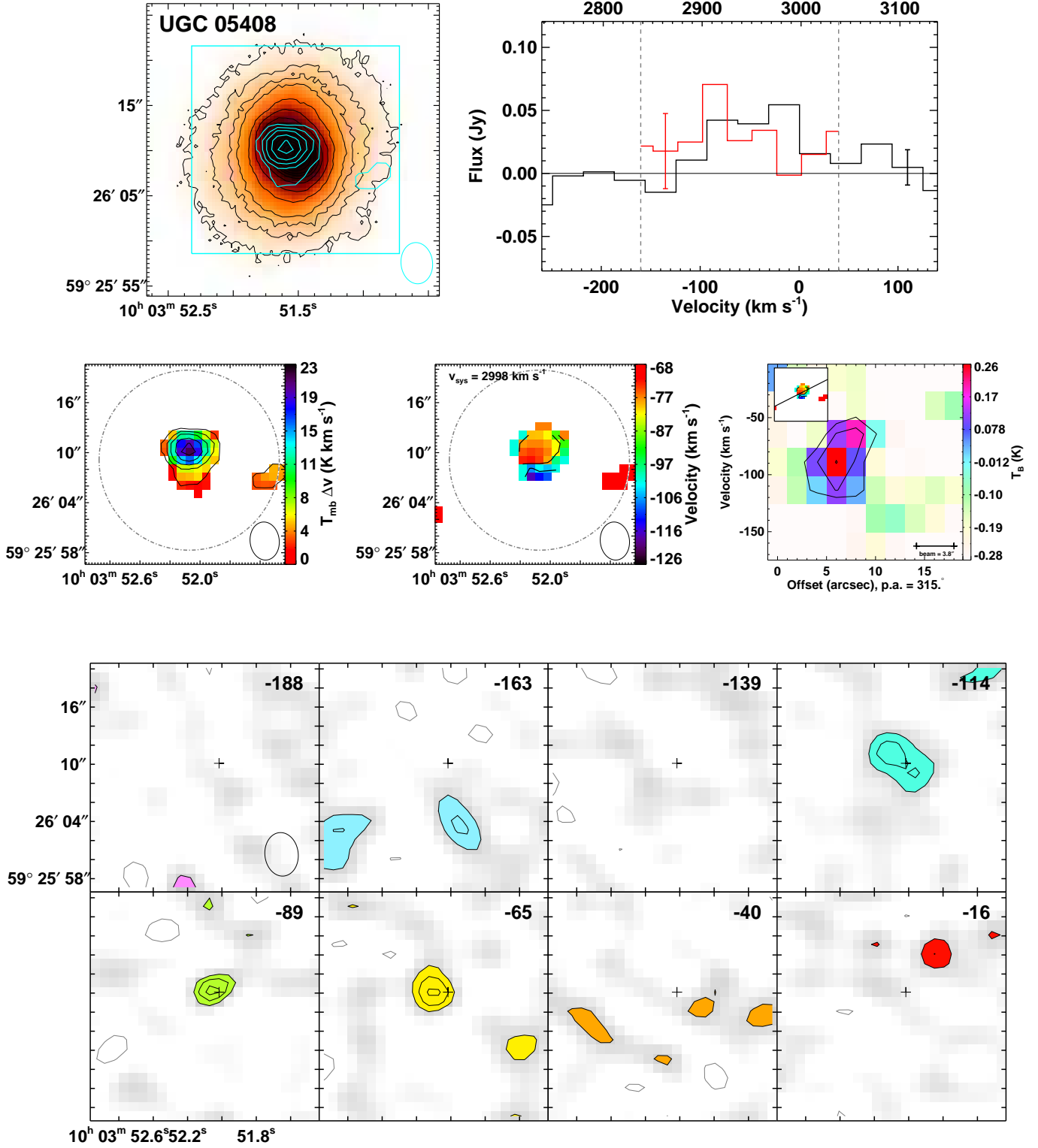


Figure A28. UGC 05408 is a field regular rotator ($M_K = -22.03$) with a bar stellar morphology. It contains a dust bar and filaments. At a distance 45.8 Mpc, it is the most distant detection in the CARMA ATLAS^{3D} survey. The moment0 peak is $3.5 \text{ Jy beam}^{-1} \text{ km s}^{-1}$.

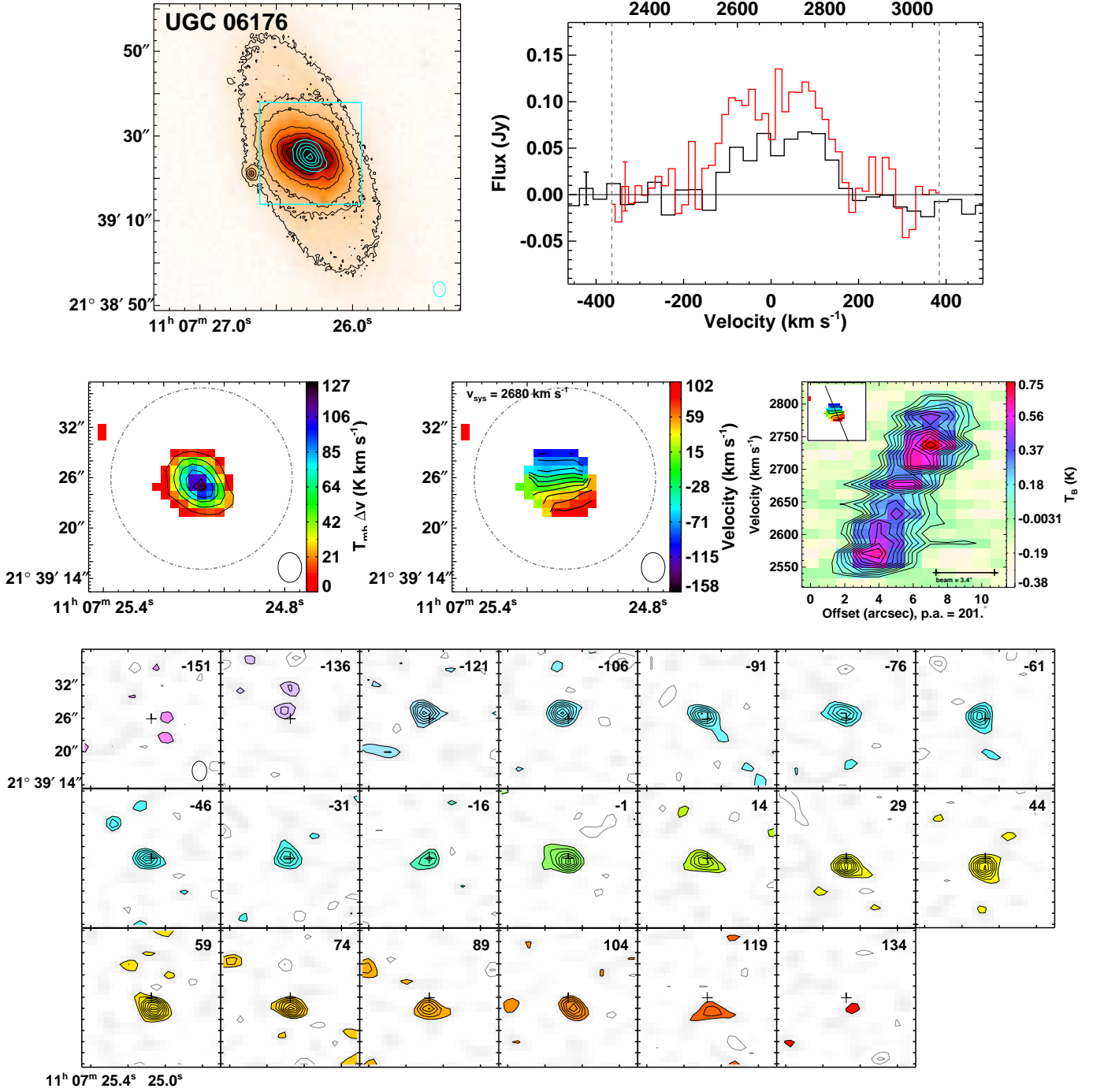


Figure A29. UGC 06176 is a field regular rotator ($M_K = -22.66$) with bar and ring stellar morphology. It contains a dust bar, ring, and filaments. The moment 0 peak is $14 \text{ Jy beam}^{-1} \text{ km s}^{-1}$.

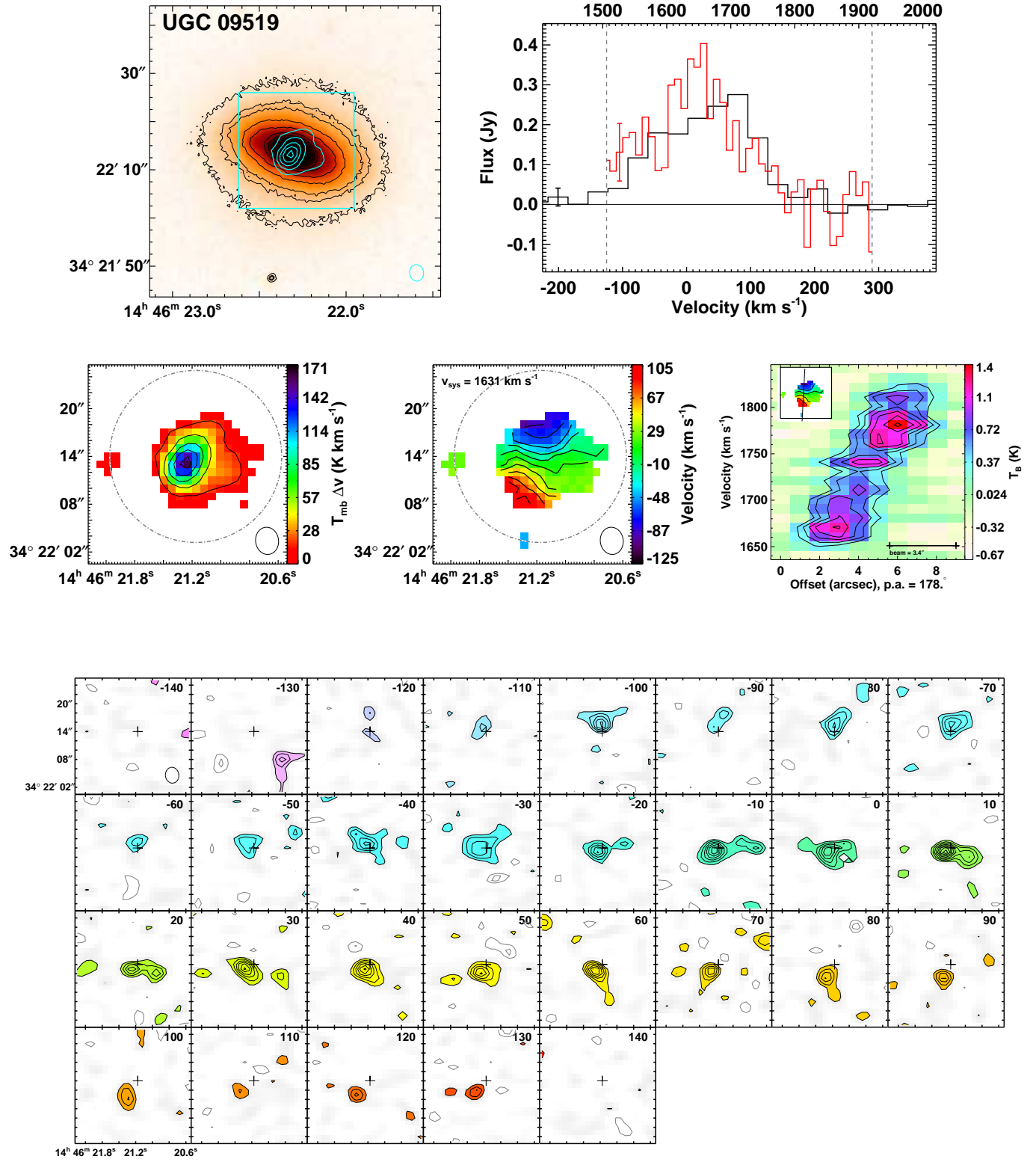


Figure A30. UGC 09519 is a field regular rotator ($M_K = -21.98$) with normal stellar morphology. It contains dust filaments. The moment0 peak is $18 \text{ Jy beam}^{-1} \text{ km s}^{-1}$.

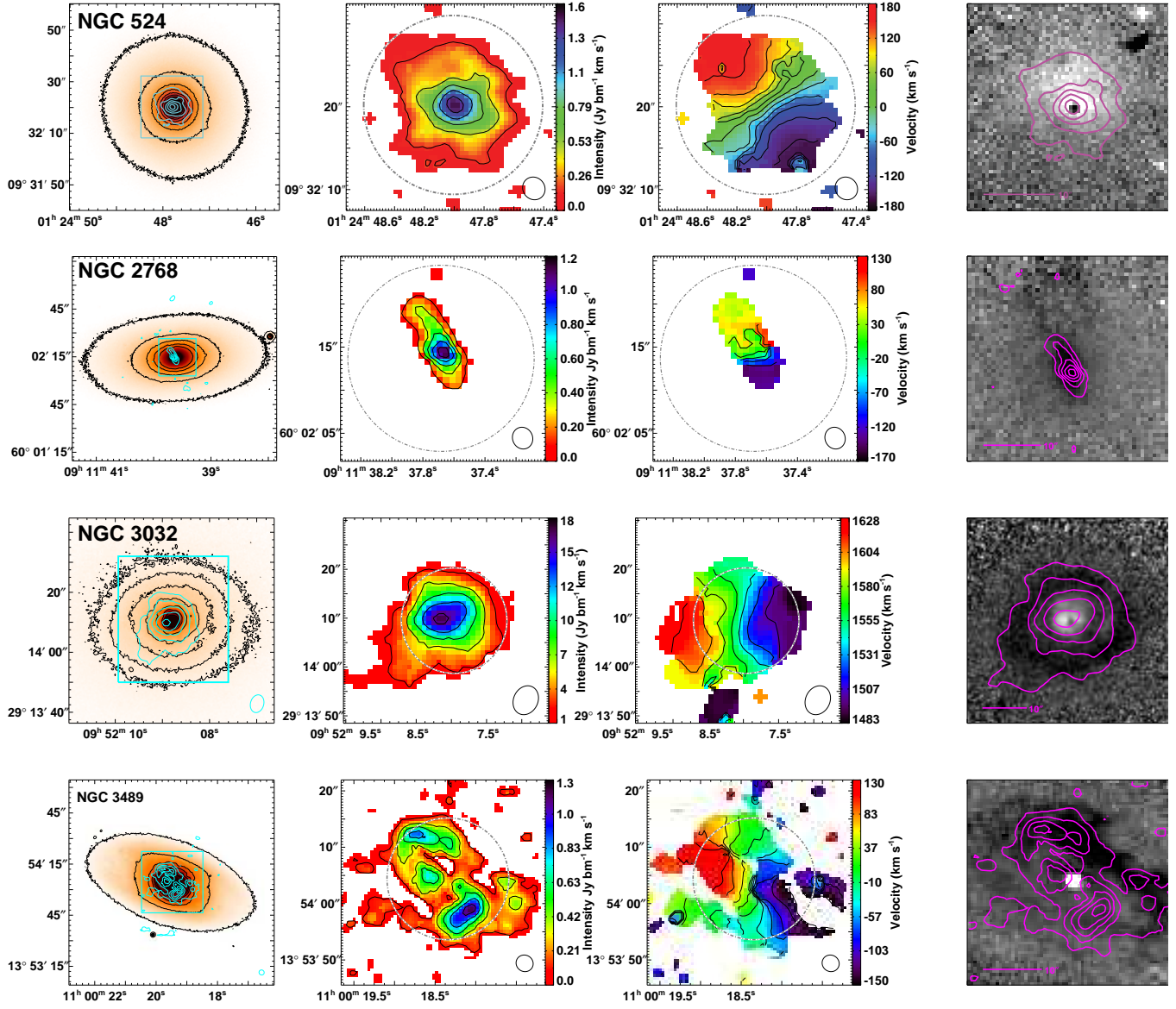


Figure B1. Interferometric CO(1-0) data from ATLAS^{3D} in the literature. From top-to-bottom, NGC 524 (Crocker et al. 2011), NGC 2768 (Crocker et al. 2008), NGC 3032 (Young, Bureau & Cappellari 2008), NGC 3489 (Crocker et al. 2011), NGC 4459 (Young, Bureau & Cappellari 2008), NGC 4476 (Young 2002), NGC 4477 (Crocker et al. 2011), NGC 4526 (Young, Bureau & Cappellari 2008) and NGC 4550 (Crocker et al. 2009). For each galaxy, from left-to-right, the panels show the r -band image overlaid with the CO(1-0) integrated intensity (moment0) contours (cyan), the color-scale and contours of the CO integrated intensity (moment0) map overlaid with the IRAM 30m telescope beam (gray), the color-scale of the CO mean velocity (moment1) map overlaid with isovelocity contours and the IRAM 30m telescope beam (gray), and the $g-r$ colour image overlaid with the CO(1-0) moment0 contours (magenta). For comparisons to unsharp-masked HST data of these galaxies, see the papers cited above.

APPENDIX B: INTERFEROMETRIC CO DATA FROM THE LITERATURE

APPENDIX C: GALAXIES OBSERVED WITH CARMA NOT IN THE ATLAS^{3D} SURVEY

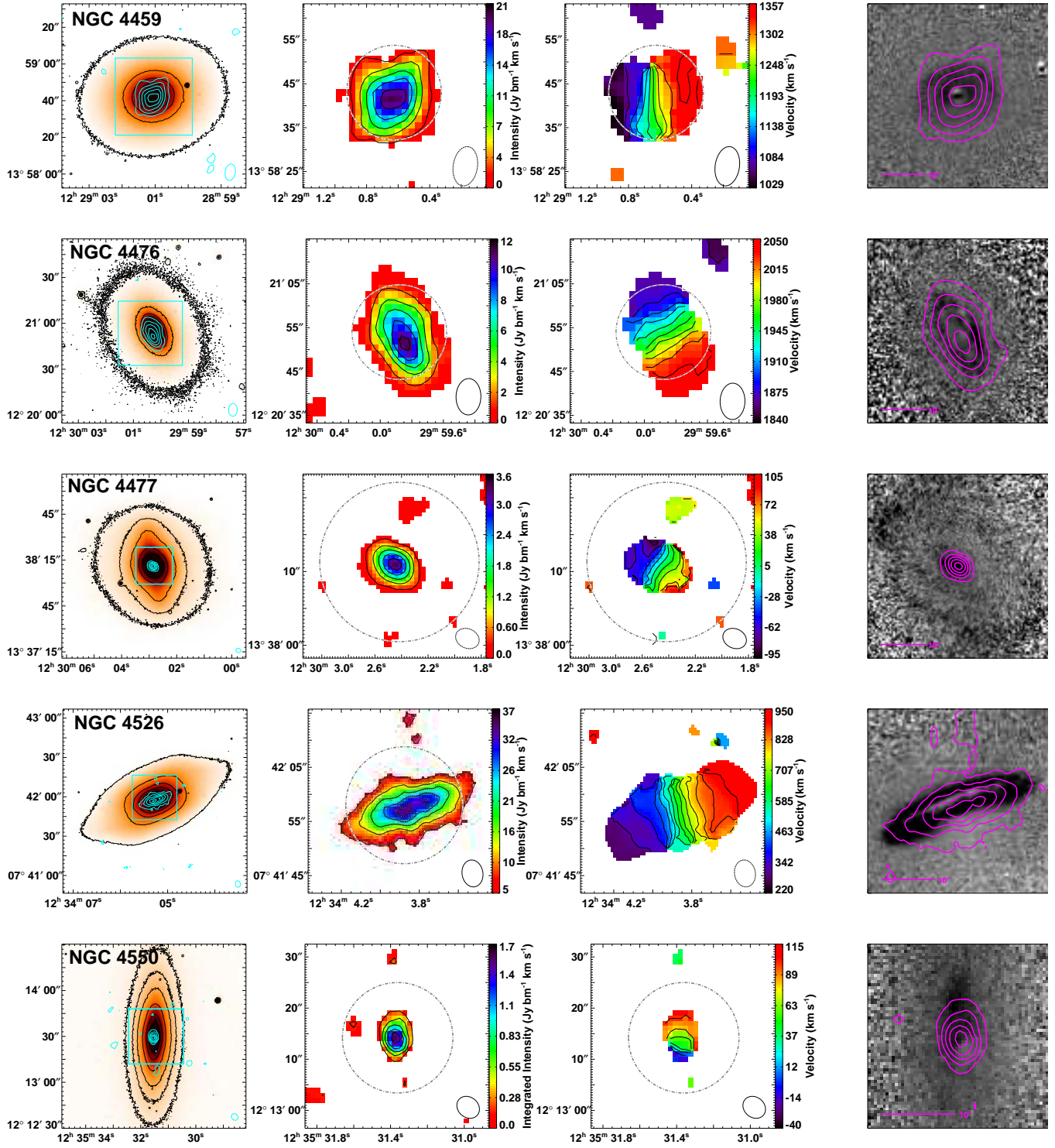


Figure B1. Continued

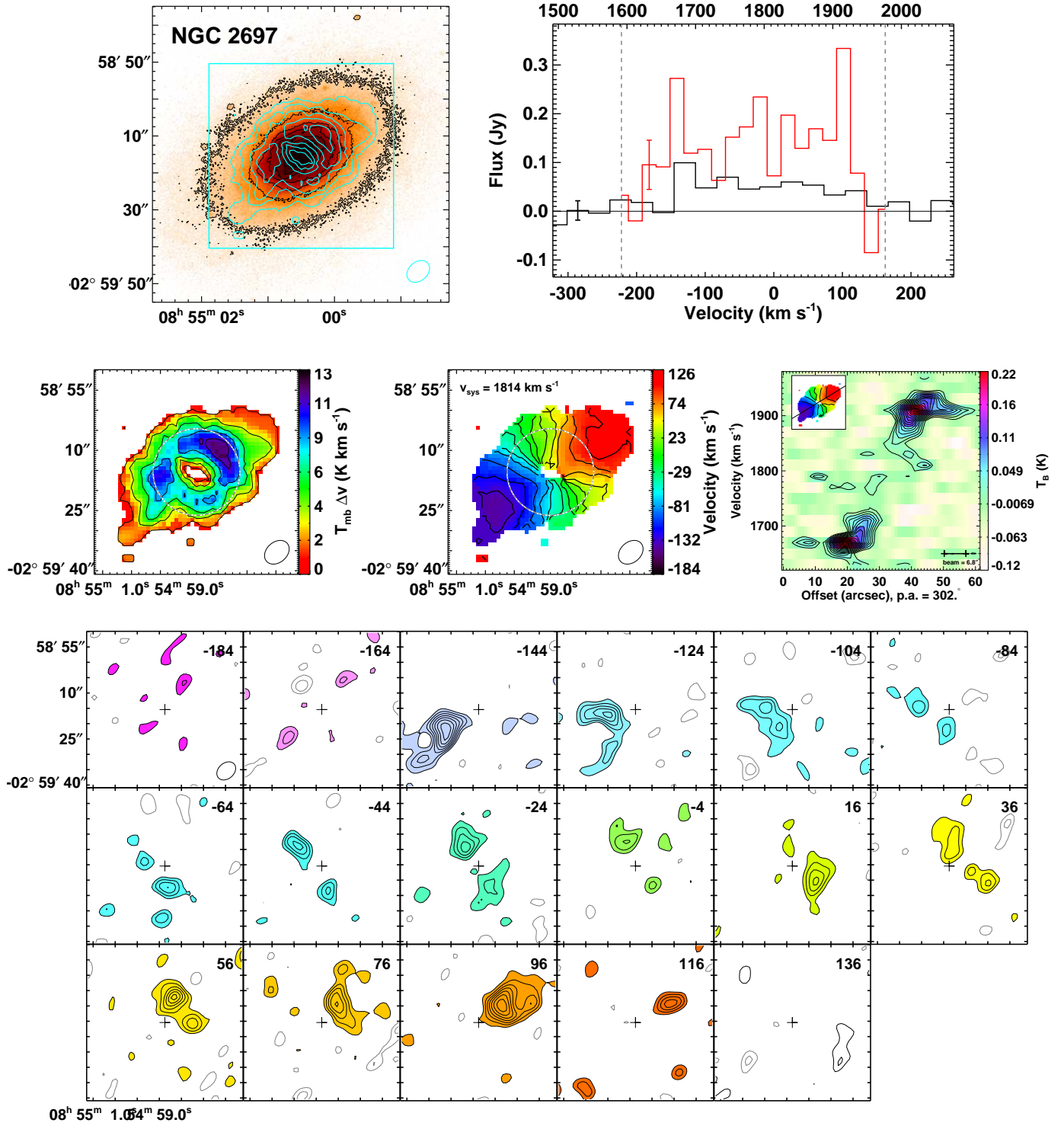


Figure C1. NGC 2697 ($M_K = -22.19$) was removed from the sample as being mis-classified and containing spiral structure in the stellar isophotes. The moment0 peak is $4.1 \text{ Jy beam}^{-1} \text{ km s}^{-1}$.

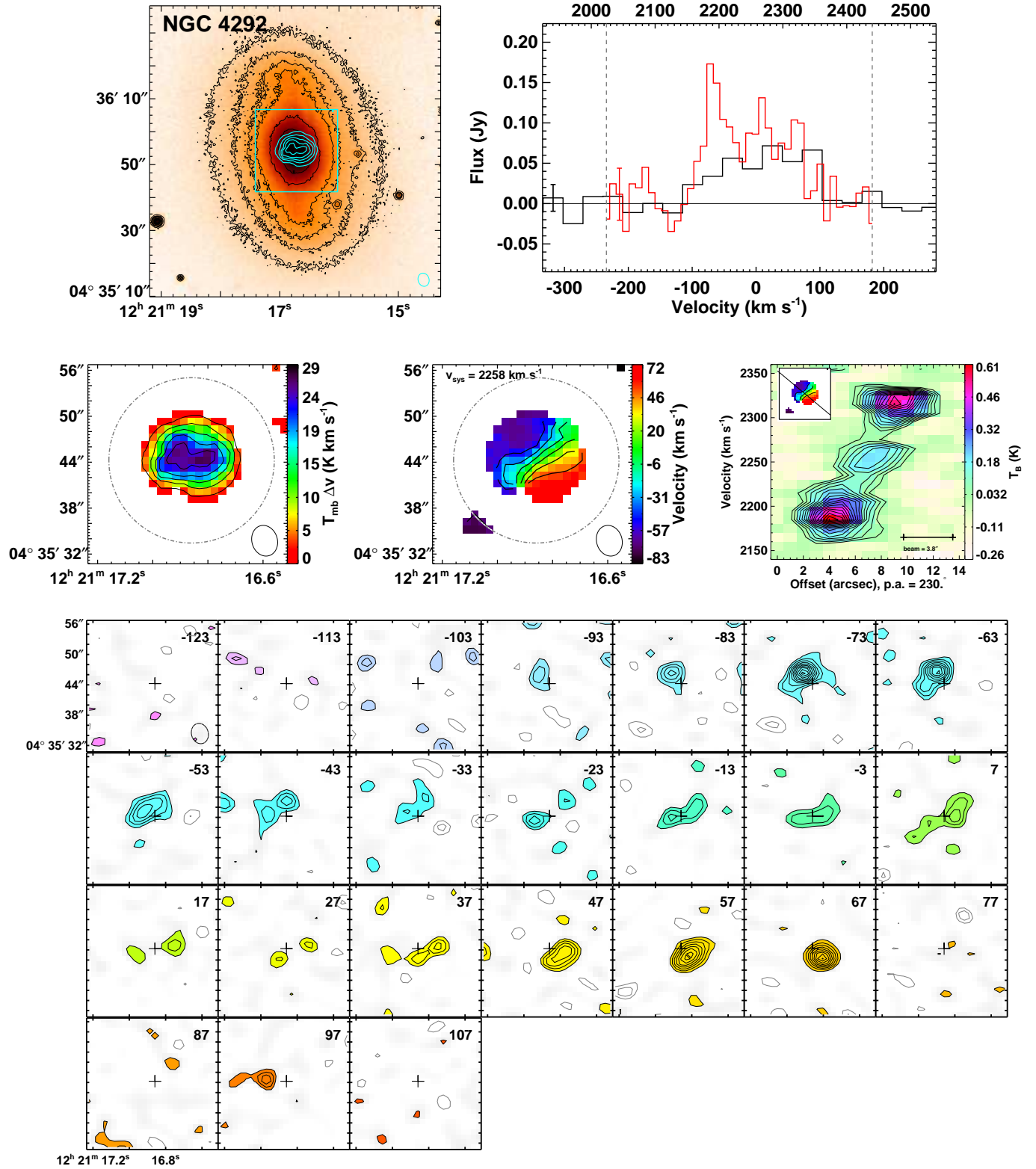


Figure C2. NGC 4292 is a Virgo cluster galaxy ($M_K = -23.2$). It was removed from the ATLAS^{3D} sample based on its not being observed with SAURON, and thus lacks stellar kinematic data. The moment0 peak is $4.3 \text{ Jy beam}^{-1} \text{ km s}^{-1}$.